Università degli Studi di Catania

PhD in Science and Technology of Materials
XXVII Cycle

Graphene Oxides and Related Applications

Simon Federico Spanò

Supervisor:
Chiar.mo Prof. G. Compagnini

Coordinator:
Chiar.ma Prof.ssa M.G. Grimaldi

PhD Thesis

A.Y. 2011-2014

Index

Introduction

Over the decades, materials science has undoubtedly occupied an increasingly important role in our everyday lives, firstly through the design, the synthesis and the diffusion of new materials, and, even if it is an obvious thing to say, it is always fundamental to emphasize how our quality of life has been made better over time thanks to the discovery of new materials. Moreover, it is also obvious that the need of creating new and more useful materials grows with the needs of society, and the limitations for responding to its requirements (e.g. sustainable energy, high performance and efficiency technology, affordable health care, personal protection, green technology, etc.) are closely linked to constraints in the properties of materials.

In the last fifteen years we assisted to an ever growing nanotechnology's impact on materials science and, consequently, on our daily routine.

Every object that have at least one dimension between 1 and 100 nm can be defined as "nanomaterial"; in this case, given the smaller sizes, the ratio between surface and inner atoms is very significant, manipulating physical, chemical and mechanical aspects of nanosystems and, therefore,

originating properties that can be totally different from bulk materials.

The explosive spread of nanotechnology in the last decade is primarily due to the availability of new approaches of synthesis (top-down and bottom up) and characterization on the nanometer scale. Furthermore, nowadays, we have a better understanding of electrical, thermal, optical, physical and magnetic properties of metal, semiconductor or dielectric nanostructures.

In recent years, carbon-based nanomaterials are among the most important systems for modern nanotechnology, because of the extreme flexibility of carbon atoms to produce different structures that include zero-dimensional (0D), one-dimensional (1D) and two-dimensional (2D) systems having plenty of different physical and chemical properties.

Without a shadow of a doubt, since its discovery in 2004, graphene has been the most promising and intriguing carbon-based nanomaterial, revolutionizing all the scientific fields due to its exceptional electrical, thermal, physical and chemical properties and opening new opportunities for future devices and systems. In fact, graphene's strength and flexibility, together with its interesting charge carrier and other properties, can improve the existing technologies and

can develop new technologic approaches, ranging from flexible electronics to DNA sequencing.

In addition, literature reports that, modifying the structure of graphene (basal planes or edges), it is possible to tune the graphene characteristics; therefore, it is the reason that the interest towards the fabrication of new graphene-based materials is growing among many research groups.

In this respect, graphene oxides (GOs) have recently emerged as a new carbon-based nanoscale materials that provides an alternative path to graphene. It is a single or few atomic layered materials made up of oxidized graphite (with various oxygenated functional groups on its basal plane and peripheries) which can be produced in large quantities at inexpensive prices.

One of the most attractive properties of graphene oxide is that it is possible to undergo it to reduction processes, removing the oxygen-containing groups with the recovery of a conjugated structure, in order to achieve graphene-like properties; in this way, through an opportune reduction approach, it is possible to tune the ratio of the sp^2 and sp^3 fractions and, consequently, its bandgap. Indeed, the tunability of the degree of reduction of graphene oxide is a very important parameter that permits us to modulate the characteristics of reduced GO to our advantage.

Most recently, several groups have demonstrated that, in addition to conventional chemical, thermal or electrochemical reduction methods, GO can be reduced by photoirradiating processes (e.g. UV-induced photocatalytic reduction, photothermal reduction using a pulsed Xenon lamp, etc.).

The reduction of GO is then definitely a key topic, and different reduction processes result in different properties that in turn affect the final performance of materials or devices composed of rGO.

The aim of my research project, during my PhD in Science and Technology of Materials, was the launching of a novel innovative approach of GO reduction that consists in the pulsed laser irradiation (532 nm) of a chemically prepared GO colloid. We can demonstrate that this method is able to finely tune the degree of reduction, tailoring the properties and the spectroscopic features of the final reduced graphene oxide (rGO) suspension. In this way, we can manipulate the degree of reduction and, consequently, the characteristics of these new intriguing nanosystems in order to earmark their use to several potential applications in many fields. For instance, my PhD research permitted to understand that the possibility to manage, through laser-induced reduction, many very important features like thermal and electric conductivity and gas/moisture-barrier

property, makes reduced graphene oxides suitable to be used like potential fillers for electronic packages.

Furthermore, the use of carbon-based nanomaterials like reduced graphene oxides is suitable both for the filtration of microorganisms and for the ability to adsorb heavy metals if their surfaces are adequately functionalized. Accordingly, during the last year of my PhD, I observed that, aptly tuning its degree of reduction and, then, its energy gap, we can earmark rGO to improve existing techniques of water treatment and purification, thanks to its antimicrobial activity and photocatalytic property.

Chapter 1. Carbon materials

1.1 Carbon allotropes: an introduction

Carbon is a non-metal element characterized by an amazing chemical versatility: its considerable capacity to combine with itself and other elements made it the essential element for organic chemistry and for life. At the same time, this important prerogative allows the formation of many stable carbon structures, allotropes, in every dimension. This occurs because four electrons in carbon valence shell (the carbon ground state electronic configuration is [($1s^2$) ($2s^2 2p^2$)]) form its three hybridizations (sp, sp^2, sp^3).

Allotropy consists in the being of an element in a crystalline solid state in various distinct forms that differ from each other by the spatial disposition of their atoms [1, 2]. This definition, however, tends to overlap with the concept of polymorphism [1,3] but, in reality, there is a considerable difference between them: the term “allotropy” relates to an alteration of the equation of state (EOS) of a substance (thermodynamic concept), instead the word “polymorphism” is related to a crystallographic concept.

The definition of allotropy given previously can be restricted, for carbon in particular, considering the type of

chemical bonds as a distinguishing property. But, having regard to the huge and ever increasing number of carbon allotropes, an opportune classification scheme for all carbon materials already proved necessary twenty years ago. A convenient classification scheme would be in accordance with the type of chemical bonds between carbon atoms, then according to the type of hybridization of the valence orbitals [4].

A first general classification scheme for carbon allotropes, proposed at the end of 90s, is shown in Fig. 1-1.

Nowadays the classification of carbon allotropes was subjected to a series of important changes and adjustments, thanks to the research and discoveries made in the last decade. However, it is still possible to make a classification based on hybridization and different dimensionality.

Depending on their spatial arrangement and, indirectly, on their type of hybridization, carbon materials can be divided into 3D, 2D, 1D and 0D allotropes. Summing up, beyond the best-known species such as diamond and graphite (3D), the other carbon allotropes are fullerenes and graphene quantum dots (0D), carbon nanotubes and polyynes (1D), graphene and graphene-based materials (2D).

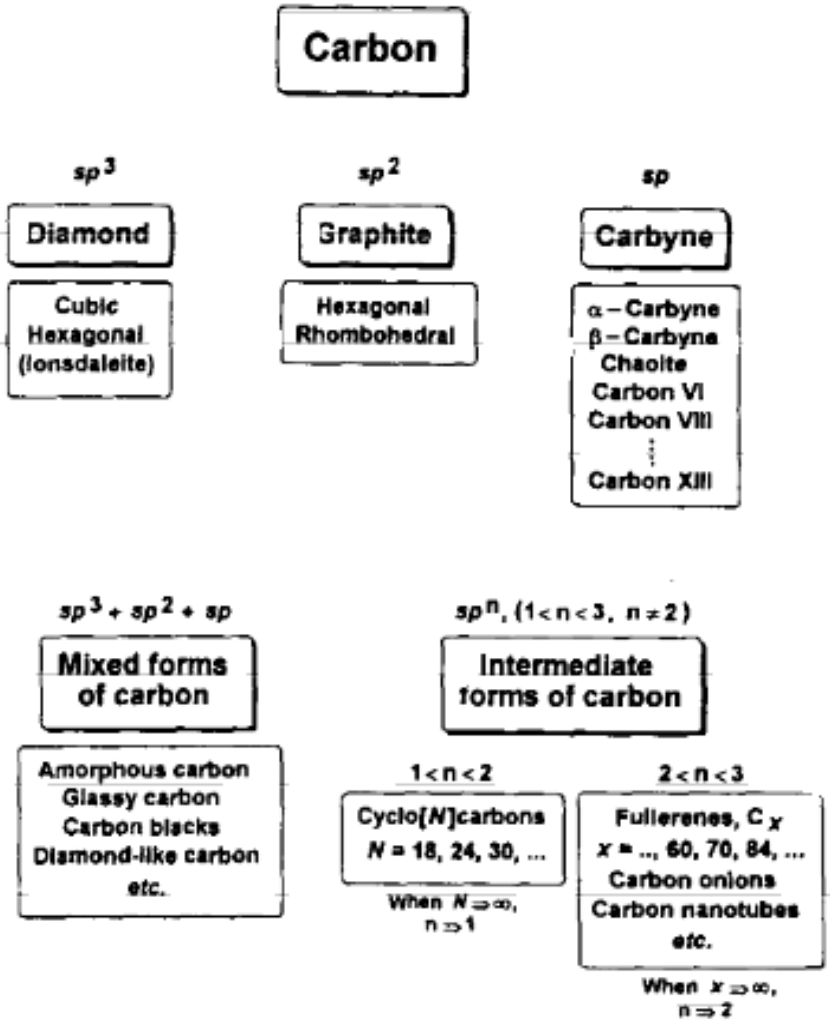

Fig. 1-1 A 90s classification scheme for carbon allotropes based on hybridization [Taken from ref. (1)].

1.2 Three dimensional carbon allotropes: Graphite and Diamond

Graphite and diamond exhibit diametrically opposite properties despite being two crystalline forms of the same element. A first reason for this huge difference between the two allotropes is to be identified in the different spatial arrangement of carbon atoms.

In a diamond, each carbon atom is connected to other fours by sp^3 σ bonds and all together are tetrahedrally arranged. Exactly, the carbon atoms show an arrangement that is a variation of a typical f.c.c. lattice (diamond lattice), as shown in Fig. 1-2.

The cubic form of diamond show a zincblende crystal structure (C-C bond length of 0.154 nm); in reality, diamond also exists in a rarer hexagonal form (Lonsdaleite), characterized by a Wurtzite crystal structure (C-C bond length of 0.152 nm).

This three-dimensional structure of diamond is extremely strong, creating an infinite network of atoms; this is the reason for its exceptional hardness (10^{th} on the Mohs scale), high strength and amazing resistance to compression.

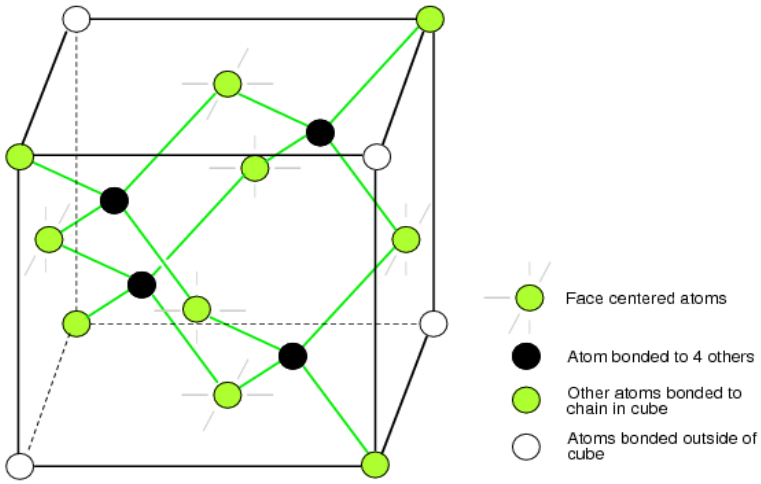

Fig. 1-2 Crystal structure of diamond

Diamond is the best thermal conductor in nature, conducting heat four times better than copper (1600 W m^{-1} K^{-1} for diamond vs 390 W m^{-1} K^{-1} for copper); it is also an excellent conductor of acoustic waves, but a very bad conductor of electricity.

Above 1700 °C in vacuum diamond changes to graphite, while, in air, the conversion starts at ~700 °C.

Also in graphite, carbon atoms form an infinite array, but, in this case, the crystal structure is hexagonal, with graphene plane like basis; consequently, carbon atoms forms a layered hexagonal array with a sp^2 hybridization.

The most usual and more stable crystal form of graphite is the hexagonal (*alpha*), with a stacking order of the layers ABABAB… (Fig. 1-3), unlike the rarer rhombohedral form (*beta*) is characterized by a stacking sequence ABCABC…
In a typical graphite plane carbon atoms, covalently bonded, show a C-C distance of 0.142 nm, while the interlayer distance is 0.335 nm. Probably, the weak interlayer forces are of the van der Waals type; this is the reason why graphite is characterized by easy exfoliation and excellent lubrification properties.

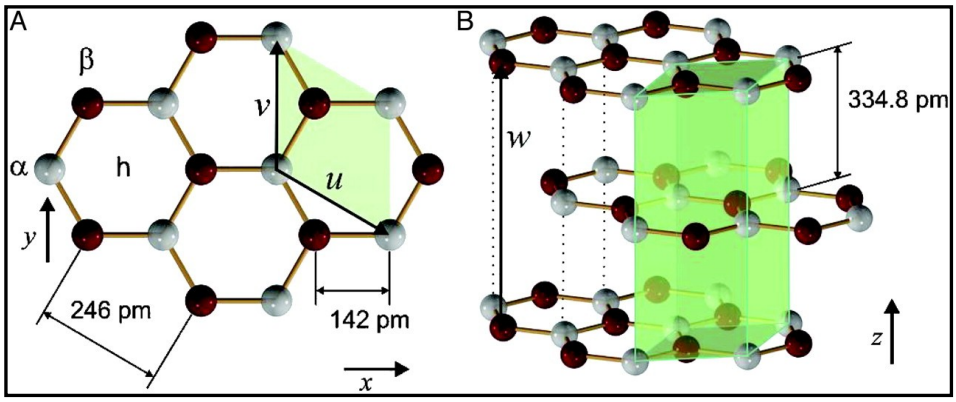

Fig. 1-3 Crystal structure of the hexagonal graphite.

Thanks to its thermal, electrical and mechanical properties and thanks to its chemical inertness, graphite finds application in many fields, like electrotechnic, metallurgy, aerospace industry, electroplating, automotive industry, etc.

1.3 Zero-dimensional carbon allotropes: Fullerenes and Graphene Quantum Dots

Fullerenes are cage-like polymorphs of carbon with general formula C_{20+2n}, discovered, in the form of C_{60} molecules, by H. Kroto and R. Smalley (1985) in the mass spectrum of laser-ablated graphite [5]. Their cage-like structure consists of hollow closed nets formed by 12 pentagonal and *n* hexagonal rings.

The C_{60} cluster (20 hexagons and 12 pentagons), named "buckminsterfullerene" because of its resemblance to the geodetic domes designed by Buckminster Fuller, is characterized by an icosahedral (I_h) point-group symmetry, related to its inherent five-fold rotational axes.

The distance between the C-atoms and the centre of the C_{60} cluster is about 3.55 Å, while the C-C bond has a length of 1.44 Å. It should also be highlighted that sublimed crystalline films of C_{60} form an f.c.c. packing in which the clusters are held together by weak van der Waals interactions; the packing is characterized by an inter-centre spacing of ≈ 10 Å and a minimum inter-cage separation of about 3 Å [6].

The distance between the C-atoms and the centre of the C_{60} cluster is about 3.55 Å, while the C-C bond has a length of

1.44 Å. It should also be highlighted that sublimed crystalline films of C_{60} form an f.c.c. packing in which the clusters are held together by weak van der Waals interactions; the packing is characterized by an inter-centre spacing of ≈ 10 Å and a minimum inter-cage separation of about 3 Å [6].

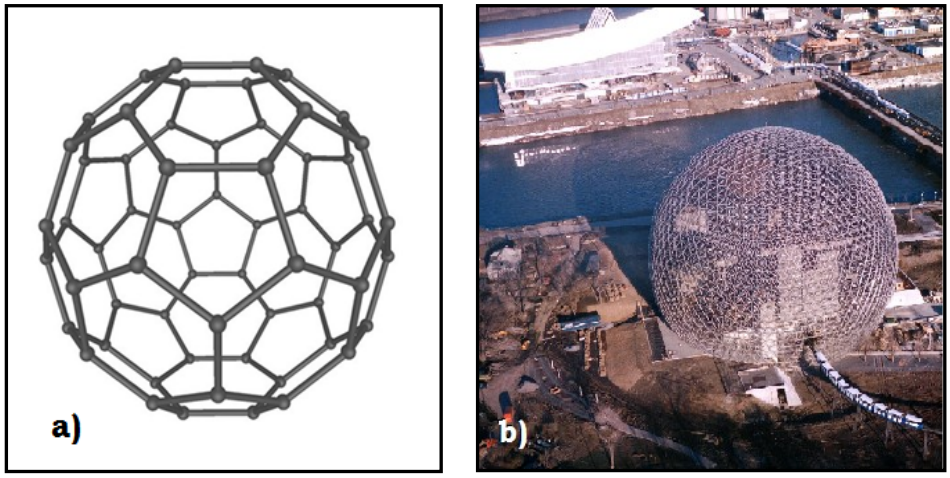

Fig. 1-4 : a) Crystal structure of C_{60}; b) geodetic dome by R. Buckminster Fuller.

Regarding the electronic band structure and density of states of f.c.c. C_{60} (Fig. 1-5), the uppermost states in the valence band, occupied by 60 electrons, derive from the 30 π-orbitals, grouped into seven variously degenerate

molecular-orbital energy levels. The widths of all bands are ≈ 0.5 eV, therefore very narrow, because of weak π-π interactions between C_{60} fullerenes in the solid state [6].

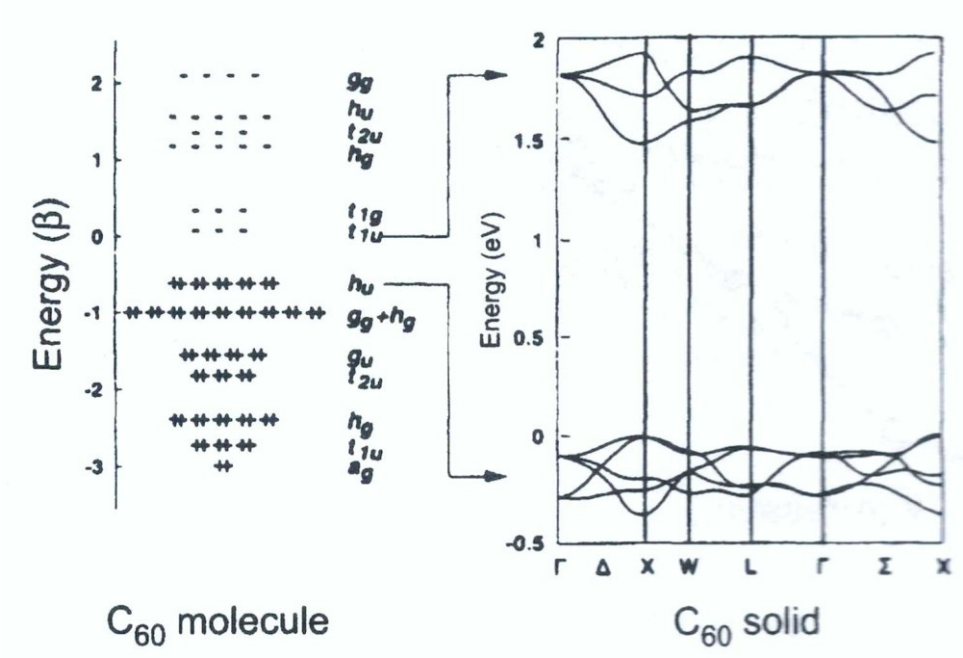

Fig. 1-5 : Electronic structure of C_{60}.

In the last years, another zero-dimensional form of carbon, that is arousing a great interest, is the zero-dimensional form of graphene, which can be called "graphene quantum dots" (GQDs). Generally, they can be described like

graphene sheets (less than 10 layers) with dimensions ranging from few nm to ~100 nm.
The increasing interest towards graphene quantum dots derives from the remarkable optical and electronic properties, related to the quantum confinement and edges effects, clearly observed because of the restricted size of GQDs.

1.4 One-dimensional carbon allotropes: Carbon Nanotubes and Polyynes

Another new member of carbon allotropes family (discovered in 1991 by Iijima [7]), intermediate in dimensionality between the 0D buckyballs and the 2D hexagonal-net layer structure of graphite, is nanotubes. These are one-dimensional tubular structures with diameters of a few nanometers, consisting of rolled graphene sheets and capped by an hemispherical section of fullerene structure [6].
In Fig. 1-6 it is possible to observe a typical example of carbon nanotubes, consisting of a chiral, single-shell structure (diameter d=10.36 Å) with end-caps based on an icosahedral C_{140} fullerene [8].

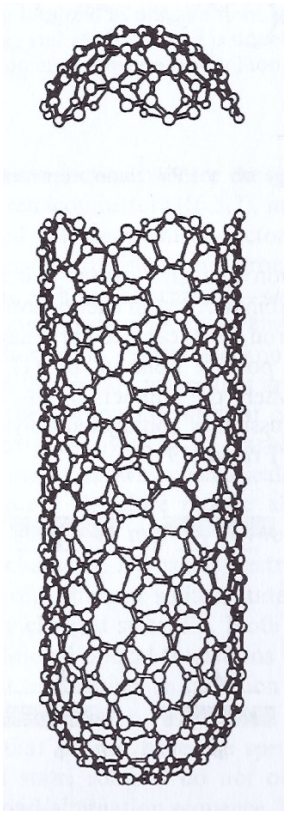

Fig. 1-6: An example of chiral, single-shell carbon nanotube, of diameter *d*=10.36 Å, based on a icosahedral C_{140} (from ref. [8]).

Carbon nanotubes can be composed of one rolled graphitic sheet (single-wall carbon nanotubes, SWCNTs), two graphene sheets (double-wall carbon nanotubes, DWCNTs), or formed by many graphitic sheets (multi-wall carbon nanotubes, MWCNTs) (Fig. 1-7).

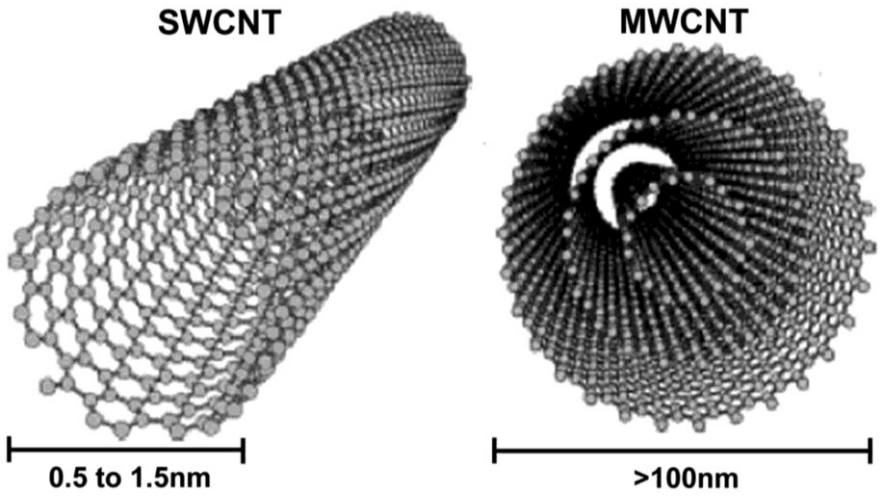

Fig. 1-7: Structure of a SWCNT and of a MWCNT.

The characteristics of CNTs, like, for example, diameter and degree of helicity, can be expressed in terms of a *chiral vector*; it can be defined like the vector connecting two "cristallographically" equivalent lattice sites (O and A in Fig. 1-8) in an unrolled honeycomb lattice.
The *chiral vector* can be expressed with the two unit vectors of the primitive cell $\mathbf{a_1}$, $\mathbf{a_2}$:

$$\boldsymbol{C_h = na_1 + ma_2 \equiv (n,m)}$$

where n and m are positive or negative integers (or zero).

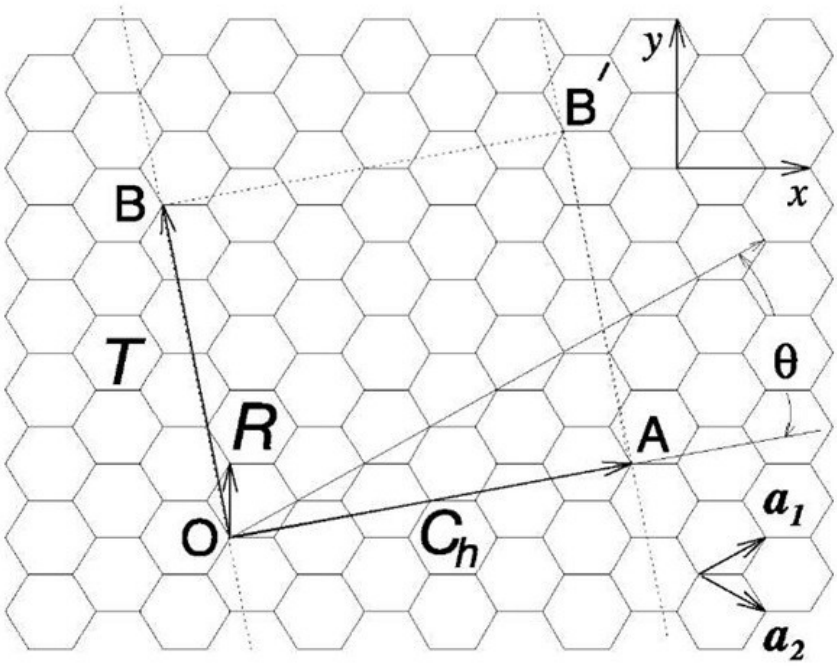

Fig. 1-8: The unrolled honeycomb lattice of a nanotube. OA is the C_h chiral vector, while the θ angle is the chiral angle of the nanotube.

The coordinates (n, m) allow to determine the tube diameter *d* and the number of carbon atoms per unit cell *N* [9]:

$$\boldsymbol{d = \frac{a}{\pi}\sqrt{n^2 + m^2 + nm}} \qquad \boldsymbol{N = \frac{2\,(n^2+m^2+nm)}{d_R}}$$

where a=2.41 Å is the lattice constant of the unrolled honeycomb lattice and d_R is:

$$\boldsymbol{d_R} = \begin{cases} \boldsymbol{d_H} \text{ if (n-m) is not a multiple of } 3\boldsymbol{d_H} \\ \boldsymbol{3d_H} \text{ if (n-m) is a multiple of } 3\boldsymbol{d_H} \end{cases}$$

where $\boldsymbol{d_H}$ is the highest common divisor of n and m.

Depending on the chiral integer n and m, CNTs can be distinguished in:

- *Armchair type*, when **n = m** ($\theta = \pi/6$)
- *Zig-zag type*, when **m = 0** ($\theta = 0$)
- *Chiral type*, when **n ≠ m ≠ 0**

The most interesting feature of CNTs is that their electrical properties depend on the helicity parameter C_h [10]. In general:

- if **n-2m=0** → *metal*
- if **n-2m=3j** (j=1,2,…) → *narrow-gap semiconductor*
- otherwise → *wider-gap semiconductor*

Moreover, it is also interesting to note that the energy gap of semiconducting CNTs is inversely proportional to the diameter of the tube, according the equation:

$$E_g = \frac{2\gamma a_{C-C}}{d_t}$$

where γ is the nearest neighbor interaction energy, a_{C-C} (0.142 Å) is the carbon-carbon bond distance, d_t is the nanotubes diameter [11].

While much is known about the new allotropes like fullerenes, nanotubes and graphene, on the other hand little is known about the *sp*-hybridized carbon allotropes, called carbines, which are linear polymeric chains of *sp*-hybridized carbon atoms [12]. Only recently the knowledge of properties and characteristics of the two isomeric forms of carbyne, polyynes $[-(-C \equiv C -) -]_n$ and polycumulene $[= (= C =) =]_n$, is increased. In particular, polyynes (chains of alternating single and triple bonds) are known to exist as interstellar materials [13] and they have attracted considerable interest for their size-dependent band gap [14] and potential nonlinear optical properties [15].
In reality a real acceptance of the significance of polyyne is not fully accepted by the scientific community, because of

its instability (its strong tendency to interact with oxygen causes the destruction of the chain) [16].
Therefore, the carbyne structures require stabilization and, consequently, tend to create chain-chain cross-linking processes.

1.5 Graphene and graphene related materials

- *Crystal and electronic structure of Graphene*

"Graphene" is made of a layer of sp^2-hybridized carbon atoms arranged into a 2D hexagonal crystal lattice (honeycomb) and it is the building block of the other carbon allotropes like fullerenes, nanotubes and graphite (Fig. 1-9).

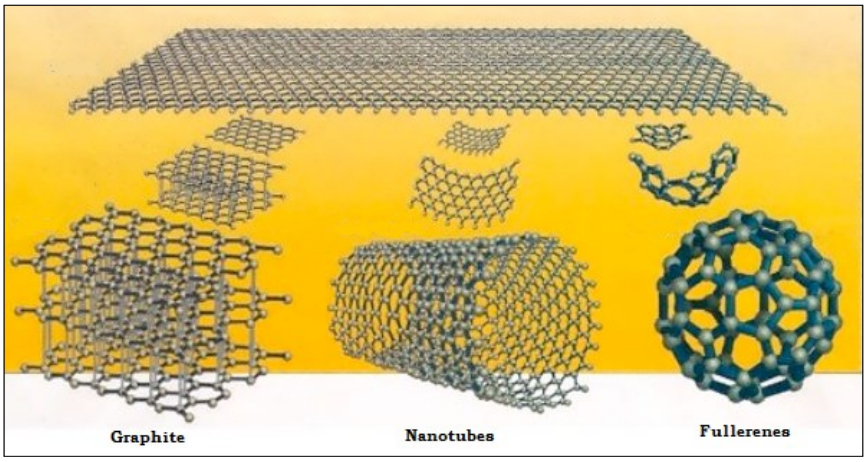

Fig. 1-9: Graphene as basis for the other carbon allotropes.

Graphene was considered a purely theoretical concept rather than an existing material for a long time, because the scientific world believed that two-dimensional materials did not exist without a three-dimensional base. However, in 2004, its existence was confirmed thanks to studies and research of two physicists of the University of Manchester, A. Geim and K. S. Novoselov [17].

As mentioned in the previous page, graphene is made by a 2D hexagonal crystal lattice, in which the carbon-carbon distance $a_{C\text{-}C}$ is 0.142 nm.

In Fig. 1-10 it is possible to observe the primitive cell of graphene, composed of two inequivalent atoms, A (white) and B (black).

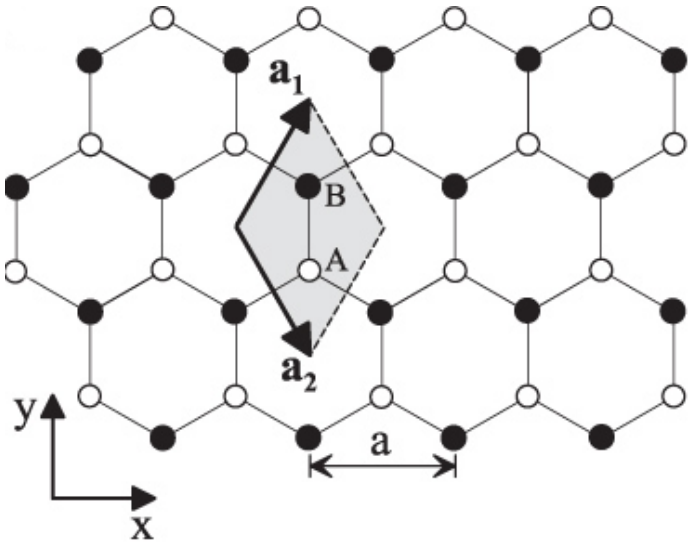

Fig. 1-10: Hexagonal lattice of graphene (taken from ref. [18]).

Graphene is not a Bravais lattice and it can be schematically considered as a triangular two-dimensional network with two carbon atoms in the primitive cell or like a compenetration of two equivalent triangular sublattices, A and B.

Considering the structure showed in Fig. 1-11, it is possible to observe the lattice vectors of graphene, $\mathbf{a_1}$ and $\mathbf{a_2}$ that can be written as:

$$\boldsymbol{a_1} = \frac{\boldsymbol{a}}{\mathbf{2}}\left(\mathbf{1}, \sqrt{\mathbf{3}}\right); \qquad \boldsymbol{a_2} = \frac{\boldsymbol{a}}{\mathbf{2}}\left(\mathbf{1}, -\sqrt{\mathbf{3}}\right)$$

where $\boldsymbol{a}$ is the lattice constant $\left(a = \sqrt{3a_{C-C}}\right)$.

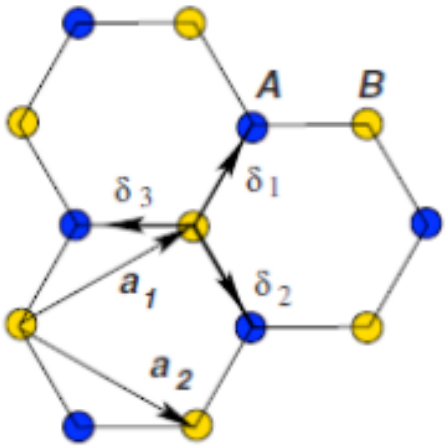

Fig. 1-11: Honeycomb lattice of graphene in which the lattice vectors a_1 and a_2 are outlined.

Moreover, in Fig. 1-12 it is possible to observe the reciprocal lattice of graphene (hexagonal Bravais lattice), in which the hexagonal first Brillouin zone is shown; the side length is $4\pi/3a$, while the two vectors $\mathbf{b_1}$ and $\mathbf{b_2}$ can be written as:

$$\boldsymbol{b_1} = \frac{2\pi}{3a}\left(1;\ \sqrt{3}\right) \qquad \boldsymbol{b_2} = \frac{2\pi}{3a}\left(1;\ -\sqrt{3}\right)$$

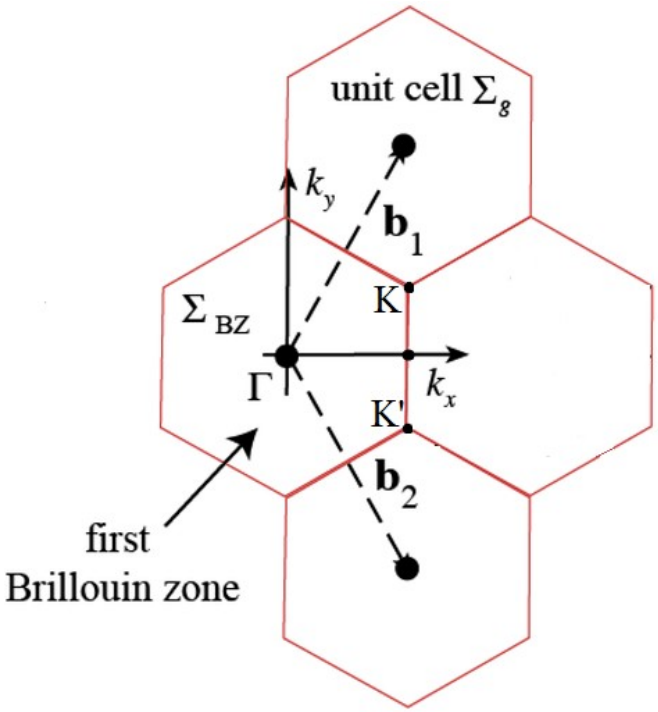

Fig. 1-12: Reciprocal lattice of graphene and its first Brillouin zone (Adapted from ref. [19]).

The corners of the first Brillouin zone, **K** and **K'** (inequivalent Dirac points), are particularly important for physics of graphene; their coordinates in the reciprocal space are [20]:

$$\mathbf{K} = \left(\frac{2\pi}{3a}; \frac{2\pi}{3\sqrt{3}a}\right) \qquad \mathbf{K}' = \left(\frac{2\pi}{3a}; -\frac{2\pi}{3\sqrt{3}a}\right)$$

In graphene carbon atoms are sp^2 hybridized, because of the head-on overlapping of the 2s orbital with $2p_x$ and $2p_y$ orbitals (generation of σ and σ* bonds); instead, the valence electron into the remaining free $2p_z$ orbital (perpendicular to the plane) generates a π and π* bond.

The three σ electrons do not take part to the electronic conduction into graphene, while the electron into the π orbital gives its conductive properties.

Graphene is a zero-gap semiconductor [21]: in fact, there is no band gap between the π valence and π* conduction bands; consequently, the two bands do not exhibit any overlap, "touching each other", on the Fermi level (0 eV), in correspondence of the K and K' points that, for this reason, are defined as *charge neutrality points* or *Dirac points*.

- *Potential applications of Graphene*

Graphene is the subject of numerous studies for potential applications in various fields, although it has been discovered very recently (2004).
First, several studies were aimed at showing that the exceptional properties of graphene, like ballistic transport, linear current-potential relation and the capacity to sustain high currents [17], make it an excellent material for the production of field-effect transistors (FET).
Moreover, the surprising characteristics of graphene make it potentially suitable for its applications in gas and bio-related sensors [22], organic light-emitting diodes (OLEDs) [23], fuel cells, solar cells [24] and energy storage.
Besides, graphene's strength, flexibility, and its notable charge carrier make it the perfect material for flexible electronics.

- *Graphene synthesis*

In last years, several chemical and physical methods have been proposed for the synthesis of graphene:

➢ <u>Chemical approaches</u>

- chemical exfoliation of graphite [25, 26];

- epitaxial growth;
- chemical vapor deposition of hydrocarbons;
- chemical reduction of graphene oxide [27].

➢ Physical approaches

- mechanical cleavage of graphite;
- unzipping of carbon nanotubes [28];
- arc discharge method [29];
- mechanical exfoliation of highly ordered pyrolytic graphite (HOPG), better known by the name of "scotch tape method" (this is the approach by which Geim and Novoselov discovered graphene in 2004) [17].

Recently, an alternative top down method has been proposed: the laser exfoliation of graphite, theorized for the first time by Jeschke in 2001 [30].

- *Graphene-based materials*

Very recently, several scientific groups have focused their interest on the deepening of knowledge related to new graphene-based materials:

- Graphene nanowalls (GNWs), which are 2D graphene multilayers staying perpendicularly on a

substrate, promising material for nanoelectronics [31, 32].

- Porous graphene (PG), which are graphene layers with holes (pores) on the surface of the sheet; it can be potentially used as membrane for gas separation [33] and energy storage [34, 35].
- Graphene quantum dots (GQDs), which are 0D materials that can be considered as small pieces of graphene sheets (less than 100 nm); GQDs can find potential applications in several fields, like water treatment [36] and photovoltaics.

- *The graphene precursor: graphene oxide*

Graphene oxide (GO) is a layered material, obtained by a hard oxidative process of graphite that involves the formation of various oxygenated functional groups on its basal plane and peripheries.

The first researcher that synthetized GO was Brodie in 1859 [37], handling graphite with an oxidative mixture made of potassium chlorate and fuming nitric acid.

Nowadays, the most used synthesis process is the Hummers method, in which the graphite is handled with a solution made up of sulfuric acid, sodium nitrate and potassium permanganate [38].

This interesting and notable carbon material e its several partially reduced forms, which are the basis of my PhD course, will be discussed in depth in the next chapters, scanning in detail their structural characteristics, properties and potential applications (in particular in nanoelectronics field) and focusing on the innovations that they would imply.

Chapter 2. Graphene oxide and reduced derivatives

2.1 Graphene oxide: introductory aspects

Graphene oxides (GOs) have recently emerged as a new carbon-based nanoscale materials that provides an alternative path to graphene [39, 40]. It is a single or few atomic layered materials made up of oxidized graphite and characterized by the presence of various oxygenated functional groups on its basal plane and peripheries.

Chemical structure of GO is still under debate, and many models have been proposed [41]. The most accepted one [42] points to a variable degree of oxidation in GOs, fluctuating at the nanometer scale, suggesting the presence of sp^2 and sp^3 carbon clusters of a few nanometers [43]. Exactly, the STM and HRTEM analysis show that hexagonal lattice of graphene is clearly preserved in some parts of the sheet while the oxidized regions appear highly defective [44, 45]. The retention of graphene-like structure, albeit with disorder, indicates that the carbon atoms attached to functional groups are slightly displaced, but the overall size of the unit cell in GO remains similar to that of graphene.

As a result, GO can be described as a random distribution of sp^3 oxidized zones characterized by the presence of oxygenated functional groups (i.e., hydroxyl, carboxylic and epoxide groups grafted randomly), combined with non-oxidized regions where most of the carbon atoms preserves sp^2 hybridization typical of pure graphene (Fig. 2-1).

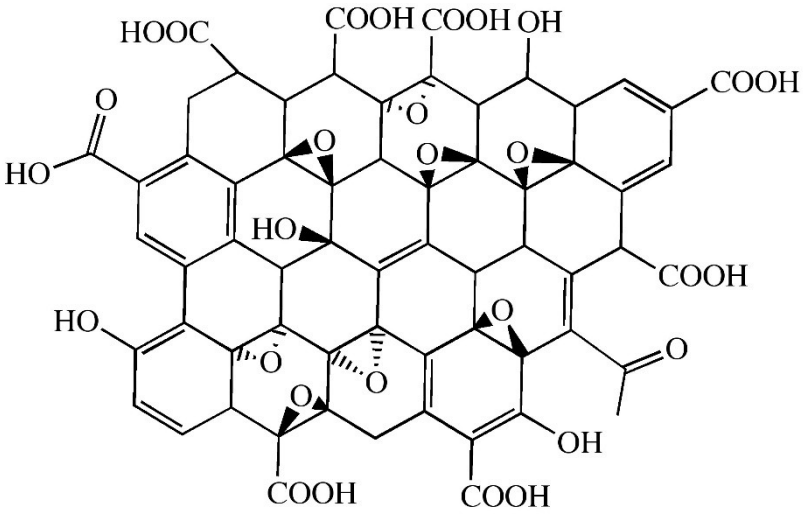

Fig. 2-1 Idealized structure proposed for graphene oxide (Taken from ref. [46]).

One of the most attractive properties of GO is that it can be (partly) reduced to graphene-like sheets by removing the oxygen-containing groups with the restoration of the typical graphene structure. Among the strategies developed to

reduce GO, low-temperature chemical reactions with reducing agents [47-49] or thermal treatment [50] are extensively used. Unfortunately, the preferred reducing agent (hydrazine) is toxic, and the deoxygenating processes are time consuming and complicated. Most recently, several groups have demonstrated that GO can be reduced by photoirradiating processes, such as UV-induced photocatalytic reduction [51, 52], photothermal reduction using a pulsed Xenon flash [53] or selective reduction by direct laser writing [54].

The reduction of GO and the capacity to modulate and check this process are key topic for my PhD course. In fact, graphene oxide and its reduced derivates are becoming more and more interesting for many potential applications in various fields, including electronics (e.g. electronic packaging for high power electronic devices) and photocatalysis (e.g. water purification), thanks to their notable properties that will be discussed in the following pages. In this respect, in the following chapter, this work will report some key experiments that aimed to reduce a chemically prepared GO colloid using pulsed laser irradiation, demonstrating that this method permits to finely tune the degree of reduction and modulate both the hydrophilicity and the spectroscopic features of the final graphene oxide suspension.

2.2 Synthesis of graphene oxide

Graphene oxide and its synthesis have a history that spans more than a century, also involving the first studies on the chemistry of graphite [41]. Indeed, as already mentioned in the previous chapter, GO "came out" for the first time in 1859 when British chemist sir B. C. Brodie was studying the structure of graphite by analyzing its reactivity. Exactly, he discovered a new strange graphitic material by handling a mush of graphite in fuming nitric acid (HNO3) with "potash of chlorate" (potassium chlorate, $KClO_3$) [37]. Brodie also deduced that the new material was only composed of three elements such as carbon, hydrogen and oxygen, given the resulting increase of the mass of graphite flakes. He even tried to determine the C:H:O composition and then a net molecular formula of the new compound, estimating the first to be 61.04:1.85:37.11, while the second could be written as $C_{2.19}H_{0.80}O_{1.00}$.

In 1899 L. Staudenmaier wanted to refine the Brodie's method for the synthesis of "graphitic acid" by adding the potassium chlorate in multiple aliquots over the course of the reaction rather than in a single addition as Brodie had done. Moreover, he also added concentrated sulfuric acid in order to increase the acidity of the mixture [55, 56]. In

reality, these changes in the synthesis process didn't involve any variation in the C:O composition of the resulting compound (~2:1) with respect to Brodie's approach.
In 1958, Hummers and Offeman devised an alternative oxidation method, which has become the best known and most widely used. It consists in reacting graphite flakes with a slurry of potassium permanganate ($KMnO_4$) and concentrated sulfuric acid [57]. Though permanganate is a common oxidant, in reality, the active specie in the Hummers method is diamanganese heptoxide (Mn_2O_7),

which is formed by the reaction between permanganate and sulfuric acid [41]:

$$\mathbf{KMnO_4 + H_2SO_4 \rightarrow K^+ + MnO_3^+ + H_3O^+ + 3\ HSO_4^-}$$

$$\mathbf{MnO_3^+ + MnO_4^- \rightarrow Mn_2O_7}$$

Over the last decades, several scientists have proposed more or less significant changes to Hummers method. Among these, one of the proposed changes that has found more success has been the addition of hydrogen peroxide at the end of the traditional Hummers process, in order to improve the oxidative action.

In this regard, the solutions of graphene oxide that was used in the various experiments carried out during my research work, were synthesized by the modified Hummers method which was proposed by Laura J. Cote and her research group (Northwestern University, Evanston, Illinois) [58].

This modified approach can be described as follows:

1. 0.5 g of graphite, 0.5 g of sodium nitrate ($NaNO_3$) and 23 mL of H_2SO_4 are stirred together in an ice bath.
2. 3 g of $KMnO_4$ was slowly added.
3. After mixing, the solution is carried to a 35 ± 5°C water bath and stirred for about 1 h, forming a dense paste.
4. Subsequently, 40 mL of water is added and the solution is transferred to 90 ± 5°C for 30 min (stirring).
5. Then, 100 mL of water is added, followed by the addition of 3 mL of H_2O_2 (30%): the color of the solution will turn from darkbrown to yellow.
6. The solution is filtered and washed with 100 mL of water. The filter cake is then dispersed in water by mechanical agitation.
7. Low-speed centrifugation is done at 1000 rpm until all visible particles are removed from the precipitates.

8. The supernatant is then spin-dried by a high-speed centrifugation step at 8000 rpm for 15 min to remove small GO pieces and water-soluble byproducts.
9. The final sediment is re-dispersed in water.

2.3 Structural features of graphene oxide

The chemical structure of graphene oxide is till today the subject of debate, assumptions and conjectures for several different reasons [41]:

i. complexity of the material (e.g. sample-to-sample variability);
ii. nonstoichiometric composition;
iii. the absence of adequate and precise analytical methods, able to perform appropriate characterizations.

The first structural model of a regular lattice of GO was proposed, in 1939, by Hofmann and Holst, which supposed a structure consisted of epoxy groups allocated on the basal plane of the graphene sheet (Fig. 2-2) [59].

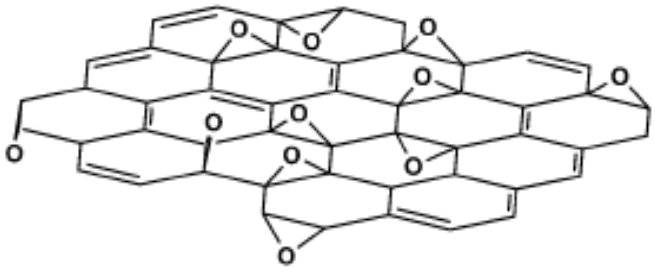

Fig. 2-2 Hofmann-Holst structural model of GO.

In 1946, Ruess suggested to make a change in the model proposed by Hofmann, including also hydroxyl groups into the basal plane, in order to justify the presence of hydrogen content in GO (Fig. 2-3) [60].

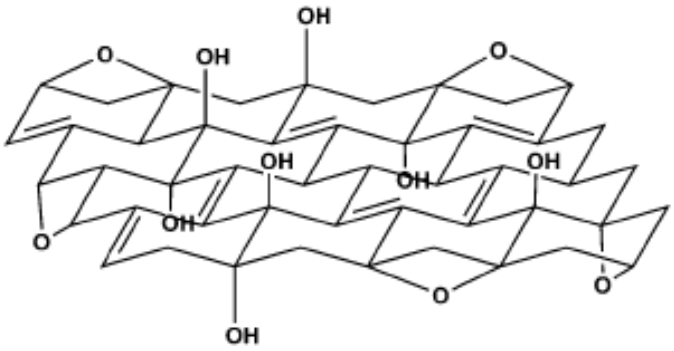

Fig. 2-3 Ruess structural model of GO.

Consequently, the primary structural difference between the two models is the alteration of the characteristic hybridization of the basal plane, which switch from sp^2 in the Hofmann-Holst model to sp^3 in the Ruess model. Moreover, he also proposed a repeat unit consisting of ¼th of the cyclohexanes that include epoxy groups in 1 and 3 positions, and a hydroxyl group in 4 position. In this regard, Marmoux observed that the resulting regular lattice structure can be considered akin to poly(carbon monofluoride), $(CF)_n$, in which the formation of C-F bonds is possible thanks to the total rehybridization of sp^2 planes to sp^3 cyclohexyl structures [61].

In 1969, Scholz and Boehm revolutionized the previous models removing epoxy groups and inserting quinoidal species [62], while Nakajima and Matsuo idealized the GO structure like a lattice framework analogous to the poly(dicarbon monofluoride), $(C_2F)_n$ [63] (Fig. 2-4). Therefore, they described the structure of graphene oxide like a graphite intercalation compound (GIC).

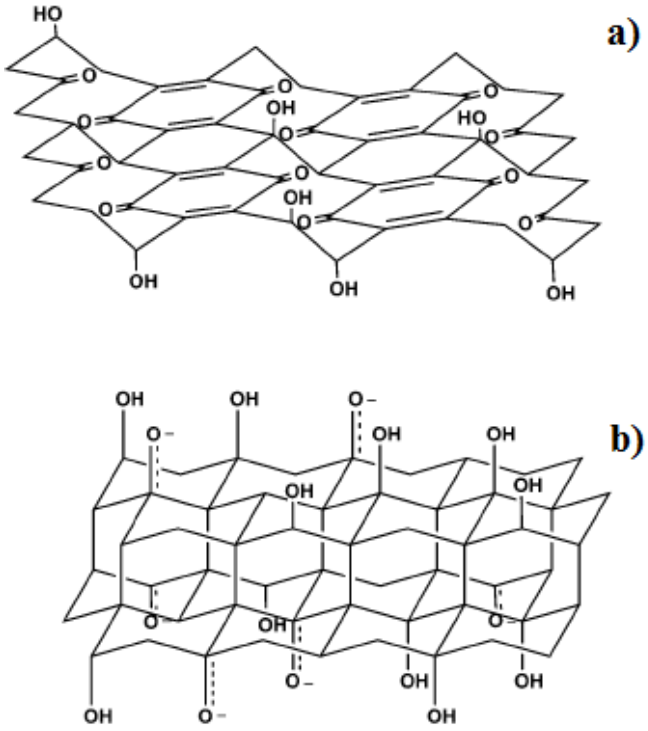

Fig. 2-4 a) Scholz-Boehm model and b) Nakajima-Matsuo model.

All possible structures of GO that have been proposed until a few decades ago are described by lattice-based model, as we have just seen. However, nowadays, the most recent models are based on a nonstoichiometric alternative. The most well-known and mentioned is the Lerf-Klinowski model (Fig. 2-5), build by in-depth solid state nuclear magnetic resonance (NMR) characterizations [64].

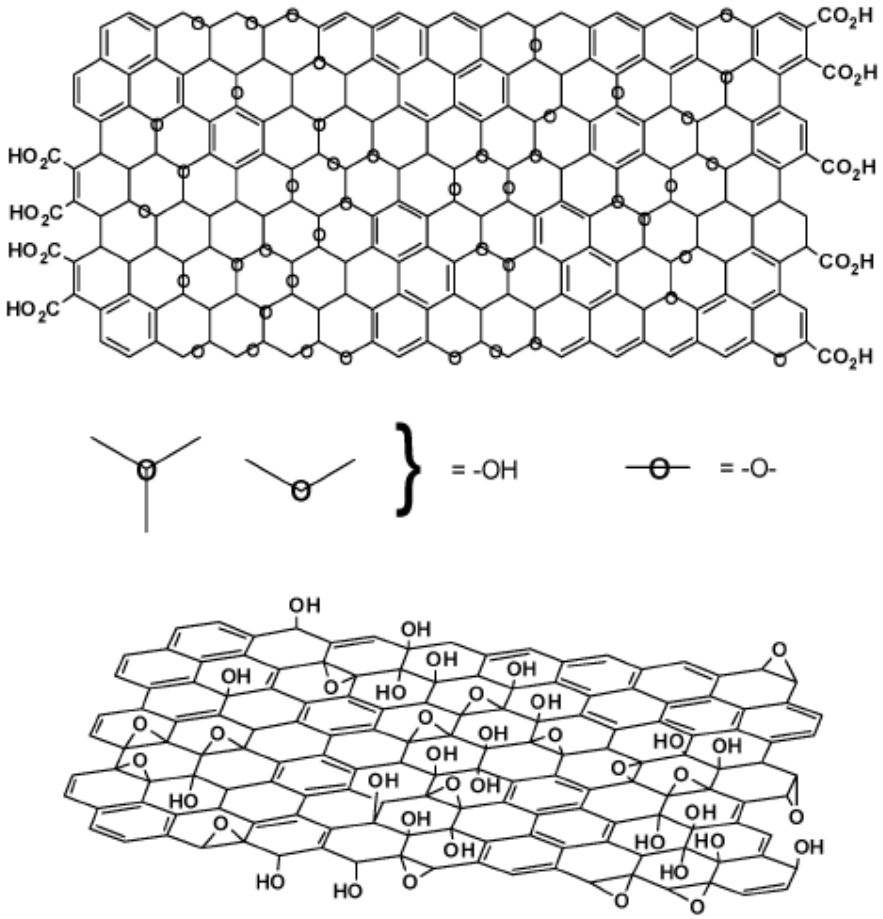

Fig. 2-5 Variations of Lerf-Klinowski model in which it is possible to observe the ambiguity relating to the presence (top, adapted from ref. [65]) or absence (bottom, adapted from ref. [66]) of carboxylic groups on the peripheral zones of the basal planes [41].

The several NMR studies also allowed to note a very strong interaction between water and graphene oxide; exactly, the water is strongly bound to the basal plane of GO through hydrogen bonds that the water establishes with the oxygen of the epoxy groups (Fig. 2-6) [67-68].

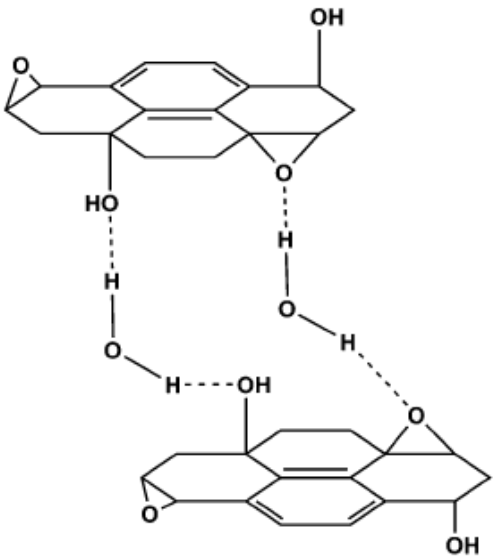

Fig. 2-6 Proposed hydrogen bond between water and graphene oxide.

In recent years, a reevaluation of the FTIR spectra of graphene oxide has been proposed, regarding the signal found at 1714 cm^{-1}. According to Lerf, Klinowski and many other scientists, this peak should be indicative of the presence of carboxylic groups on the periphery of the basal plane of GO (as seen in Fig. 2-5); however, Dèkàny, through

DRIFT spectroscopy [69], suggested to assign the signal to single ketones and/or quinones. In this way, he upstream revisited the Scholz-Boehm model, proponing a regular, corrugated quinoidal structure interrupted by trans-linked cyclohexyl species interspersed with tertiary alcohols and 1,3-ethers (Fig. 2-7) [70].

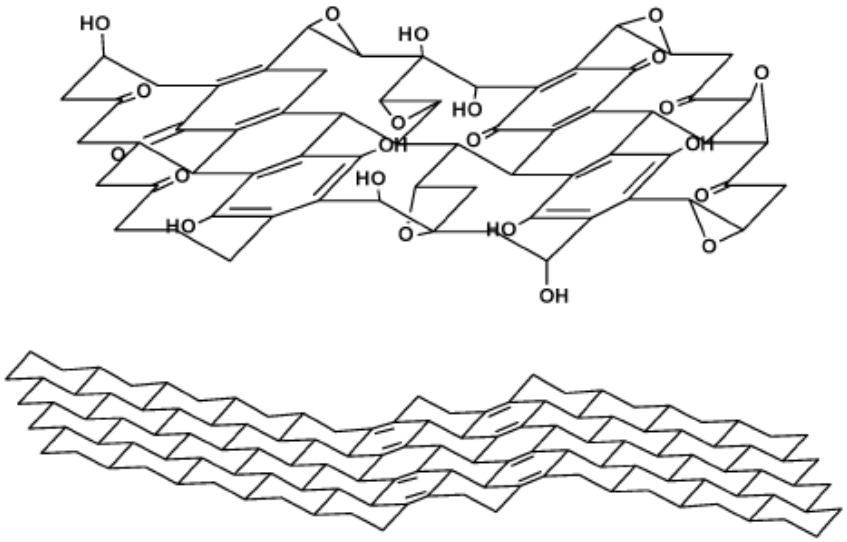

Fig. 2-7 Structure of GO proposed by Dèkàny [70].

However, Dèkàny was in the position of having to justify the results of potentiometric acid-base titrations, which revealed the presence of acid sites on the basal plane of GO [71]. He tried to explain it presuming that α,β-unsaturated ketones undergo a keto-enol isomerization; consequently,

the enol form would justify the acidic proton exchange. Nevertheless, what is being proposed by Dèkàny could be despute by the fact that the keto form is thermodynamically more favored, preventing, thereby, the process of enolization. An exception in case the enols are present in aromatic regions (phenol-quinone exchange).

2.4 Chemical reactivity of graphene oxide: reduction processes

The reduction process is one of the most important reactions of graphene oxide, because of the conspicuous analogies between reduced graphene oxide and pristine graphene. After all, this process is the best way to obtain sizeable quantities of graphene-like materials, by restoring the π-network. The reduction-induced restoration of the typical graphene sp^2 bonding network in GO and the complete or partial removal of the oxygen functional groups imply sensitive changes regarding electrical, thermal, mechanical and morphological properties.
The conventional reduction methods can be divided in chemical, thermal and electrochemical approach.

- *Chemical reduction*

The most-used chemical method consists in the addition of a reducing agent like hydrazine monohydrate (N_2H_4) to a GO dispersion (at 80-100°C) [72,73].

However, it is still not clear what would be the reaction scheme of this reduction process. Initially, the scientists tried to explain the removal of oxygen and, at the same time, the incorporation of nitrogen into the reduced GO, presuming that hydrazine reacts with anhydrides and lactones (formation of hydrazides) and with quinones (formation of hydrazones) [74]. However, only the following reduction of hydrazones can involve a deoxygenation process; further, an hydrazone can undergo a reduction process only if it is adjacent to an epoxy group (Wharton reaction) [75]. Moreover, also the Wolff–Kishner-type reduction of the carbonyl groups is not possible at that low temperature and with a so poorly basic reaction media.

Consequently, one the most reliable mechanistic routes is the follow [73]:

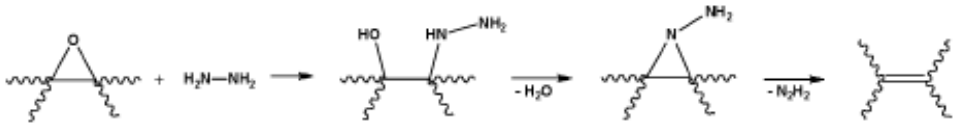

According this scheme, hydrazine would cause the ring-opening of the epoxy groups [76]; the second step could consist in the formation of an aminoaziridine moiety which subsequently undergoes the thermal elimination of a diimide with the consequent formation of a double bond [77,78].

Over the years, other reducing agents have been proposed for the synthesis of reduced graphene oxide: gaseous hydrogen [79], hydroquinone [80] and strongly alkaline solutions [81, 82].

- *Thermally-mediated reduction*

Rather than using a reducing agent to remove oxygen from the surface of graphene oxide, it is possible to reduce it through direct heating in a furnace at 1050°C [83].

The byproducts of the thermally-mediated process are carbon monoxide, water and various hydrocarbons; but the primary byproduct is the carbon dioxide (CO_2), which is exactly what permits the exfoliation of the stacked structure of the reducing GO thanks to the enormous pressure that the high temperature gas creates within the GO layers (above 130 MPa) [84].

- *Electrochemical reduction*

The electrochemical removal of the oxygen functionalities can represent an effective alternative approach to reduce graphene oxide; it avoids the use of dangerous chemical reagents like hydrazine and the obtaining of byproducts, but involves the production of low quantities of reduced GO. Typically, this approach consists in the deposition of thin films of GO on a substrate (ITO, glass, plastic,…); then, the electrodes are putted on the opposite ends of the film and a linear voltage (from -0.60 to 0.87 V) is applied in a sodium phosphate buffer. Normally, the process of reduction is mainly observed during the first 300 s and the reaction scheme can be the following, in which the basic role of hydrogen ions in the buffer solution is pointed out [85]:

$$\underset{\text{Oxide}}{\text{Graphene}} + aH^+ + be^- \longrightarrow \underset{\text{Oxide}}{\text{Reduced Graphene}} + cH_2O$$

- *An alternative approach: photo-induced reduction*

In the last few years, several groups have preferred a novel and interesting alternative method to obtain reduced graphene oxide, consisting in photoirradiating processes

(UV-induced photocatalytic reductions [51, 52], photothermal treatments by pulsed Xenon flash [53] or selective reduction by direct laser writing [54]).

In the following chapters, it will be propose an innovative method of photo-induced reduction that provides the use of pulsed laser irradiation processes in order to synthesize reduced GO colloids (rGO) characterized by different reduction degrees [86].

Chapter 3. Laser irradiation: a novel approach to reduce graphene oxide

3.1 LASERs and matter

The laser is often considered a real landmark invention of the middle of the last century, like the transistor and the computer [87].

Lasers had a rich and complex history and, although their potential seems obvious today, at first it was not clear.

The first conceptual contribution to lasers was given by Albert Einstein that, in 1917, introduced the idea of lasing action, proposing the theory of stimulated emission of light, according to which photons could stimulate emission of identical photons from excited atoms [88].

In 1928, R. Ladenburg reported indirect evidence of stimulated emission [89] that physicists of the time named “negative absorption”; however, they considered it only a phenomenon of little practical importance, considering Boltzmann population distribution was the norm, with higher energy states that are inevitably less populated than lower states. Three decades later, in 1958, a new theory, based on an extension of the concept of MASER (Microwave Amplification by Stimulated Emission of Radiation) to

optical frequencies, was proposed by Schawlow and Townes [90], increasing the interest about the phenomenon. Two years later, in 1960, Theodor Maiman constructed the first functional laser (with ruby as active medium) at Hughes Research Laboratories [91, 92].

From then on, lasers have been largely used in a considerable range of science and technological fields; in particular, with the development of high power laser systems, the prospects of laser–matter interaction and, consequently, laser-induced material processing came into being [93-95].

The primary "eye-visible" effect of laser action on matter was the removal of some material from a solid target surface within the laser spot; this process was called "laser ablation", from Latin *ablatio*, which means "removal" [96].

Today, Pulsed Laser Ablation (PLA) is one of the most important techniques used to fabricate nano-sized materials, consisting in an explosive evaporation of solid materials by strong pulsed laser irradiation. Nowadays, this method is largely used for fabrication of thin films ("laser deposition") and nanoparticles (NPs) or for micromachining.

Initially, laser ablation was generally carried out for targets set in a gas or vacuum, in order to avoid unwanted effects like deactivation or oxidation of ejected materials. However, in the space of a decade, many research groups

demonstrated that a laser ablation process can be performed in liquids such as water and organic solvent. The studies on laser ablation in liquids for material processing were unexplored until 1987, when Patil et al. first studied and reported the laser matter interaction at solid–liquid interface [96].

In comparison with the conventional physical and chemical methods (e.g. chemical vapor deposition [97], vapor phase transport [98], pulsed laser ablation in vacuum, hydrothermal methods [99], soft-template [100]) the technique of PLAL has many distinct advantages:

i. a synthesis that is chemically simple and “clean”;
ii. the final product is usually obtained without by-products and no need for further purification;
iii. low cost of experimental setup and easily controlled parameters;
iv. the extreme confined conditions and the induced high temperature and high pressure region further the synthesis of unusual metastable phases.

Fig. 3-1 shows a typical example of set-up for PLAL experiments. Obviously, this setup may vary from one research group to another though their common characteristics are the same [96].

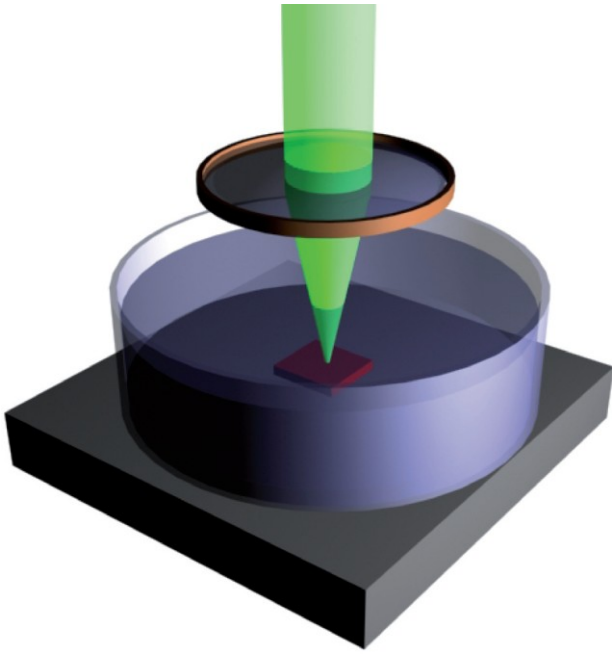

Fig. 3-1 Experimental setup for laser ablation of solids in a liquid environment (taken from ref. [96]).

Although the fundamental mechanism regarding nanostructure formation by laser ablation in liquid is still not fully understood, according to several studies, interaction between pulsed laser light and the target initially generates a local high-temperature and high-pressure plasma plumes above the target surface. Such a phenomenon is the basis of laser ablation process and it can be possible only if the value of laser fluence (J/cm^2)

is above a threshold that depends on laser wavelength, solvent and material of target.

After the formation of the laser-induced plasma, a process of clustering starts into a so-called “cavitation bubble”, which is formed by the expansion of ejected materials and the local heating of the solvent in the vicinity of the ablation spot. The formation of clusters into the cavitation bubble involves a following process of aggregation. When the pressure conditions become so drastic, the cavitation bubble collapses, with a consequent propagation of a shockwave and ejection of materials [101, 102] (Fig. 3-2).

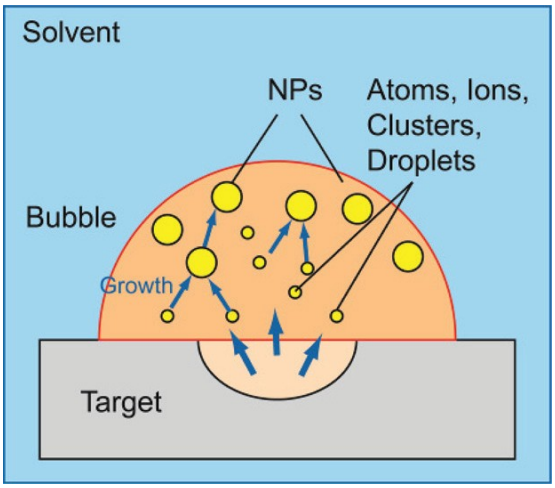

Fig. 3-2 Growth of NPs inside the cavitation bubble (taken from ref. [96]).

Summarizing, the formation mechanisms of NPs in LAL can be described as follows [96]:

i. There will be at least three formation processes of NPs.
   (a) Direct laser ablation process;
   (b) Secondary etching process by high pressure of confined plasma;
   (c) Secondary etching process by high pressure generated by the collapse of the cavitation bubble.
ii. All materials ejected through the above processes are involved in the cavitation bubble, and NPs will grow inside the bubble.

It is known that, by using different target materials and solvents, and varying parameters such as the laser wavelength, fluence, and pulse duration, PLAL permits to produce a wide variety of nanomaterials; moreover, by modulating the above parameters, it is also possible to vary size and shape of nanoparticles.

Even if Laser Ablation of solid targets is one of the most interesting today's applications of lasers, the laser irradiation of suspended nanomaterials is becoming a rapidly growing field, in order to modify their size, shape, and composition [93]. In this case, the laser beam (oft-unfocused) is used under-threshold and the irradiation

mechanism is tendentially of thermal nature: a photo-induced thermal process that is able to generate localized heating and/or melting/vaporization of suspended nanosystems.

Depending to the nature of the nanomaterials and laser parameters, a laser irradiation process can be used for different goals:

1. Shape and size modifications of NPs in suspension. In this respect, two mechanisms were proposed: the first consists in a melting-evaporation mechanism, in which the laser induces melting and/or vaporization of larger sized particles into atoms or molecules that, afterwards, rearrange into smaller nanostructures with the same or different shapes and crystal structures [93,103-105]. The second proposed mechanism consists in a laser-induced Columbic explosion that involves the ejection of photoelectrons or thermal electrons from the surfaces of target nanostructures, leaving positive charges behind on the surface. These laser-induced charges generate an electrostatic repulsion between different parts of the primary particles, thus causing a consequent fragmentation of the single particle into several smaller ones. [93,106-108].

2. Synthesis of NPs via laser irradiation of solutions with precursors. Laser irradiation of aqueous metal salts or liquid precursors is an interesting bottom-up method that can form colloidal suspensions of NPs [109-111]. For example, metal salts are first photochemically induced to generate neutral M^0 atoms, which then form clusters and, then, nanoparticles. Fig. 3-3 shows a direct photoreduction and a photosensitized reduction mechanism for the photochemical synthesis of NPs from solutions with precursors.

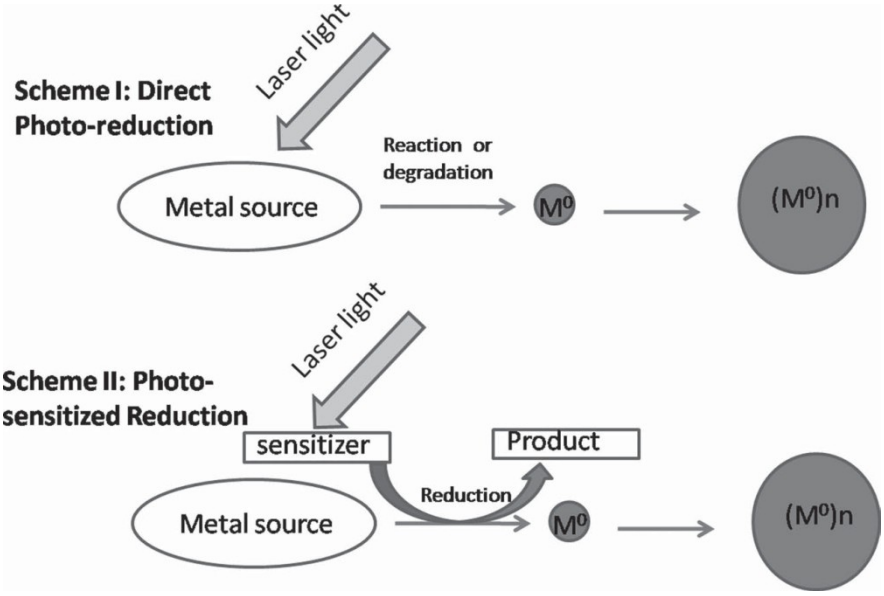

Fig. 3-3 Schemes for direct photoreduction and photosensitized reduction of metal salt solution or liquid precursors (taken from ref. [112]).

3. Laser-induced alloying. The irradiation of a mixture of two (or more) colloids of elemental NPs can melt or vaporize them, thus making the formation of their alloys. A typical example is the preparation of Ag:Au alloy NPs with different composition mixing and, then, irradiating Ag and Au colloids in different proportions [113,114].
4. Laser-induced chemical modification of nanosystems. The photo-induced thermal effects can modify the chemical and structural nature of the surface of suspended NPs; for instance, the laser irradiation may generate reductive or oxidative phenomena with consequent variations or removal of functional groups and changes in the chemical structure. Against this backdrop, it is also possible to integrate laser irradiation processes of graphene oxide suspensions, which undergo a laser-induced reduction. This mechanism, at the heart of my PhD thesis, consists in the size increase of the sp^2 hybridized regions, because of the modification/removal of the oxygen functional groups (similar to a solvothermal reduction [115]). As will be shown in the following pages, laser irradiation is a simple method for the reduction of graphene oxide sheets by the action of a pulsed laser at visible wavelengths. Such a method has essentially

three advantages, which make it potentially important for many fields, like electronic packaging and water purification:

- it is greener than other approaches;
- it involves the graphene oxide sheets directly in solution, with negligible overall temperature increase;
- it can easily permit to modulate the degree of reduction of graphene oxide during the laser irradiation process.

3.2 Laser processes in liquids for the preparation of carbon based nanomaterials

In addition to the novel approach of laser-induced reduction of graphene oxide that will be discussed in par. 3.3, lasers can be successfully used for the synthesis and/or the modification of several carbon based materials. Here some important examples are quickly described [116].

Laser exfoliation of graphite

Generally, the exfoliation of graphite is carried through mechanical (scotch tape) or chemical processes (intercalation of certain compounds within the layers).

However, recently an alternative top down approach has been proposed to break the weak van der Waals forces that stack the graphite layers together: laser exfoliation.
According to Jeschke [117] graphite is characterized by two different ablation mechanisms: at low fluence conditions it exhibits an exfoliation process, while the high fluence threshold implies a series of bond breaking phenomena inside the graphite layers.
Recently, my research group proposed a novel method for the synthesis of graphene by pulsed laser ablation in water of an HOPG target (highly oriented pyrolytic graphite). The ablation process was performed using the second harmonic (532 nm, 5 ns pulse and 10 Hz repetition rate) of a neodymium-doped yttrium aluminum garnet laser (Nd:YAG) employing different fluences. During the experiments, three phases are observed (Fig. 3.4):

- at low fluences (below 5 J/cm^2) the ablation process produced molecular species, recognizable as hydrogen-terminated polyynes with relatively short length [118].
- at fluences between 5 and 10 J/cm^2, the UV spectrum showed the formation of species that are characterized by an absorption signal at around 260 nm. This intense absorption can be attributed to the

presence of graphene quantum dots (GQDs) [119] or graphene nanosheets [120].

- At fluences higher than 10 J/cm^2 some fluctuating layered materials appeared at the water-air interface; the several characterizations revealed that these suspended objects show a moderate oxidation, labelling them as reduced graphene oxide.

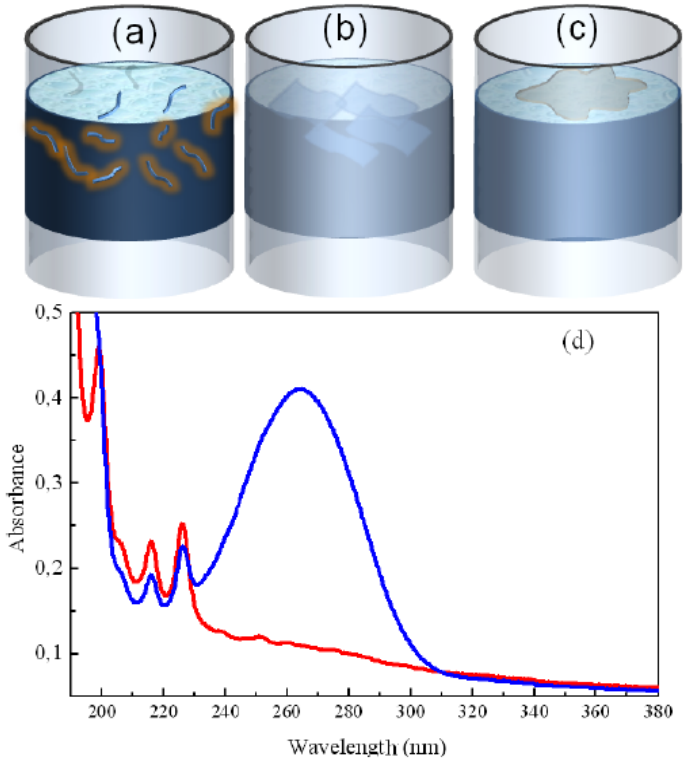

Fig. 3.4 (a-c) Schematic representation of the three phases of the laser ablation of graphite in water; (d) Absorbance spectra for low (red) and high (blue) fluence (taken from ref. [116]).

Electric field-assisted laser ablation of carbon in water

During a typical laser ablation process, the produced plasma also contains electrons and ions, which can be driven by an external and/or a magnetic field that, applied to the plasma plume, can influence:

- the kinetics of reactions at the plasma/liquid interface;
- the clustering processes;
- the assembly of NPs into larger nanostructures.

Moreover, since the surface of the nanoparticles is charged, the application of an external electric or magnetic field can modulate their size and shape.

At the same time, based on the above, an external electric field can be applied to drive the building blocks that were previously obtained by laser ablation. This is what my research group did, applying an external electric field to a suspension of polyynes, produced by pulsed laser ablation of graphite in water (with a laser fluence of 5 J/cm^2 and an irradiation time of 30 min), using the second harmonic of a Nd:YAG laser beam.

It was observed that, applying an external electric field (30 V DC potential) to two HOPG electrodes submerged into the polyynes suspension, the building blocks (the polyynes) are forced to move towards the electrodes (electrophoresis),

starting to grow perpendicular to the electrode surface and giving a new kind of nanostructure: graphene nanowalls (GNWs) (Fig. 3-5) [116].

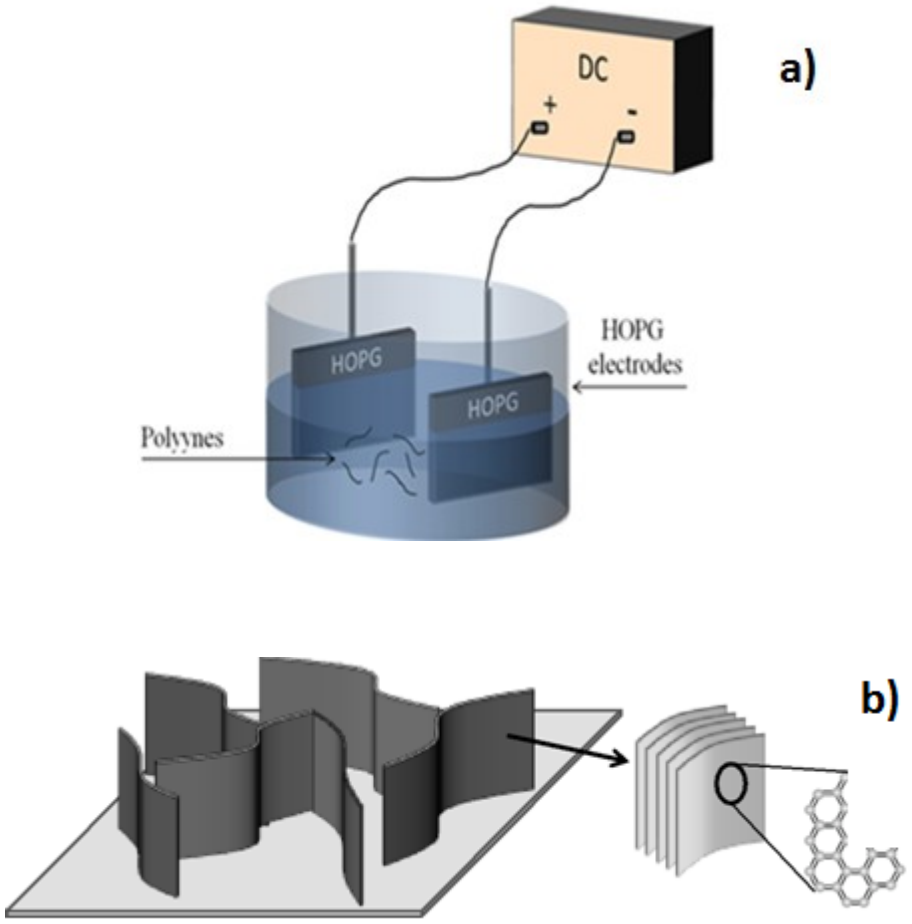

Fig. 3-5 a) Schematic representation of the application of an external electric field to a polyynes suspension after PLA (taken from ref. [128]); b) Schematic illustration of graphene nanowalls (taken from ref. [121]).

Novel method for the synthesis of porous graphene (PG) and graphene quantum dots (GQDs)

Very recently, P. Russo and Y.N. Zhou developed a new top down method for the synthesis of PG and GQDs, exploiting the action of a femtosecond laser onto a graphite target in water [116]. Specifically, after performing a laser ablation process at 25 J/cm^2, they observed the presence of large layers that floated at the water-air interface.

Atomic force microscopy (AFM) and field emission scanning electron microscopy imaging (FEI) analysis permitted to observe some interesting features of these carbon nanostructures; in particular, FEI images showed that the sheets had many ripples on the surface. Moreover, high magnification images can permit to observe the presence of a huge quantity of pores, which are ~10-20 nm in size (Fig. 3-6).

In reality, the absorption spectrum of the solution obtained after the femtosecond laser ablation process at 25 J/cm^2 also showed the presence of an absorption peak at 270 nm, which may be assigned to GQDs [122].

Summarizing, the perform of a femtosecond laser to ablate a graphite target in water at fluences > 20 J/cm^2 involves the parallel formation of porous graphene and graphene quantum dots.

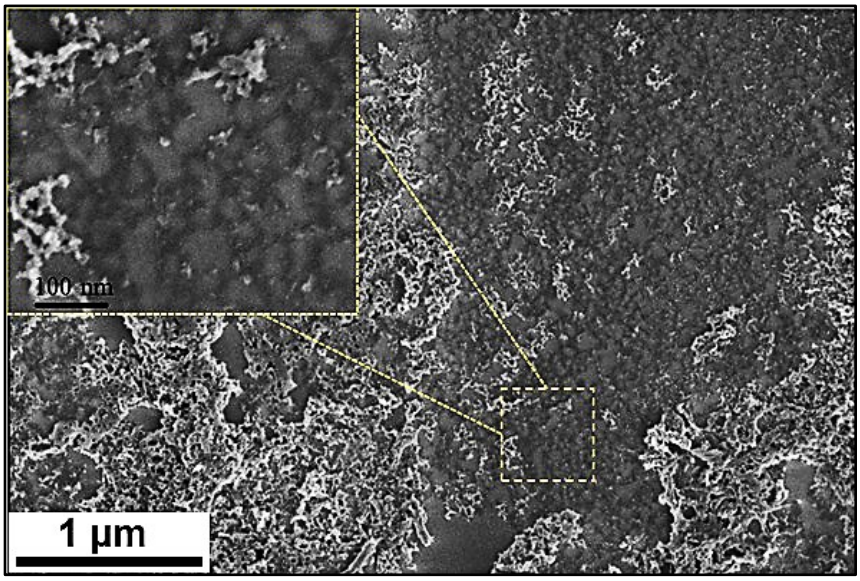

Fig. 3-6 FEI image of a single layer of porous graphene (taken from ref. [116]).

3.3 A novel method for GO reduction: Laser irradiation approach

As we have seen in the earlier paragraphs, laser irradiation of nanomaterials in suspension is acquiring a notable importance for the modification of shape, size and composition of NPs.

During my PhD, laser irradiation processes were used in order to realize a novel and interesting approach to

synthesize reduced graphene oxides. Specifically, I will report some key experiments that aimed to reduce a chemically prepared GO colloid using pulsed laser irradiation, demonstrating that this method is able to finely tune the degree of reduction of rGO and, consequently, its properties.

Graphene oxide aqueous suspensions were synthesized by the modified Hummers method (as described in the chapter 2), consisting in a strong oxidation of graphite powder provided using sulfuric acid, potassium permanganate and hydrogen peroxide [58].
The obtained GO solution was subjected to a laser irradiation process, under continuous stirring, in order to obtain reduced graphene oxide (rGO). For such a process, we used the second harmonic (532 nm) radiation of a Nd:YAG pulsed laser system (Continuum, Surelite II model) operating with a pulse duration of 5 ns and a repetition rate of 10 Hz. The laser beam size was around 28 mm^2, and it was directed toward the GO solution without any focusing lens (Fig. 3-7).

Fig. 3.7 Experimental apparatus used for laser irradiation process of GO.

The GO suspension was irradiated homogeneously at a constant fluence of 0.32 J/cm^2 for different times ranging between 15 and 300 min (Fig. 3-8).

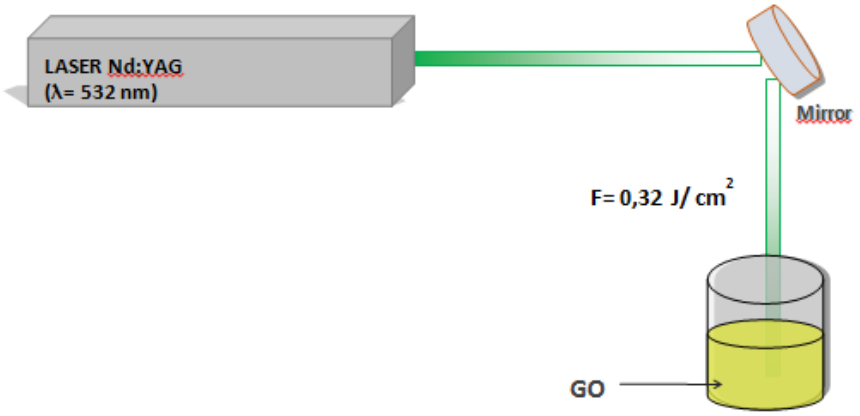

Fig. 3-8 Experimental setup for laser irradiation process of GO.

It has been observed that greater fluences (above 0.5 J/cm^2) cause a deep modification of the sheet morphology since a plasma is ignited into the colloidal solution, while with lower fluences we need very long irradiation times to obtain similar results.

Typically, a slightly diluted GO colloidal solution shows a pale yellow coloration. But the laser irradiation process leads to a gradual browning of the GO suspension, which is the first clue of the laser-induced reduction (Fig. 3-9).

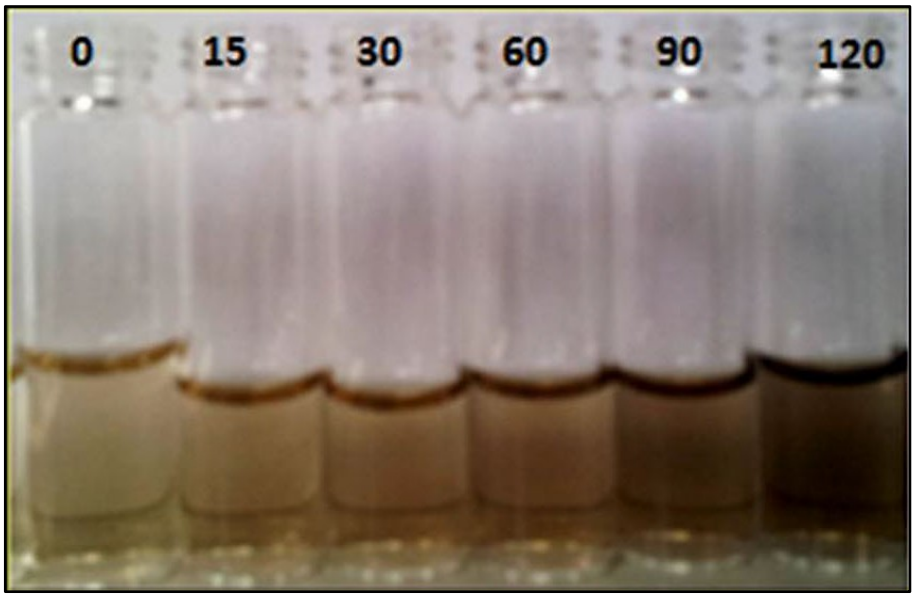

Fig. 3-9 An example of image of GO suspension upon increasing the laser irradiation time.

The observed change in color from light yellow to brown indicates increased light absorption in the visible and NIR region due to the partial restoration of the network within the carbon structure [86].

The use of the second harmonic (532 nm) radiation of a Nd:YAG pulsed laser, rather than an UV radiation as in literature, permits to obtain several solutions with a different degree of reduction, thanks to a more gradual and light laser-induced reduction process of GO.

Chapter 4. Tunable properties of laser reduced graphene oxides

4.1 Spectroscopic characterization

4.1.1 UV-visible Spectroscopy

UV–Vis analysis was carried out using a Perkin Elmer lambda 2 Spectrometer in the range 190–900 nm.

In the absorption spectra (Fig. 4-1), we can clearly distinguish a peak at about 230 nm, corresponding to p–p* transitions of C=C bonds and a shoulder at around 300 nm, due to the n–p* transitions of the C=O bond in sp^3 hybrid regions [123]. A redshift up to 240 nm and an increase of the absorption over the entire spectral region are observed for the reduced layers. This fact can be explained with an increase of the sp^2 hybridized regions after irradiation and is consistent with the disappearance of the C=O signal at 300 nm (partial restoration of the network within the carbon structure) [86].

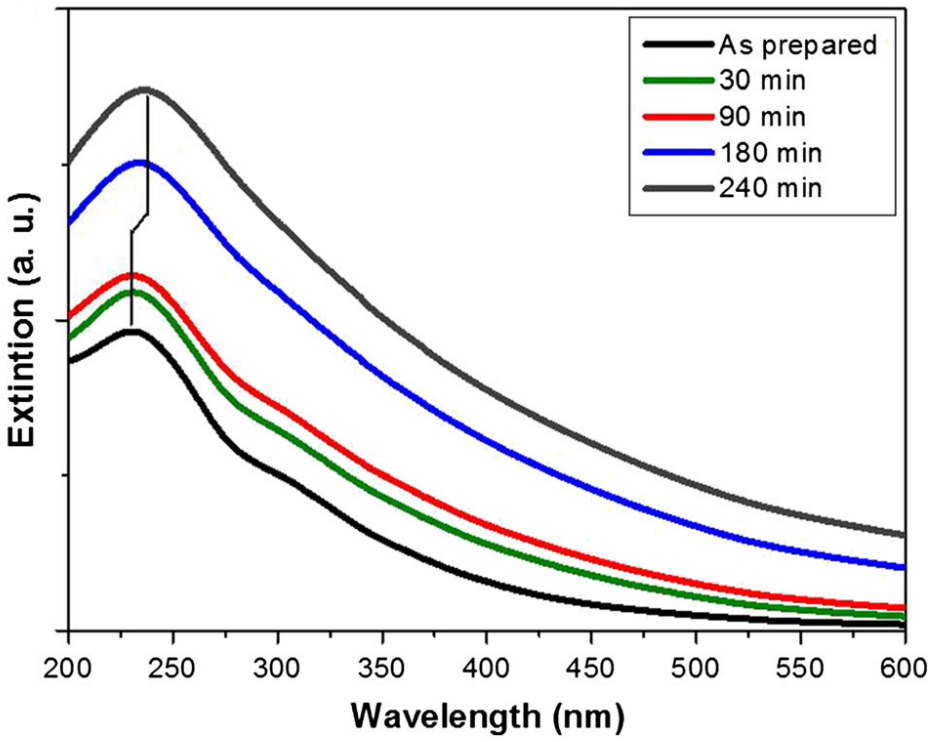

Fig. 4-1 UV–vis spectra of GO suspension upon increasing the laser irradiation time.

4.1.2 FT-infrared Spectroscopy

Such an extinction spectrum is corroborated by the FTIR spectra presented in Fig. 4-2.

Fourier transform infrared (FT-IR) spectra were performed using a Bruker Equinox 55 Spectrometer.

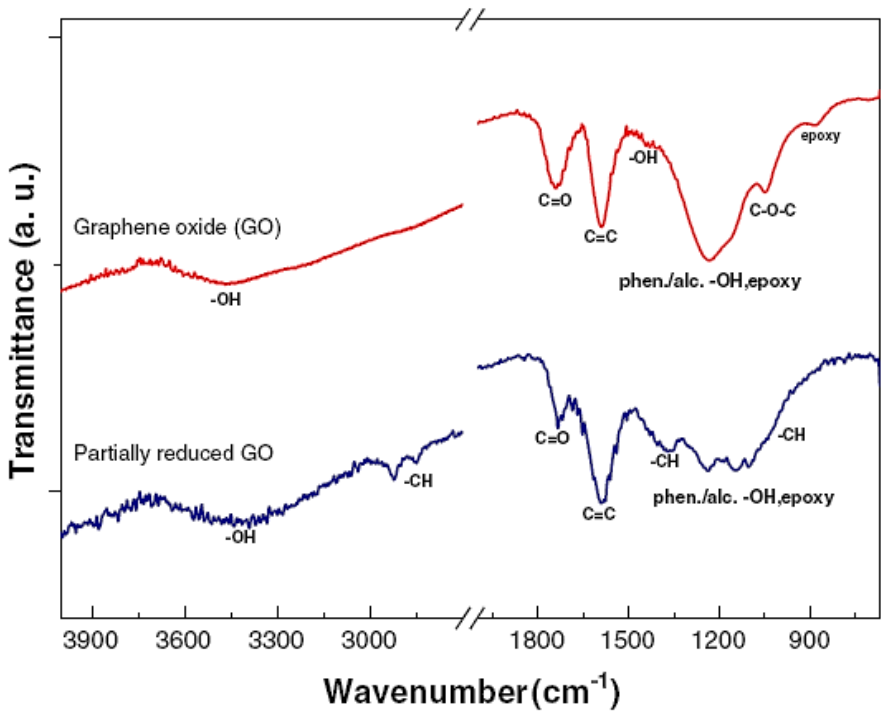

Fig. 4-2 FT-IR spectra of GO and partially reduced GO.

As-prepared GO shows characteristic OH (3420 cm^{-1}), C=O (1735 cm^{-1}), aromatic C=C (1622 cm^{-1}), epoxy (1220 cm^{-1}) and C–O (1110 cm^{-1}) signals [50]. After the laser treatment, most of them are reduced significantly, while mild CH stretching signals appear (2800 cm^{-1}). Moreover, signals at 1050 and 890 cm^{-1}, also related to epoxy functionalities, are removed. The peak at 1573 cm^{-1}, attributed to the aromatic C=C group, still exists and appears prominent as

consequence of the oxygen-rich functionalities removal and the restoration of the sp^2 hybrid regions.
Similar results have been obtained by X-ray photoelectron spectroscopy.

4.1.3 X-ray photoelectron Spectroscopy

X-ray photoelectron spectroscopy (XPS) analyses were performed using a PHI ESCA/SAM 5600 Multy technique spectrometer equipped with a monochromatized AlKα X-ray source operating at 250 W at a base pressure of 10^{-10} mbar. For this reason, some drops of the GO solution have been deposited onto a silicon substrate.
Fig. 4-3 shows the C1s XPS peak of GO that provides a fingerprint of the degree of oxidation of the surface. The peak shape suggests the presence of different oxygen functional groups. Three main different components can be clearly identified. One at 284.5 eV is attributed to C–C species, while the one at 287 eV is due to the presence of epoxy, hydroxyl (C–O) groups. The last component at 289 eV reveals the presence of carboxylated species (O–C=O) [41]. As for the FTIR analysis, the C1s XPS spectrum of the reduced GO exhibits the same oxygen functionalities, but their intensities are greatly reduced.

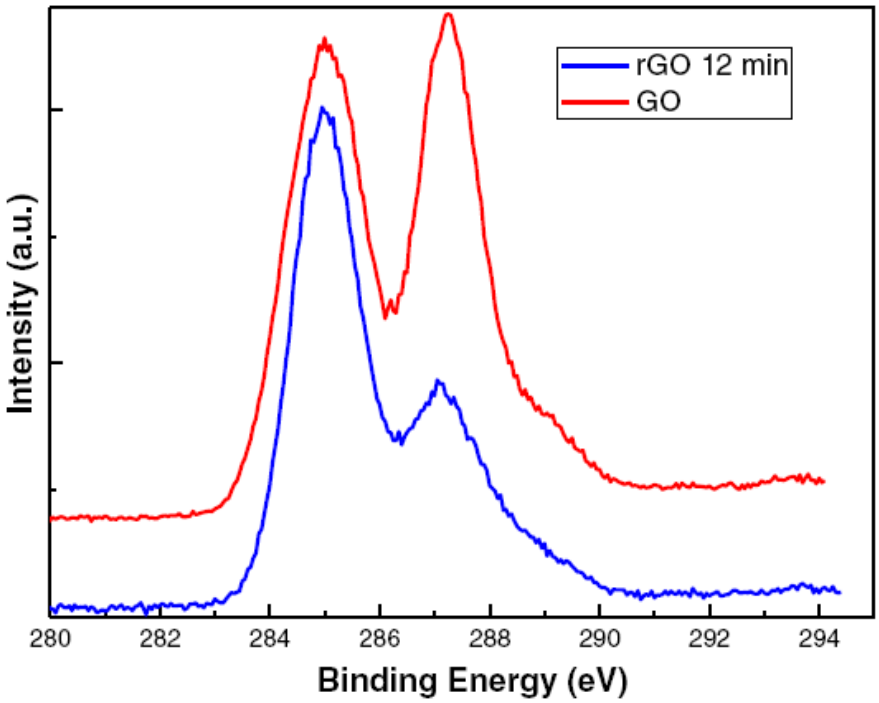

Fig. 4-3 XPS spectra of GO and partially reduced GO.

4.1.4 Raman Spectroscopy

Normally, Raman spectroscopy is very important tool for the characterization of carbon based materials and, compared with other techniques, is a quick, nondestructive and effective way for the characterization of graphene layers.

In Fig. 4-4 it is interesting to note that, as soon as the irradiation process starts (15 min late), the disorder-induced D-band shifts from 1359 to 1365 cm^{-1}, while the G band undergoes a shift from 1617 to 1608 cm^{-1}.

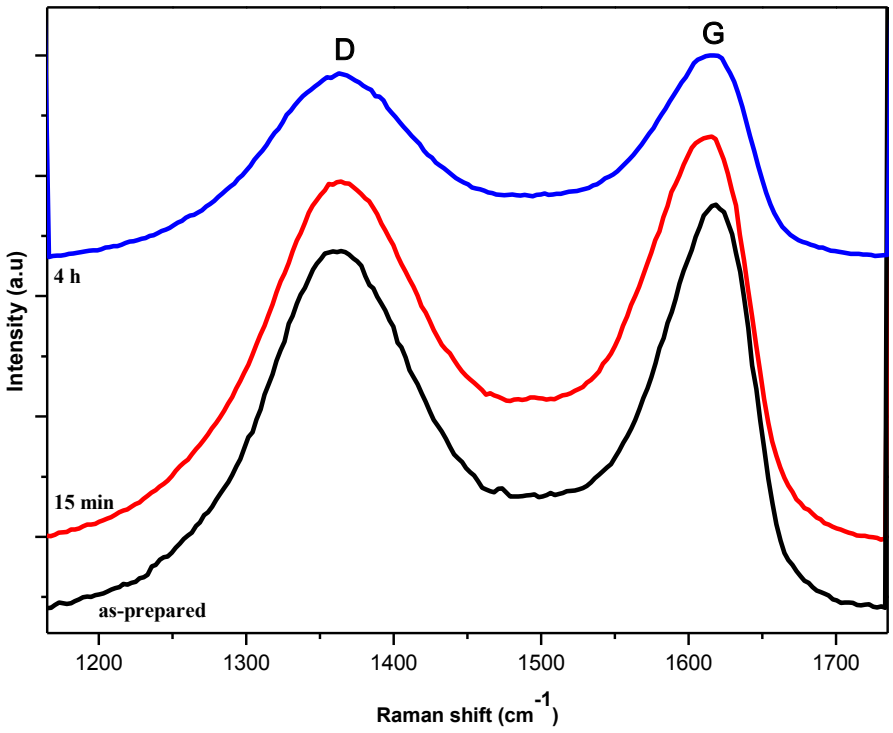

Fig. 4-4 Raman spectrum of GO and partially reduced GO.

These Raman shifts can be related to the decrease of bond disorder during the laser-induced reduction because of the increase the sp^2 contribute.

But, at the same time, it is possible to observe that, after four hours of laser irradiation, the D-peak re-shifts to 1361 cm^{-1}, while the G-peak is back to 1615 cm^{-1}. It can be allocated to clustering phenomena of sp^2 regions.
Another important parameter in Raman spectroscopy is the intensity ratio I_D/I_G that, according to the Tuinstra-Koenig equation, is correlated with the average size of sp^2 domains [124,125]:

$$\mathbf{I_D/I_G = C(\lambda)/L_a(\text{Å})}$$

where $C(\lambda)$ is a Raman wavelength-dependent constant, while L_a correspond to the average size of graphene sites.
Through the Raman experimental data and the above equation it is qualitatively possible to assert that, at least for the first hours of laser irradiation, the average size of hybridized sp^2 sites decreases.
This peculiarity will be confirmed and explained through other characterizations techniques in the following sub-paragraph.

4.1.5 Tunable photoluminescence properties and tunability of energy gap

The progressive change of the backbone structure of graphene oxide layers has implication in one of the most intriguing properties of GOs that is the radiative recombination of electron–hole pairs in the isolated small sp^2 clusters, which causes fluorescence in the UV–Vis region.

This offers unique routes toward solution-processable optoelectronic devices with graphene and graphene-based composites [126].

My experiments, conducted through a Varian Cary Eclipse Fluorescence Spectrophotometer (collected at 90°), show that using a 325-nm excitation wavelength, GO has an initial broad luminescence at 560 nm (180 nm FWHM) which progressively blueshift up to a value of 450 nm (100 nm FWHM). This has been reported in Fig. 4-5 plotting some normalized spectra and reporting (inset) the behavior of the luminescence position and intensity as a function of the reduction time. The trend resembles a first-order kinetics, and the data have been fitted with an exponential functional form giving 50 and 20 min as a time constant, respectively.

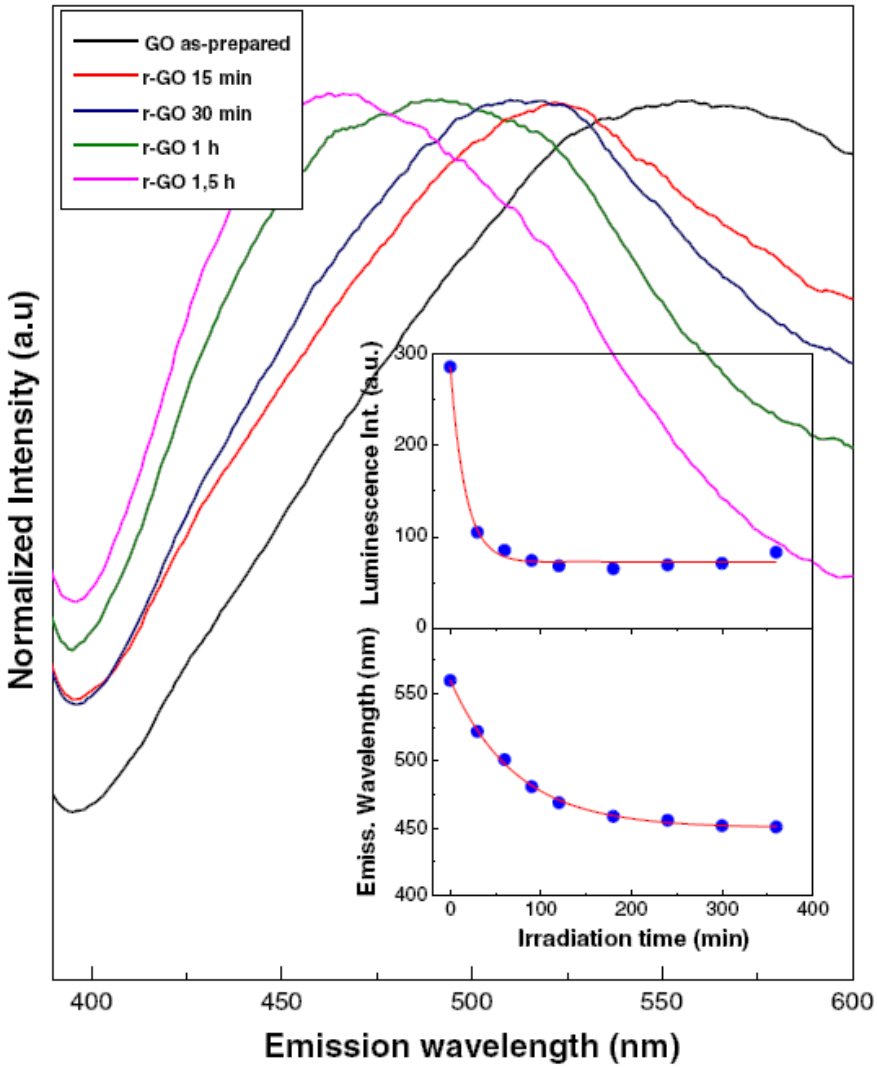

Fig. 4-5 PL of GO and rGO irradiated at different times. The inset reports a detailed change of position and intensity of the emitted luminescence.

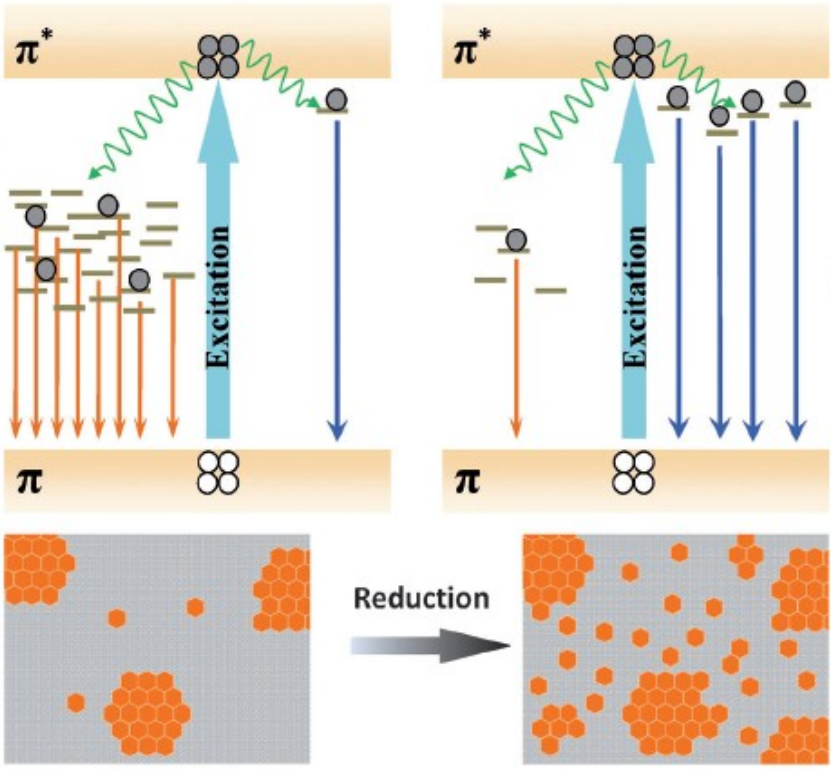

Fig. 4-6 Proposed PL emission mechanisms that explain the evolution of photoluminescence of GO with increased reduction (taken from ref. [126]).

The broad emission band in the as-prepared GO is generally attributed to optical transitions from disorder-induced localized states. During the reduction process, the number of these disorder-induced states within the л-л* gap decreases so that the intensity of the emission is reduced. At the same time, the reduction of GO leads to the

formation of distorted sp^2 domains, which gives the formation of new small graphitic sites. As previously reported in literature [126,127], the initially present sp^2 domains in GO do not increase in size with reduction. Instead, the reduction of GO usually leads to the creation of newly formed smaller sp^2 clusters (confirming the Raman results), which create new isolated states inside the band gap that are liable for the photoluminescence and its blueshift in the reduced graphene oxides (Fig. 4-6).

The small sp^2 clusters that create the above new isolated molecular states could eventually percolate to mediate the transport of carriers by hopping. Therefore, the electron–hole recombination among the confined cluster states originating from these small and isolated sp^2 domains may lead to excitonic features such as those found in an organic light-emitting molecular semiconductor [126,128].

However, it should also be underlined that the emission spectrum of GO and rGOs and its blueshift, on one hand, permits to have important information about the formation of the new smaller sp^2 domains during the laser-induced reduction and the consequent creation of the new isolated states inside the energy gap but, on the other hand, it cannot give us fully correct and unambiguous information about the variation of the average energy gap of the system.

This is true because the emission phenomena of GO and rGOs do not result from direct HOMO-LUMO transitions but, rather, from a series of transitions that involve the isolated trapped states inside the band gap.

Therefore, an important tool that permit us to observe the variation of the energy gap during as the function of the laser irradiation time of graphene oxide is “Tauc plot”, which is obtained by a rehash of the absorption spectra (the absorption phenomenon consists in a direct transition, from the valence band to the conduction band!).

A Tauc plot is used to determine the value of band gap (Tauc gap) in semiconductors [129] and, typically, is characterized by the quantity hν (the energy of the light) on the abscissa and the quantity $(\alpha h\nu)^{1/r}$ on the ordinate, where α is the absorption coefficient of the material. Instead, the value of the exponent r depends on the nature of the transition (r=1/2 for direct allowed transitions).

The Tauc plot in Fig. 4.7 shows that the as-prepared GO has an average energy gap of 2,2 eV; instead, the band gap of the reduced graphene oxides results greatly lower. In detail, as expected, we can observe a gradual decrease of the energy gap as the function of the irradiation time and, consequently, as the function of its degree of reduction, even obtaining a value of 0,8 eV after three hours of laser irradiation.

This plot fully confirms the increase of the conductive feature of reduced graphene oxides with the increase of their degree of reduction.

These results, also confirmed through electrical characterizations (par. 4.4), are extremely important for several applications, including electronic packaging.

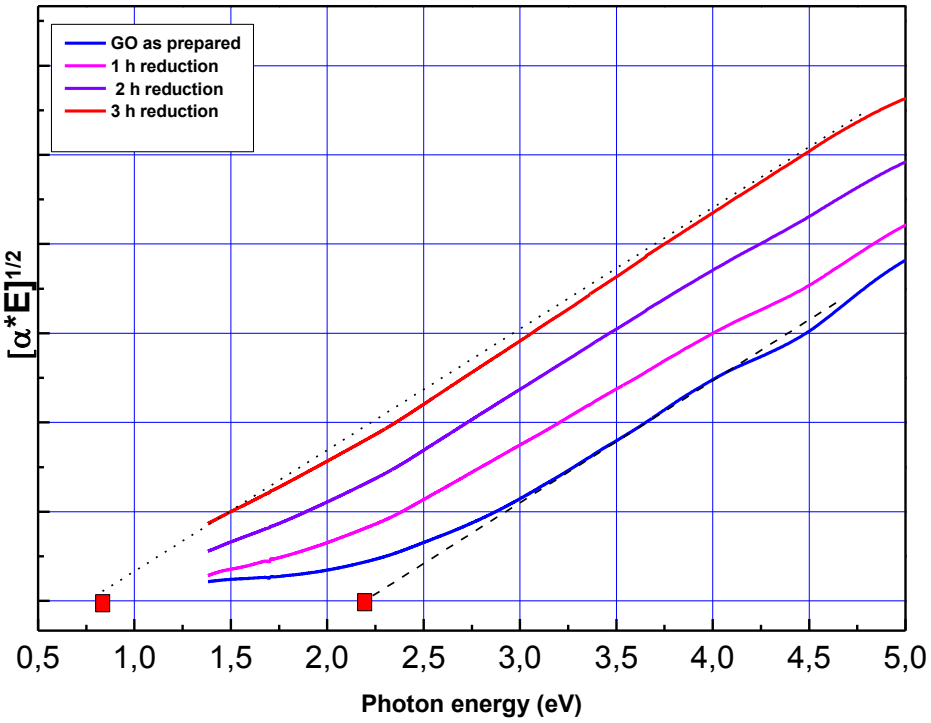

Fig. 4.7 Tauc Plots of GO and rGO at different irradiation times.

4.2 ζ-potential analysis

Such an increase in the graphitized portion of the graphene oxide backbone should have consequences in the layer hydrophobicity. First of all, we have checked this property looking at the surface charge of the GO sheet in solution, measuring the ζ-potential values of the colloid before and after each reduction process.

Each sheet of GO is negatively charged (less than -60 mV for the as-prepared sample) when dispersed in aqueous solution due to the ionization/hydrolysis of oxygen groups. The stability of aqueous GO colloids was, therefore, attributed to electrostatic repulsion rather than hydrophilic interaction [130].

ζ-potential measurements were obtained using an Horiba Scientific NanoParticle Analyzer SZ-100-Z and the results induced by laser irradiation are depicted in Fig. 4.8 as a function of the irradiation time.

ζ-potential values increase up to a saturation at around -50 mV. Since objects with ζ-potentials more positive than +30 mV or more negative than -30 mV are considered to form stable dispersions [131], these measurements confirm the observed macroscopic stability of the suspension at any irradiation time.

Moreover, the evolution of the ζ-potential measurements follows an exponential behavior as a function of time, similar to the one already shown for the luminescence blueshift and indicating a correlation between surface charge properties and graphitization of the backbone.

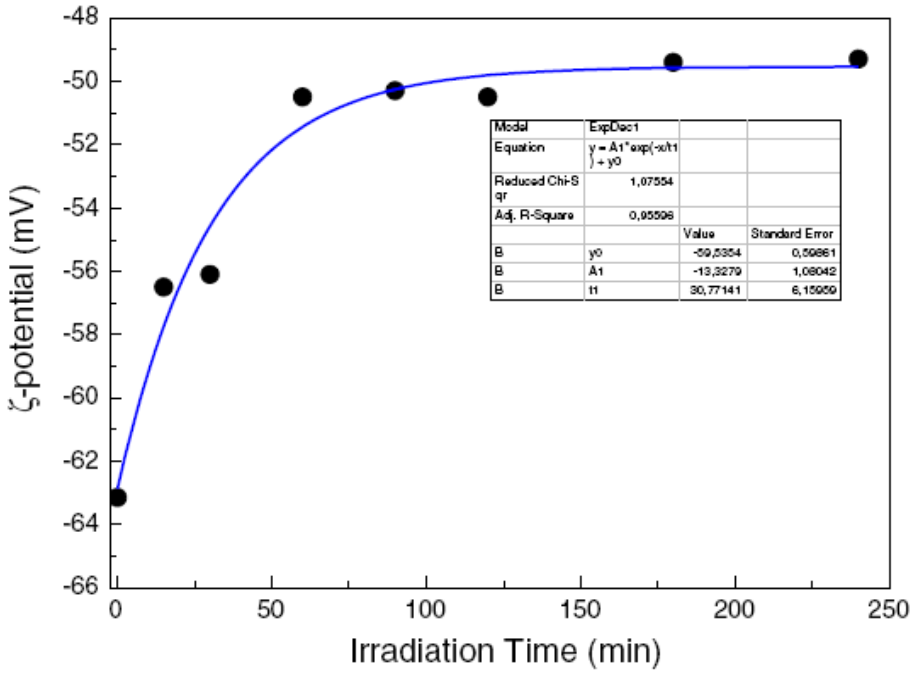

Fig.4-8 ζ-Potential evolution as a function of irradiation time.

4.3 Microscopy analysis

In addition to ζ-potential measurements, we have checked the hydrophobicity property of reduced graphene oxides observing the interaction of graphene with a hydrophilic surface (SiO_2). The corresponding AFM images (NT-MTD AFM operating in the tapping mode) are reported in Fig. 4-9. Fig. 4-9a clearly shows an extended deposition of GO partially scratched from the silicon surface, thus resulting in a GO-free SiO_2 (highlighted in the red circle). The overall roughness of the investigated regions (10 X 10 micron scale) results in a RMS of 1,3 nm. On the contrary, in the case of the deposition of rGO (Fig. 4-9b), a wrinkled layer, having a RMS of 6 nm is obtained. The different film morphology is related to the above-mentioned reduction of hydrophilic character of rGO. This tends to form large aggregates in aqueous solution. Accordingly, the reduced suspension drop casted on silicon will be less homogeneous (as indicated by the presence of large aggregates) and results in a thicker GO. Investigations are currently running to quantify this effect.

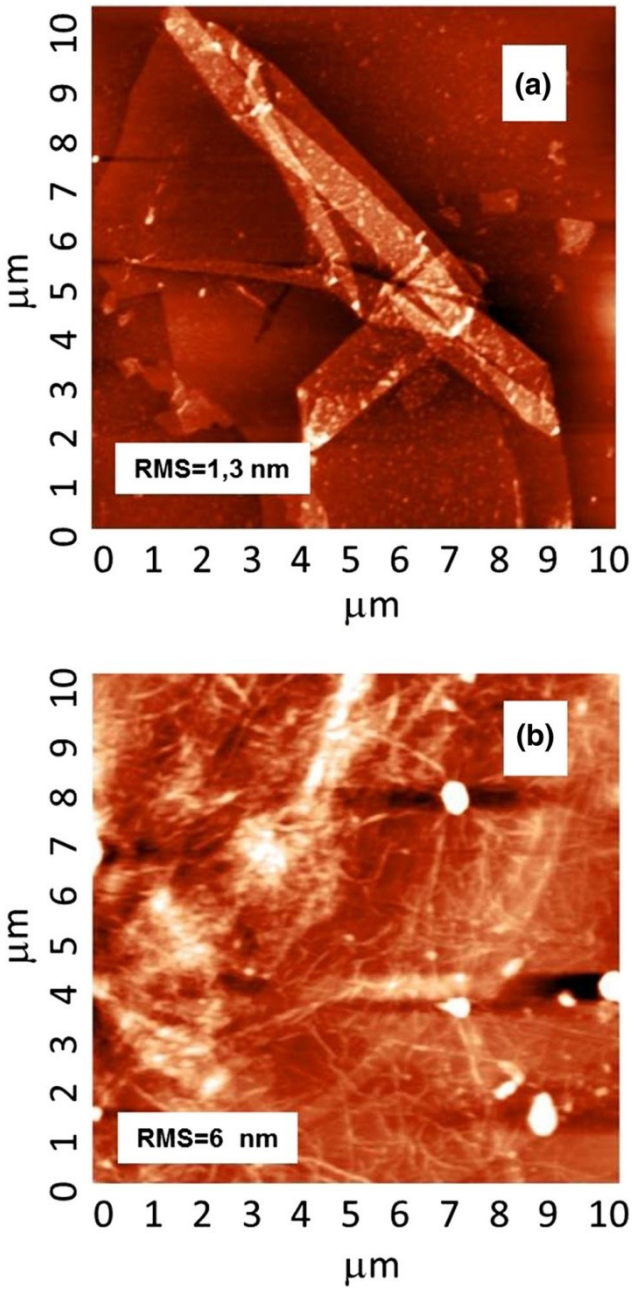

Fig. 4-9 AFM images of (a) GO and (b) rGO laser irradiated for 2 h, drop casted on SiO_2 surfaces.

Moreover, Scanning Electron Microscopy (SEM) has been very useful to observe the interesting and fascinating images of graphene oxide sheets and their folds (Fig. 4-10 and Fig. 4-11).

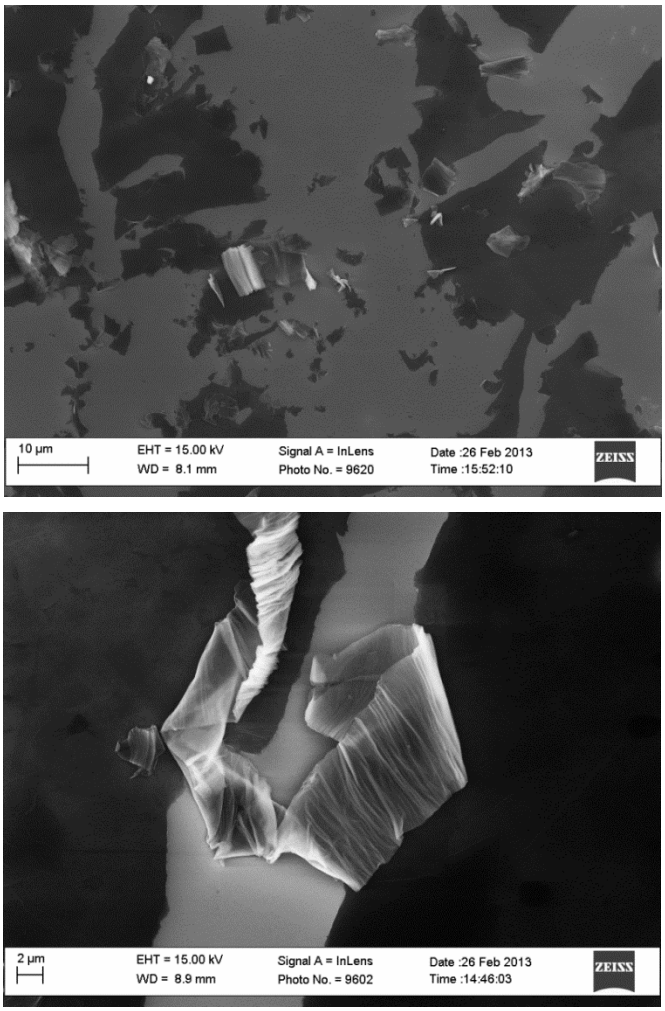

Fig. 4-10 Typical SEM images of GO sheets.

Transmission Electron Microscopy (TEM), performed by a Jeol JEM-ARM-200 cold FEG, has permitted to observe the series of overlapped layers in a GO sheet (from one to three layers, Fig. 4-11), with a characteristic “step-profile” (Fig. 4-12).

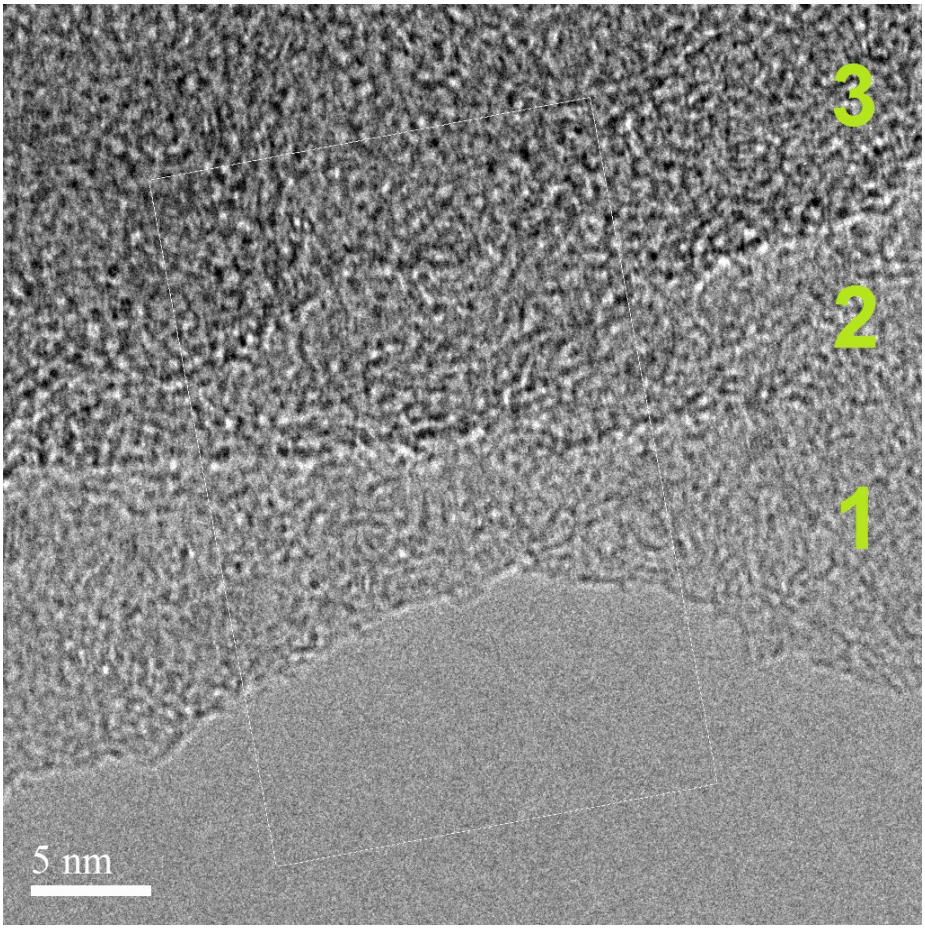

Fig. 4-11 TEM image of a GO sheets in which it is possible to observe the different layers.

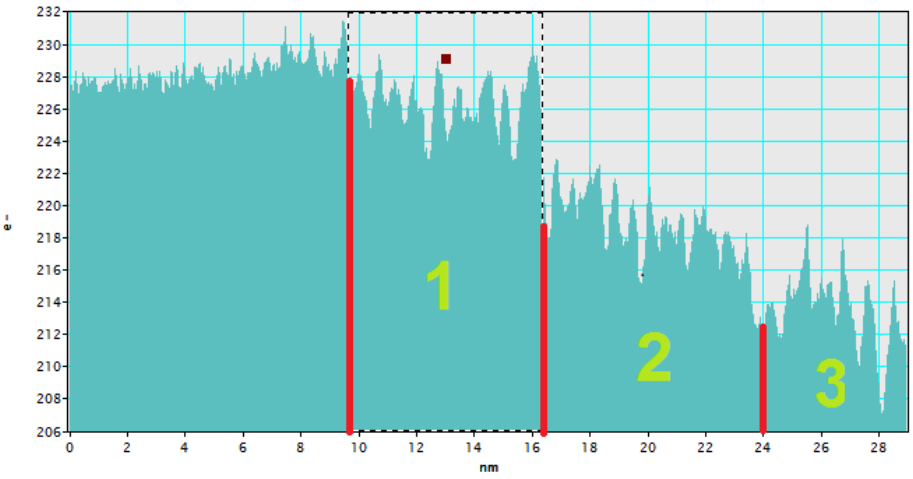

Fig. 4-12 Characteristic "step-profile" of a GO sheet.

4.4 Reduction-dependent resistivity measurements

The most common technique used for measuring the sheet resistance of materials is called Van der Pauw method. The method is based on a four point measurement and its advantage comes from the ability to measure precisely the resistivity of two-dimensional samples of an arbitrary shape. The approximation of two-dimensional samples can be achieved if the sample is much thinner than it is wide. In order to reduce the errors in calculations the sample needs to be symmetrical. For the measurement four contacts have to be placed on the sample as shown in Fig. 4-13.

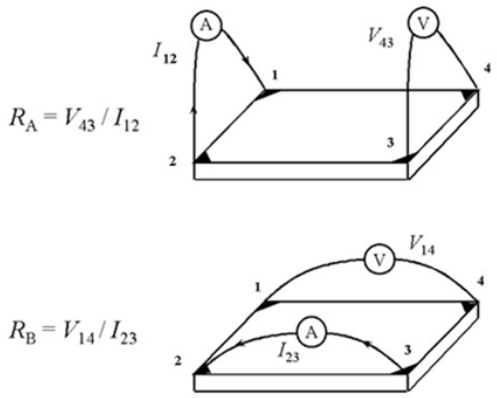

Fig. 4-13 Schematized representation of a "four contacts" Van der Pauw system.

The contacts are numbered counter-clockwise. The contacts are placed at the boundary of the sample and must be as small as possible. In the measurement the DC current is applied between the contacts 1 and 2 (I_{12}) while the voltage is measured between contact 3 and 4 (V_{34}). According to Ohm's law, from these two values the resistance, $R_{12,34}$ can be calculated as:

$$R_{12,34} = V_{34}/I_{12}$$

The sheet resistance, R_S, can be determined from the measurement of the resistance along the vertical ($R_{12,34}$) and

horizontal ($R_{23,41}$) edge of the sample according to the Van der Pauw equation

$$\exp(-\pi R_{12,34}/R_s) + \exp(-\pi R_{23,41}/R_s) = 1$$

In the case if $R_{12,34}=R_{23,41}=R$ the sheet resistance, R_S, can be easily calculated as:

$$R_s = R\pi/\ln 2$$

Electrical measurements of GO and rGO films were conducted by using Ecopia HMS-3000 Measurement System by means four-point Van der Pauw approach at ambient condition (Fig. 4-14).

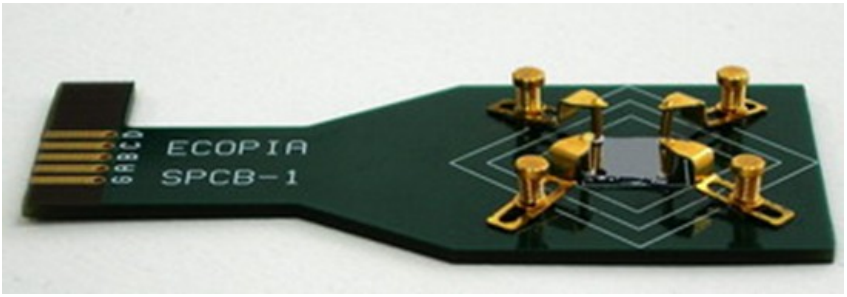

Fig. 4-14 Four-point Van der Pauw apparatus used for electrical measurements of GO and rGO films.

Four gold dots of about 0.1 mm were soldered at the four corners on the top surface of each film.

The GO and rGO films were built on a high-resistivity Si substrate by drop casting of the respective solutions (0,5 mg/mL). Therefore, a small amount of the current leaked through the bulk substrate, rather than passing through the graphene oxide. The resistivity of the samples was measured after mounting in a sample holder by passing current (I) through the sample and measuring the voltage (ΔV) between two points in a sample with known dimensions.

Figure 4-15 shows the sheet resistance of the GO and rGO thin films. As shown, first of all, we observe that if we increase the volume of GO solution drop-casted on the substrate from 700 to 1200 μL (variation of the amount of deposited material from ~0,3 to ~0,6 mg/cm^2), the sheet resistance decreases from $4*10^8$ to $3,5*10^7$ Ohm/Sq.

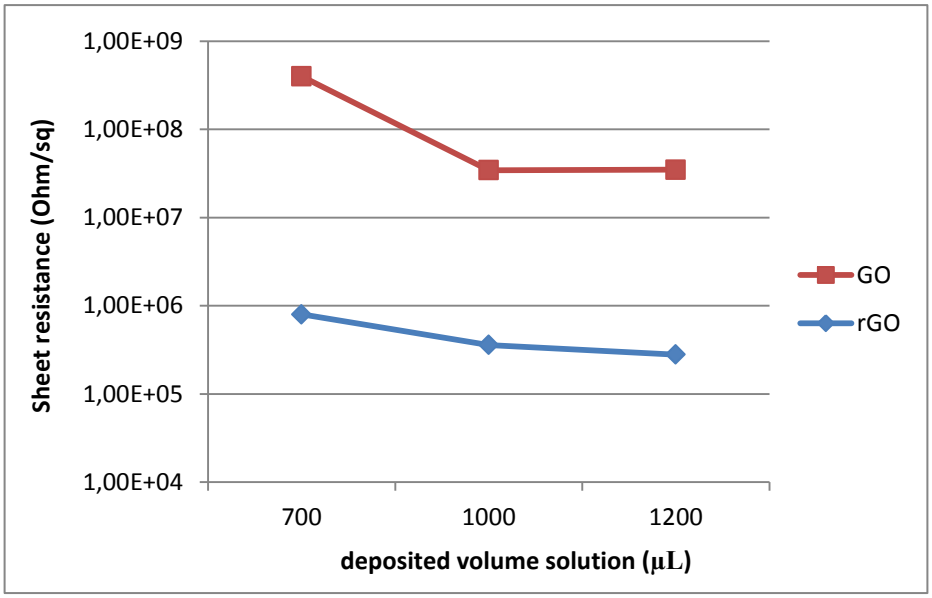

Fig. 4-14 Sheet resistance vs. deposited volume solution of GO and r-GO.

However, the most important information given by Fig. 4-14 is that, in case of films obtained by drop-casting of a GO solution irradiated for 2 h, the lowest sheet resistance is about $2{,}8*10^5$ Ohm/Sq, two order magnitude lower than GO. This result confirms the higher conductivity of reduced graphene oxides compared to GO, as we expected through the study of Tauc plots in the previous paragraphs.

Chapter 5 Prospective application features of reduced graphene oxides

5.1 Electronic packaging

Since the reduced graphene oxide has properties that make it very similar to pristine graphene, its potential applications are various: from energy storage to photocatalysis, from photovoltaic to sensing. Also in the electronics field and, in particular, with regard to power electronics, the products of reduction of GO can have a very important role, firstly thanks to its notable electrical and thermal properties. In this respect, recently, several studies (many of them are carried out in our research group) have unveiled the very good thermal conductivity of reduced graphene oxides that, under the suitable conditions, can catch up the typical values of pristine graphene.

Broad thermal properties and, also, remarkable mechanical characteristics could make rGOs very interesting potential nanomaterials for electronic packaging as a filler for new generation nanocomposites, usable for the realization of the protective assembling covers of chips, like in Fig. 5-1. Specifically, given their characteristics, these novel

graphene materials could be potentially applied for the production of plastic high power packages (~1–150 kW); they are for power electronics that may operate at voltages greater than 1000 V, currents greater than 1000 A, and moderate frequencies (<1 MHz). For packages of this kind of devices it is fundamental that the material in use is characterized by very high heat dissipation, in order to minimize the thermal effects on circuits and system performance.

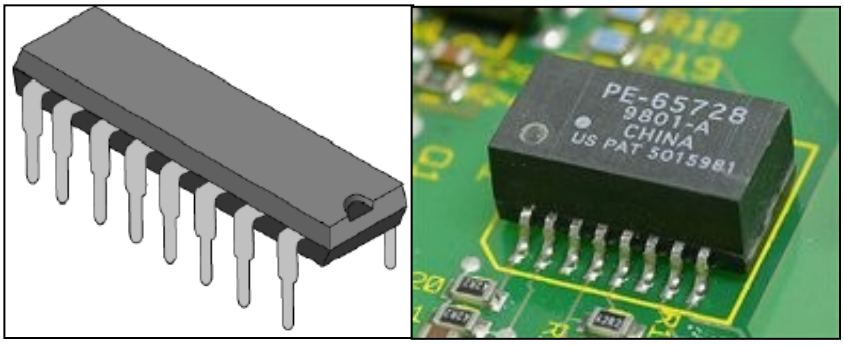

Fig. 5-1 Example of a plastic enclosure of a an integrated circuits chips.

Electronic packaging includes a broad range of technologies. For example, typically, the "encapsulation" (“potting”) is one of the most-used technique for the production of plastic electronic covers and it consists of immersing the part or assembly in a liquid resin like an epoxy or a polyurethane. Another very used method is the

"injection moulding", in which the liquid resin is infused through a mould in which the chip is situated (Fig. 5-2). During the above processes, reduced graphene oxides sheets could be employed like fillers for fitting polymer matrices, in order to improve the characteristics of the package.

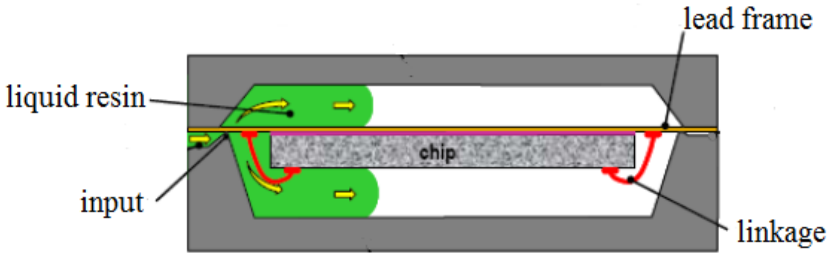

Fig. 5-2 Scheme of the production of an electronic package by injection moulding.

Although the concept of "high heat dissipation" for an electronic package became the crucial topic for industries and researchers, reduced graphene oxides can also offer two other properties that are just as important as the previous one: gas-barrier and moisture-barrier properties [132-134]. In fact, it is clear that an electronic system like a power device has to avoid any contact with oxygen and water, in order to guarantee a correct performance of the die, to avoid the formation of voids into adhesives and to eliminate any safety risks.

In this respect, recently, it was observed as graphene-derived layered materials like GO and rGO can be potential candidates of gas barrier membranes [135-137]. After all, many researchers have demonstrated as the incorporation of reduced graphene oxide fillers into a suitable polymer matrix implies the improving of gas-barrier (e. g. nitrogen and oxygen) and moisture-barrier properties of the resin [138].

In reality, the capacity to give rise a barrier effect for gas and moisture is not only a prerogative of layered graphene-derived materials like GO or rGO: it is a typical property of many plate-like nano-objects (e.g. clay). In fact, the dispersion of fitting plate-like nano-fillers in a polymer matrix allows to reduce gas and water vapor permeability because the tortuous diffusion path generated by them decreases the apparent gas diffusivity (Fig. 5-3) [138,139].

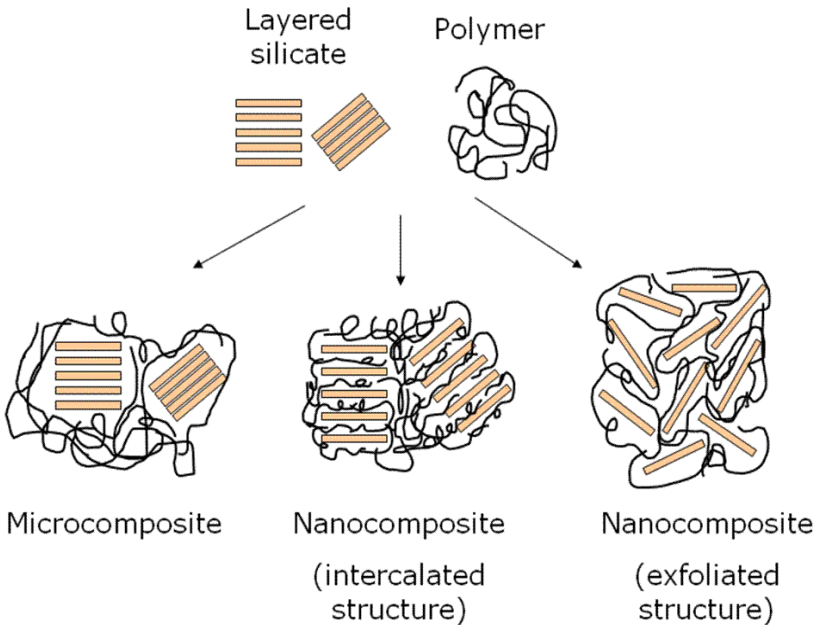

Fig. 5-3 Scheme of the typical formation of a composite plate-like filler (e.g. layered silicate)/polymer in which the "tortuosity" of the diffusion path is apparent.

The addition of flakes (e.g. layered silicates) to a resin film improves barrier properties thanks to the combination of two phenomena [139,140]:

- the decrease in area available for diffusion;
- the increase in the distance in which a gas or the water must spread to cross the film, thanks to the tortuous path around the impermeable flakes.

In this respect, the latest research has unveiled as graphene oxide and its reduced derivates have shape, size,

surface/volume ratio and, above all, interlayer spacing that are really appropriate for decreasing of oxygen and moisture diffusivity into a package.

Generally, the gas (e.g. oxygen) or water vapor permeability of a polymer film, in which GO or rGO are incorporated like fillers, can be analyzed using Fick's second law of diffusion, as follows:

$$D\nabla^2 c = \frac{\partial c}{\partial t} \tag{1}$$

in which ***c*** is the gas/vapor concentration in the film [141].

When **c** is close to zero at the bottom surface, the solution of Eq. (1) can be written as:

$$J = J_s \left(\frac{4d^2}{\pi Dt}\right)^{0.5} \sum_{n=0}^{\infty} exp\left[-\frac{d^2}{4Dt}(2n+1)^2\right] \tag{2}$$

where ***J*** is the gas/vapor molar flux at time ***t***, $\boldsymbol{J_s}$ is the gas/vapor flux at steady state, ***D*** is the diffusivity and ***d*** is the sample thickness.

At this juncture, it is fundamental to observe the correlation between the gas diffusivity ***D*** and the presence of GO or rGO sheets like fillers into the polymer film (Nielsen approximation) [142]:

$$D = D_0 \left(\frac{1 - \varphi_c}{1 + \frac{\alpha}{2} \varphi_c} \right) \quad (3)$$

where $\boldsymbol{D_0}$ is the diffusivity of polymer, $\boldsymbol{\varphi_c}$ is the volume fraction of the graphene material and $\boldsymbol{\alpha}$ is its aspect ratio.
This approximation describes the increase in the "tortuosity" of the gas/vapor diffusion path by relating it to the volume fraction and aspect ratio of graphene materials.

A valid example of in-depth research in this field has been carried out by Hye Min Kim and his coworkers [132,134].
To study the oxygen and water vapor barrier properties, they studied the behavior of 12 μm EVOH/GO and EVOH/RGO composite films (EVOH = ethylene vinyl alcohol) on a 23 μm PET substrate.
For example, regarding the oxygen diffusivity, the experimental data relating to EVOH/GO film, fitted through model calculations by Eq. (1), are shown in Fig. 5-4, in which the oxygen flux is plotted with respect to time.

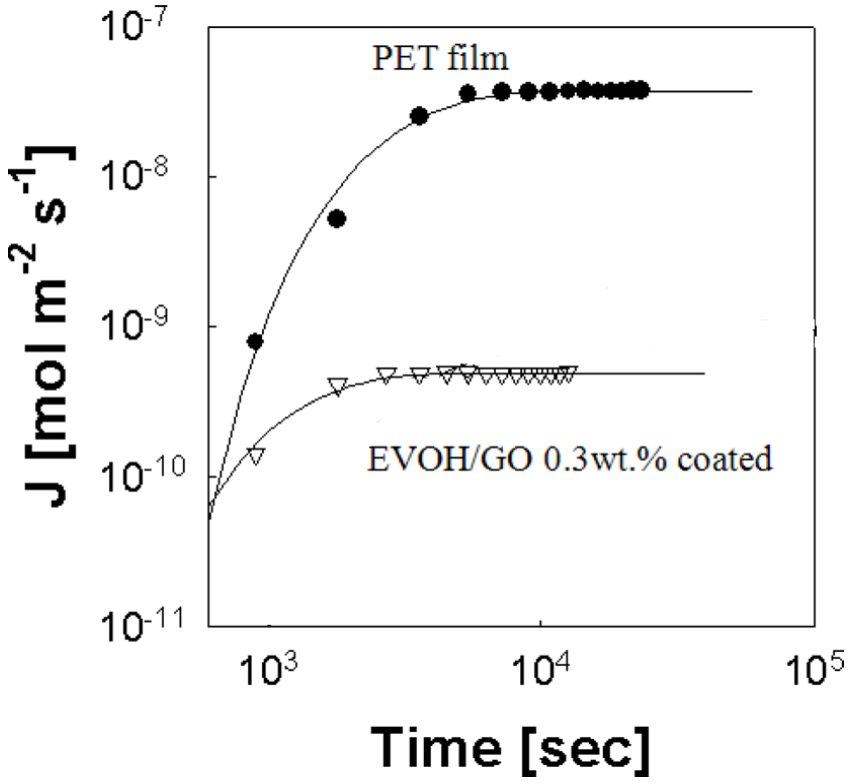

Fig. 5-4 Oxygen molar flux with respect to time of polyethylene terephthalate (PET) and ethylene vinyl alcohol (EVOH)/GO (adapted from ref. [134]).

It is so interesting to note as the oxygen molar flux of EVOH/GO (0.3 wt%) coated film is 123 times lower than a PET film.

The oxygen permeability $\boldsymbol{P}$ of these EVOH/GO and EVOH/rGO films, without PET substrate, can be determined by:

$$\frac{1}{P} = \frac{\chi_{GO}}{P_{GO}} + \frac{\chi_{GO}}{P_{PET}} \quad (4)$$

where $\boldsymbol{\chi_{GO}}$ is the ratio of the thickness of EVOH/GO to EVOH/GO/PET film. Thanks to this equation is possible to calculate that the oxygen permeability of EVOH/GO (0.3 wt%) film is 3.63×10^{-15} mol s^{-1} m^{-1} Pa^{-1} (63% of that of the pure EVOH film), while the oxygen permeability of EVOH/RGO (0.3 wt%) film is 4.48×10^{-15} mol s^{-1} m^{-1} Pa^{-1} (78% of that of the pure EVOH film). Consequently, the oxygen diffusivity of EVOH/GO (0.3 wt%) film is 1.4 times lower than that of the pure EVOH film.

Moreover, Kim and his coworkers have carried out very important studies regarding the moisture-barrier property of the above films (Fig. 5-5) [134].

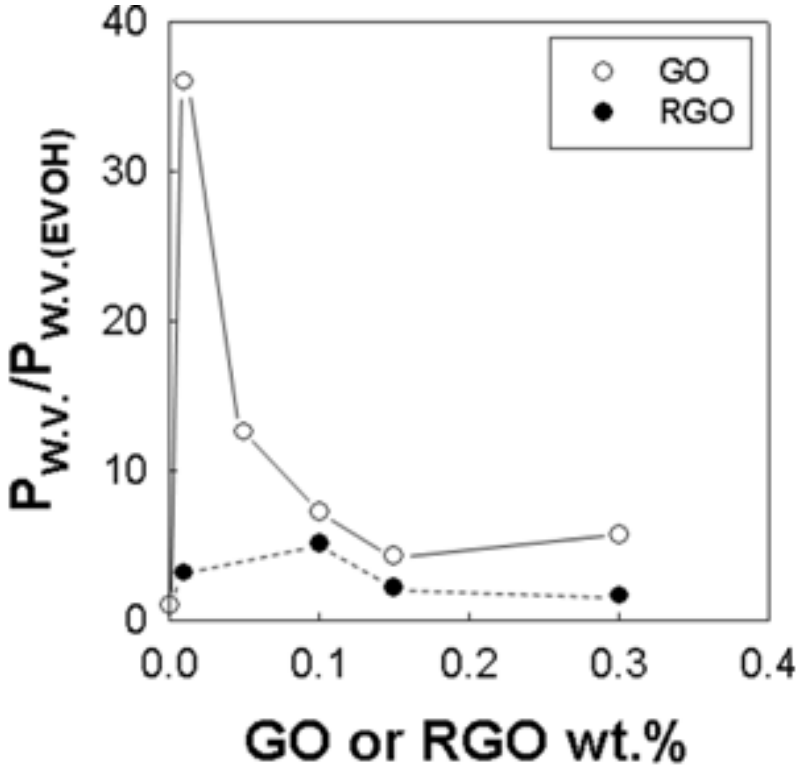

Fig. 5-5 Water vapor permeability of EVOH/GO and EVOH/RGO films, normalized by permeability of EVOH film (adapted from ref. [134]).

The water vapor permeability of rGO is lower than that of the GO. This may be due to the decrease of the interlayer spacing after the reduction process, since water molecules diffuse properly through the interlayer spacing [143]. This decrease of water vapor permeability in the RGO/EVOH film can also be caused by the decrease of the oxygen content, in favour of sp^2 hybridization, by the reduction.

Consequently, Kim's studies, primarily those relating to its moisture-barrier properties, together with the studies regarding its good thermal conductivity, permit to presume that rGO could be perfect like filler not only for food packages, but also for plastic enclosures of electronic devices and, in particular, for plastic high power packaging. Moreover, the possibility to easily tune the degree of reduction of rGO through an appropriate synthesis method like laser irradiation may permit to modulate and improve its characteristics in order to obtain nanomaterials with excellent electric, thermal and oxygen/moisture-barrier properties.

5.2 Water purification

5.2.1 Antimicrobial activity of reduced graphene oxides

- *Introductory aspects*

Significant recent attention has been drawn toward interactions between graphene derivatives and bioorganisms, since graphene-based nanomaterials have been found to show very interesting antibacterial

properties. For instance, antibacterial graphene-based papers can be conveniently fabricated with superior inhibition ability to bacteria growth, suggesting the promising environmental friendly applications of these low-cost and highly effective carbon nanomaterials [144].
Considered these literature data, it may be envisaged to take advantage of graphene properties in order to improve existing techniques of water purification. Although disinfection methods currently used in drinking water treatment can effectively control microbial pathogens, recent research have revealed a dilemma between the effective disinfection and the formation of harmful disinfection byproducts (DBPs). In fact, chemical disinfectants commonly used by the water industry such as free chlorine, chloramines and ozone can react with various constituents in natural water to form DBPs, many of which are carcinogens. Therefore, there is an urgent need to reevaluate conventional disinfection methods and to find novel innovative approaches that enhance the reliability and robustness of disinfection while avoiding the formation of byproducts. Recently, several natural and engineered nanomaterials have been investigated as possible alternative disinfection method. In particular, graphene oxide was recently proposed for the removal of pollutants from water [145]. Moreover,

graphene and GO were tested as antimicrobial agent: in fact, under some cases, the interaction between Escherichia Coli bacteria produces the disruption of the bacterial membrane [146].
During my PhD course, the antibacterial activity of GO and rGO at various reduction level was evaluated.

- *Experimental section*

The antimicrobial activity was tested on Escherichia Coli (ATCC25922), a well-known Gram-negative bacterium considered to be an indicator of faecal contamination in drinking water. Bacterial survival test was performed.
A single colony was inoculated in 50 ml of Luria-Bertani (LB) broth and grown overnight at 37°C by constant agitation at 180 rpm under aerobic conditions. The following day, the bacterial growth was measured by optical density at 600 nm.
Then, bacteria were diluted up to 106 CFU/ml and exposed either to GO or rGO at different concentrations in a volume of 300 µl. A control sample of untreated bacteria was run in parallel. Experiments were made in triplicates. Different final concentrations of GO or rGO were tested, ranging from 5 to 20 µg/ml. Aliquots were collected at one hour (1h) or three hours (3h)

respectively, conveniently diluted by serial dilutions 1:10 and plated in LB Agar Petri dishes. Plates were incubated overnight at 37°C and undergone to UV exposure for 1h. CFU were counted the following day.

Fig. 5-6 shows us the results of the bacterial survival test, in which it is possible to observe interesting trends.

First of all, we can note as, after 1h of UV treatment, the as-prepared GO do not present any antibacterial activity, while the reduced graphene oxides show an antimicrobial action that increases in relation to the irradiation time (then as function of the degree of reduction). Moreover, at the same time, it is apparent that, on equal terms of degree of reduction, the antibacterial activity of rGOs, increases with the concentration of solution. For instance, regarding GO solutions irradiated for 3h, we observe that 5, 10 and 20 μg/mL rGO solutions are respectively capable of killing 5%, 49% and 60% of the bacteria colony.

This experimental data suggest that, also for potential antibacterial applications, a synthesis method that permits to easily modulate the degree of reduction of rGOs is very important in order to improve the antimicrobial characteristics of the nanomaterial.

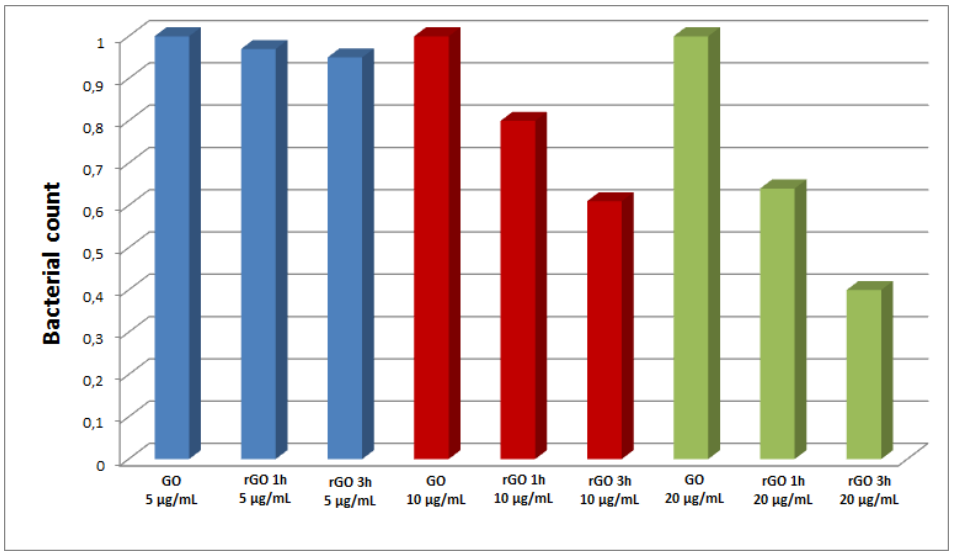

Fig. 5-6 Results of bacterial survival test.

5.2.2 Photocatalytic activity of GO/TiO_2 and rGO/TiO_2 nanosystems.

- *Introductory aspects*

Photocatalysis is a process in strong development, which finds application in every place in which the removal of pollutants is required (pharmaceutical laboratories, hospitals, food industries, automotive industries and so on). Photocatalytic method, alternative to the traditional processes for the disinfection of water and air, allows to inactive many dangerous microorganisms and it consists in

photochemical reactions using a catalyst which is active if it is irradiated by light of opportune wavelength. Typical catalysts are both II-VI compound semiconductors (CdS, ZnS) and semiconductor oxides (TiO_2, ZnO, ZrO_2, SnO_2).
Irradiation with light of proper wavelength produces electron excitation from a photocatalytic semiconductor valence band to the conduction band, with the consequent generation of an electron-hole pairs. Both electrons and holes can migrate to the surface of the semiconductor particles, where they react with water and dissolved oxygen to form various oxidizing species, as hydroxyl radicals known [147, 148].

- *Photocatalytic activity of titanium dioxide*

The titanium dioxide (TiO_2) is an oxide semiconductor with an high photocatalytic activity (activated by sunlight), due to its chemical and physical properties. Indeed, TiO_2 is the most effective catalyst, compared to other, in the degradation of many contaminants of interest.
TiO_2 is the most widely used semiconductor photocatalyst in water/wastewater treatment owing to its low toxicity, chemical stability, low cost, and abundance as raw material. It generates an electron/hole (e^-/h^+) pair upon absorbing a UV photon (Fig.5-7), which later migrate to the

surface, forming reactive oxygen species (ROS) or undergoing undesired recombination [149].

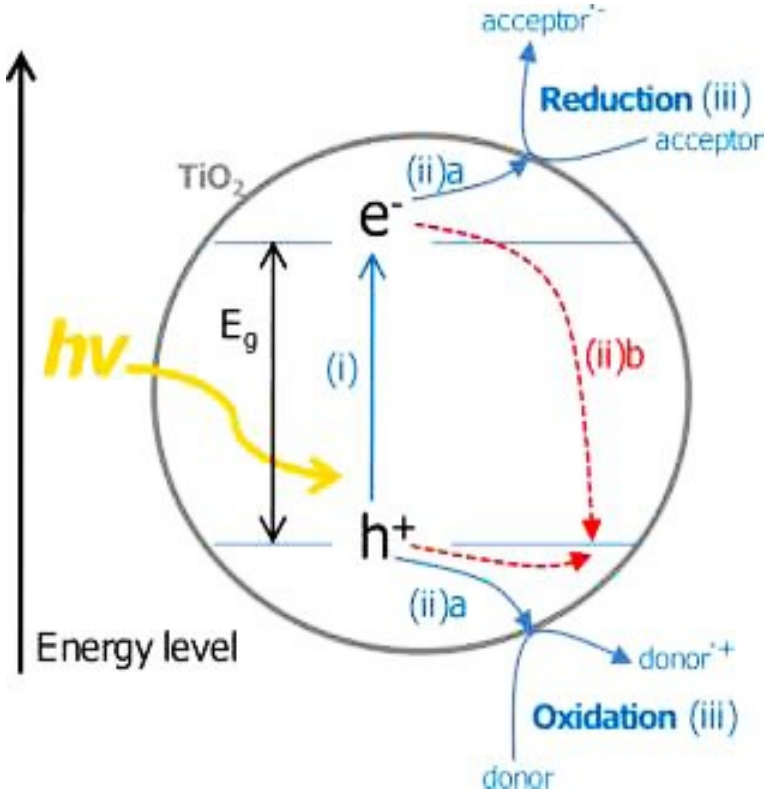

Fig. 5-7 Main processes in a photocatalytic semiconductor subsequent to the creation of an electron-hole pair induced by the incident radiation.

In case TiO_2 is in an aqueous solution, the gaps on the surface of the catalyst can directly oxidize water molecules or OH^- ions that are present in the solution. The oxygen can act as electron acceptor reacting with the electron created

according to the following mechanism. Finally, hydrogen peroxide (H_2O_2) generated is transformed into hydroxyl radicals that can cause the degradation of organic substances suspended in the aqueous solutions:

$$h^+ + H_2O \rightarrow OH + H^+$$
$$h^+ + OH^- \rightarrow OH$$
$$e^- + O_2 \rightarrow O_2^-$$
$$O_2^- + H^+ \rightarrow HO_2\cdot$$
$$HO_2\cdot + HO_2\cdot \rightarrow H_2O_2 + O_2$$

Unfortunately, most of the electron-hole pairs produced recombines too soon (about 10^{-9} s) compared with time that characterize the activation of the chemical reactions (10^{-8}-10^{-3} s) [150]. Therefore, only a small number of electrons (<1%) and holes don't recombine, leading to an enormous decrease in the efficiency of the process.

Recently, a field of big interest is improving the photocatalytic activity of TiO_2 mainly through two ways:

- avoiding the recombination of holes with electrons
- enlarging the light absorption of TiO_2 in the visible region.

In this respect, the combination of carbon nanostructures (carbon nanotubes, graphene oxide or, even better, reduced graphene oxide) with TiO_2 appears to be a good approach to

enhance the photocatalytic activity of titanium dioxide [151]. Specifically, these carbon nanosystems act as electron trap, reducing the recombination with holes and enhancing the answer to visible radiation.

- *Enhancing of photocatalytic activity of titanium dioxide through carbon nanostructures*

Carbon nanotubes (CNTs), with their characteristics and their high surface area, show the potential to contribute to three routes of increasing photocatalytic activity [151]:

- high-surface area and high quality active sites;
- retardation of electron–hole recombination;
- visible light catalysis by modification of bandgap and/or sensitization.

In Fig. 5-8, we can observe the different proposed mechanisms of synergistic enhancement in TiO_2-CNTs composites [151].

Also GO sheets are particularly effective in separating charges on TiO_2 because of their 2D profile. Additionally, the unpaired π electrons on GO can bond with surface Ti atoms of TiO_2 to form Ti–O–C bonding and extend the light absorption range of titania nanoparticles (Fig. 5-9) [152-155]. The GO-TiO_2 composites exhibited excellent photochemical responses under visible light (λ > 400 nm) irradiation.

The GO-TiO_2 hybrid materials have been used to harness photon energy for H_2 generation from water decomposition [156-158].

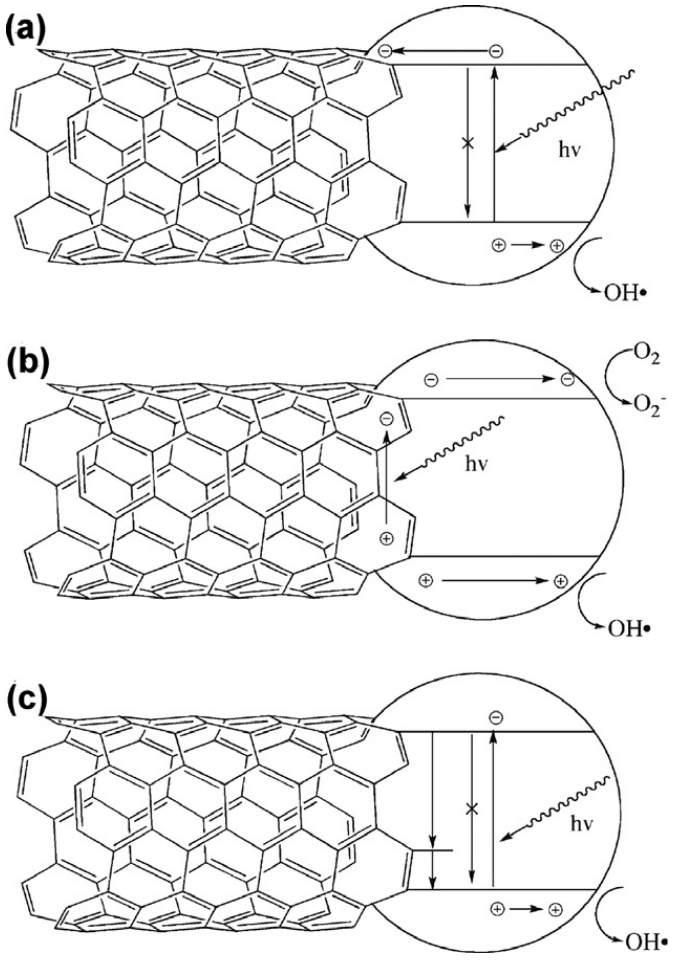

Fig. 5-8 Proposed mechanisms of synergistic enhancement in TiO_2–CNT composites. (a) CNTs inhibit recombination by acting as sinks for photogenerated electrons in TiO_2. (b)Photosensitizing mechanism based on electron–hole pair generation in the CNT [159]. (c)CNTs act as impurities through the Ti–O–C bonds [160,161]. Reproduced from ref. [160].

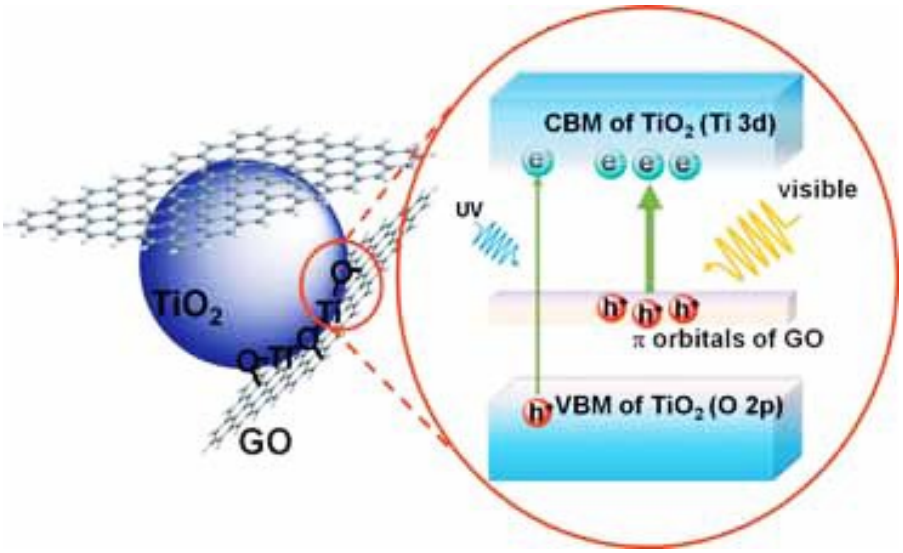

Fig. 5-9 Ti–O–C bonding formed through interaction between unpaired π electrons on GO with surface Ti atoms of TiO_2. This bonding narrows the band gap of TiO_2 and extends the light absorption range of TiO_2 (taken from ref. [152]).

- *Synthesis of GO/TiO_2 and rGO/TiO_2 nanosystems*

Considering what literature reports and considering the above information, during my PhD course GO/TiO_2 and rGO/TiO_2 were synthetized, in order to obtain novel nanomaterials with high photocatalytic activity.

These composites were prepared irradiating for 15 min (Nd:YAG, λ=532 nm, F=0,2 J/cm^2) a mix of a P25 solution (a mixture of anatase and rutile nanoparticles in an approximately 4:1 proportion, acquired from SigmaAldrich) with a GO or rGO solution, in a 9:1

proportion. The laser irradiation process aims to forward the interaction TiO_2/GO and TiO_2/rGO through the formation of Ti-O-C bonds.

Fig. 5-10 reports the extinction spectrum of a GO/P25 mix, irradiated for 15 min, in which it is possible to note the presence of a new component at ~280 nm (probable synonymous of formation of a new specie). This new signal is neatly observable in the extinction spectrum of rGO (2 h)/P25 mix, irradiated for 15 min (Fig. 5-11).

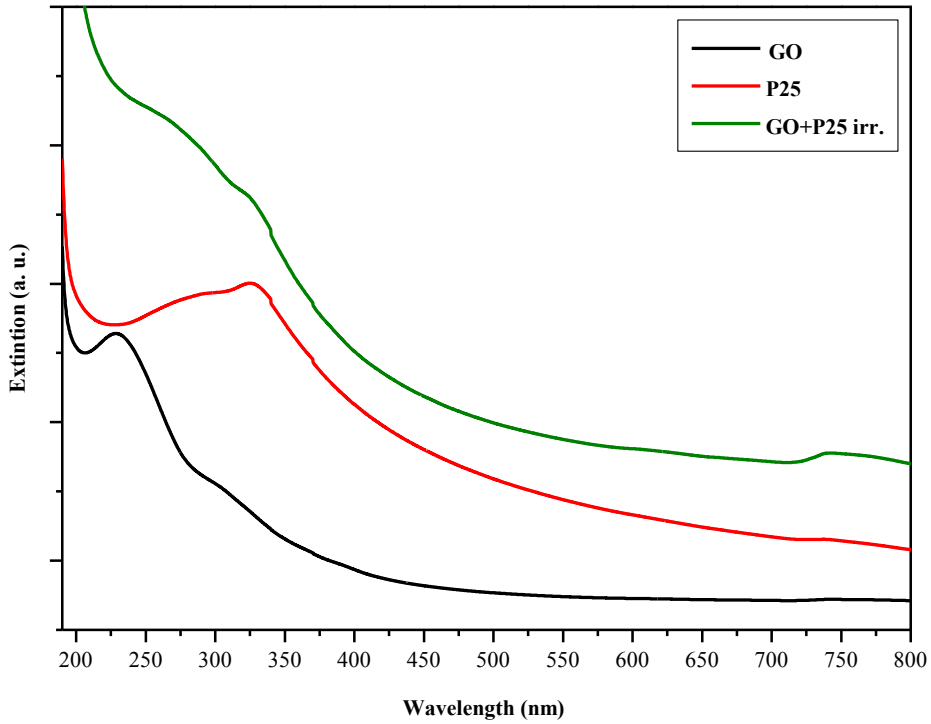

Fig. 5-10 Extinction spectrum of a laser irradiated GO/P25 mix.

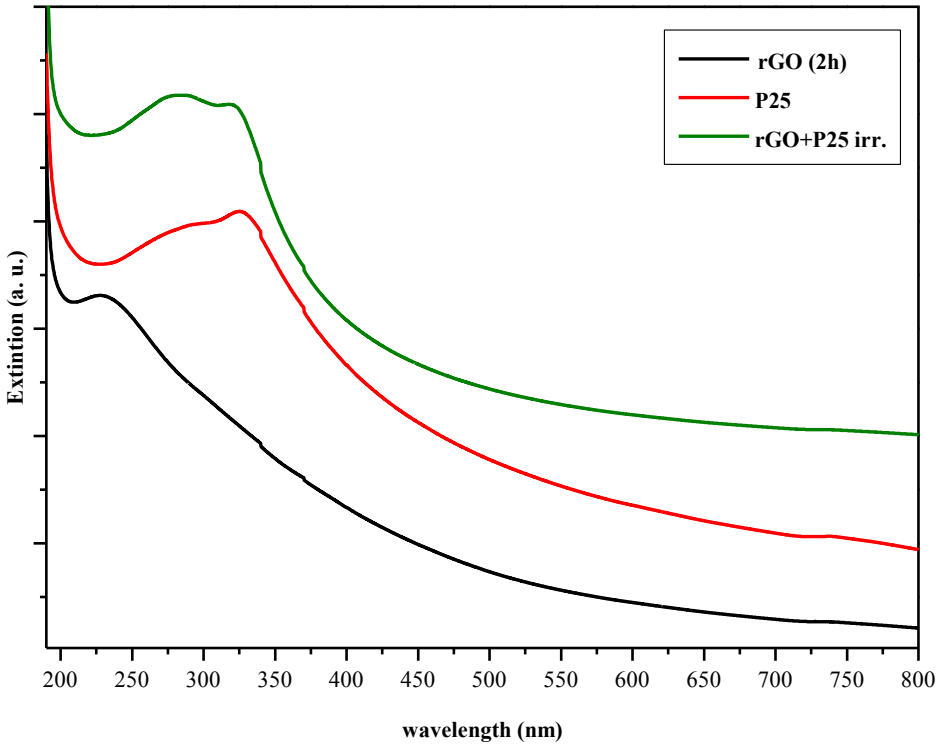

Fig. 5-11 Extinction spectrum of a laser irradiated rGO (2h)/P25 mix.

Another technique of characterization that may prove the formation of these nanosystems is Raman analysis; in fact, for instance, it is possible to observe significant Raman shifts of D and G peaks of GO or rGO as consequence of the GO/TiO_2 or rGO/TiO_2 interaction (Fig. 5-12).

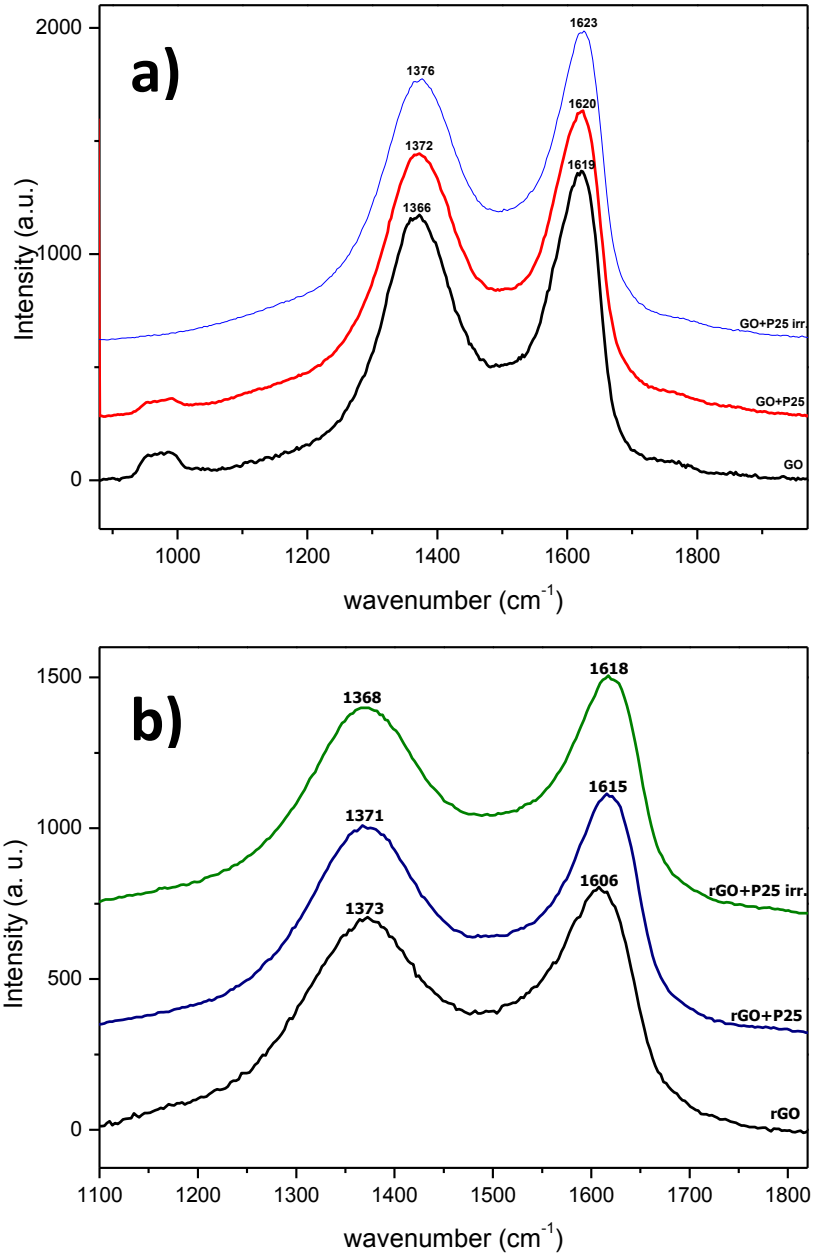

Fig. 5-12 Raman spectra of a) GO/P25 and b) rGO/P25 mix, before and after laser irradiation.

In addition, the images obtained by Scanning Electron Microscopy (SEM) tend to confirm the presence of an hard interaction between TiO_2 nanoparticles and GO or rGO sheets after the laser treatment (possible generation of Ti-O-C bonds); in fact, we can note as the titania nanoparticles are surprisingly present only onto the surface of graphene sheets, following their edges, while TiO_2 is totally absent outside them (Fig. 5-13 and 5-14).

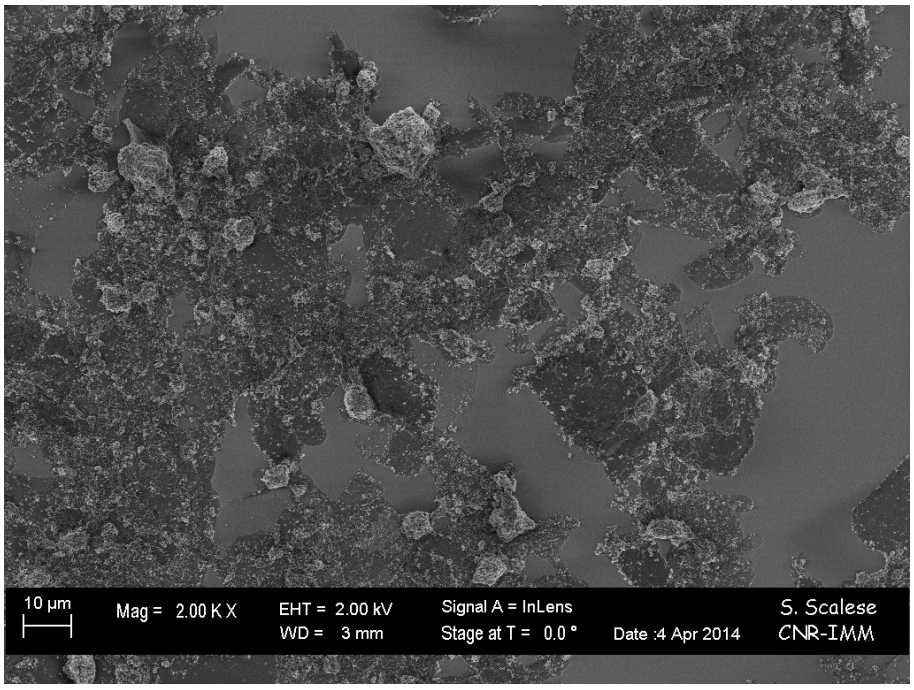

Fig. 5-13 SEM image of a GO/P25 mix, irradiated for 15 min.

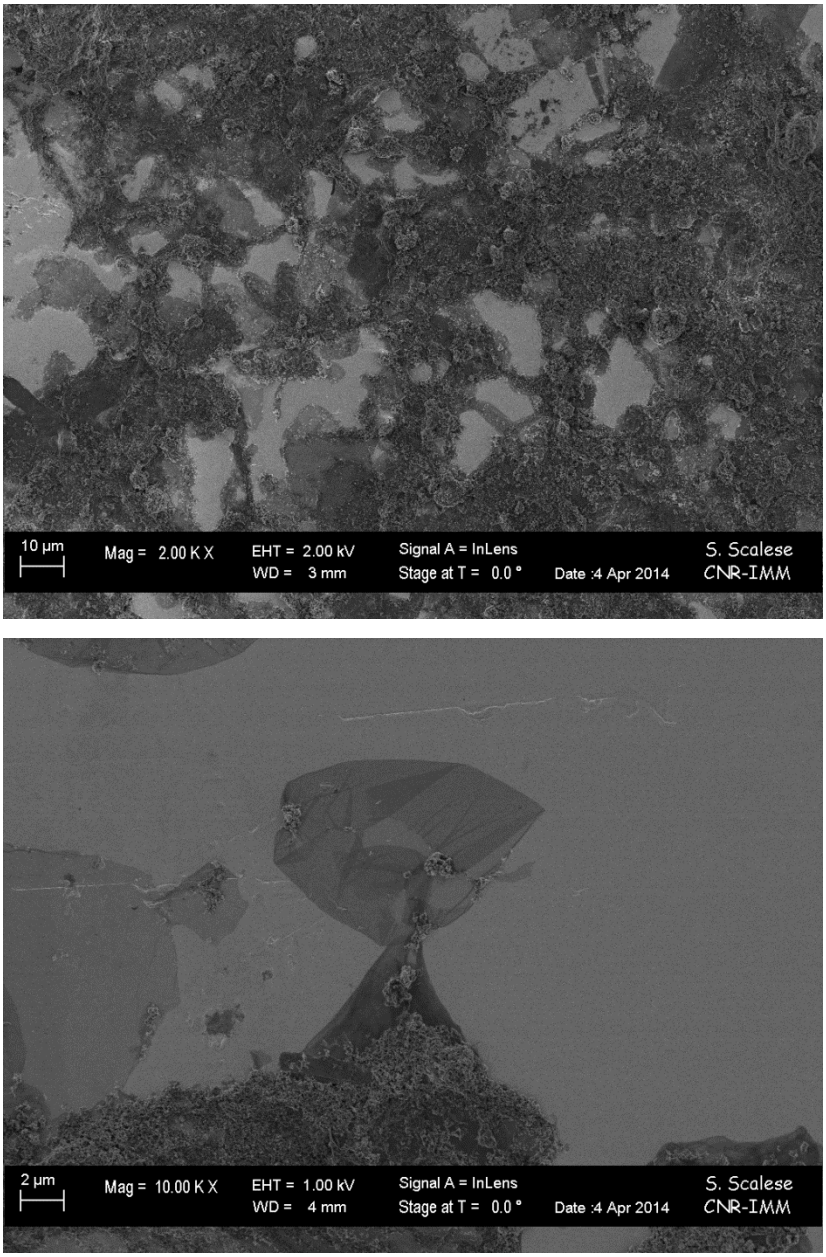

Fig. 5-14 SEM images of a rGO(4h)/P25 mix, irradiated for 15 min.

- *Photocatalytic properties of GO/TiO_2 and rGO/TiO_2 nanosystems.*

The photocatalytic characterization of GO/TiO_2 and rGO/TiO_2 has been conducted in methylene blue, an azo dye with a positive charge (Fig. 5-15), used as 10^{-5} M solution. The aim is to investigate the role of GO and rGOs in supporting and enhancing the photocatalytic activity of titania, measuring the photocatalytic degradation of MB under UV-Vis light irradiation (350-550 nm) for 1 h.

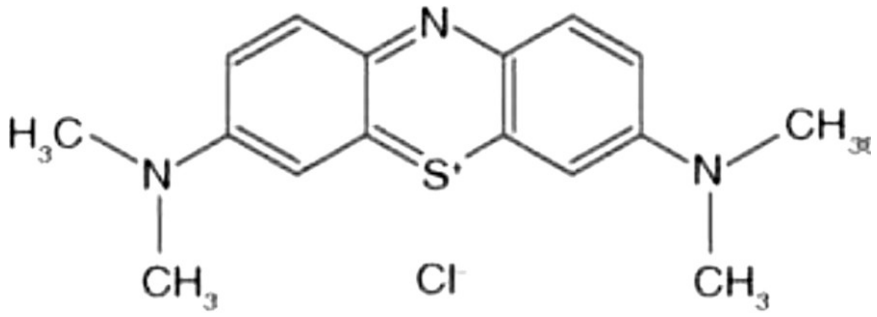

Fig. 5-15 Methylene Blue structure.

Fig. 5-16 reports the remaining concentration (C/C_0 %) of MB in solution, following the interaction between MB and GO(rGOs)/TiO_2 nanosystems (P25 20 mg/L, GO and rGO 10% relatively to P25), in darkness and under UVA-blue light irradiation (350-550 nm).

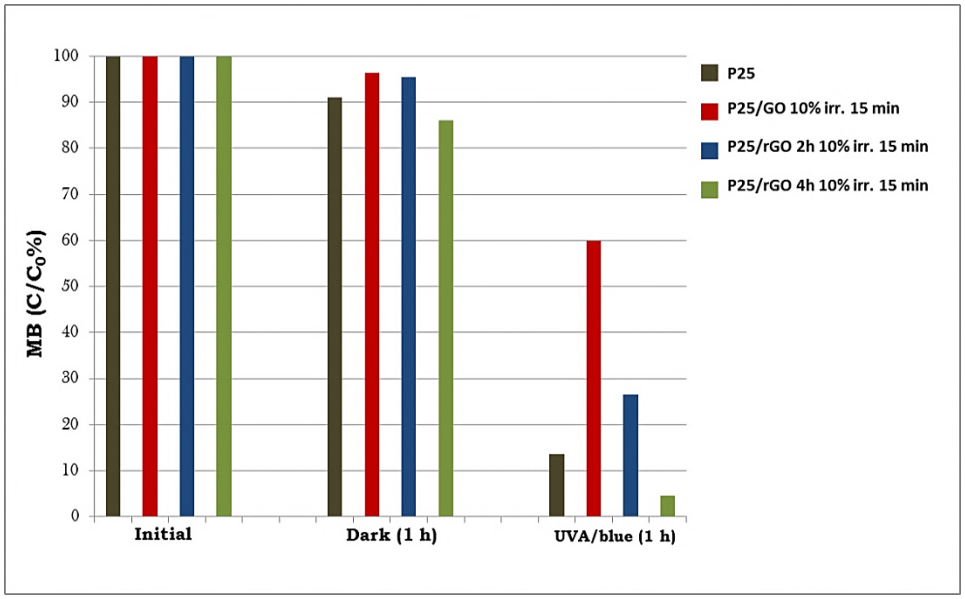

Fig. 5-16 Photocatalytic activity of P25/GO and P25/rGOs solutions, through measurements of photocatalytic degradation of Methylene Blue (MB).

Fig. 5-16 already shows a light initial decrease of residual concentration of MB in dark conditions; however, this first diminution of MB percentage in all the solutions is only due to absorption phenomena that characterize both P25 and GO or rGOs (phenomena of photocatalytic degradation are absent in these conditions). Instead, the most interesting information is shown for solutions undergone to UVA/blue irradiation exposure. In fact, it is possible to note a very surprising trend: the residual concentration of MB, following the photocatalytic degradation processes, decreases with the increase of the reduction degree of the

graphene component. Specifically, we observe that the residual MB amounts to 59.8% for the irradiated P25/GO solution, 26.5% for the irradiated P25/rGO (2h) solution and only 4.5% for the irradiated P25/rGO (4h); therefore, this last solution is capable to degrade more than 96% of the MB concentration, showing a photocatalytic activity that is superior to P25 that degrades only 86% of MB in solution, on equal conditions.

The different photocatalytic activity of these nanosystems from varying the degree of reduction of rGOs can be easily connected with the modulation of energy gap of the nanosystem, which determines the excitation of TiO_2 and, consequently, the formation of electron/hole pairs (e^-/h^+) that in turn react with the adsorbed oxidants/reducers (e.g. O_2/OH^-) to produce active oxygen radicals; these radicals will cause degradation of the model dye methylene blue.

Conclusions

During my PhD course in Science and Technology of Materials, my research aim was the synthesis and characterization of reduced graphene oxides solutions by a novel, simple and promising approach that consists in the progressive pulsed laser irradiation of as-prepared GO colloids, obtained by a modified Hummers method. In this way, it may be possible to avoid the use of any toxic reducing agent, like hydrazine, and any other deoxygenating processes that are time consuming and complicated. In other words, this facile method has essentially the advantages to being greener than other approaches and to involving the graphene oxide sheets directly in solution, with negligible overall temperature increase.

Concerning the laser reduction mechanism, our hypothesis is that GO sheets undergo to a mechanism similar to a solvothermal reduction; in particular, we can assume that during the laser irradiation of a GO solution, there is a local increase of the temperature and pressure, which led to the reduction of the sheets.

The use of a 532 nm laser irradiation wavelength, slightly diverted from the typical absorption wavelength of graphene

oxide, has permitted to gradually and finely tune the degree of reduction and, consequently, the graphene component of rGO varying the exposure time to the pulsed laser radiation. Another fundamental goal of my PhD project was the achieving of opportune scientific supports in order to demonstrate that a so simple way of manipulation of the degree of reduction and, consequently, of the properties of reduced graphene oxides permits to earmark their use to several potential applications in many fields. For instance, it has been possible to demonstrate how reduced graphene oxide, through its tunable features like, first of all, bandgap, may acquire properties that make it fit for electronic packaging field, as a filler for new generation nanocomposites, usable for the realization of the protective assembling covers of chips, like plastic high power packages (considering its well-known thermal, electrical and gas/moisture barrier properties). Furthermore, studies and research during my PhD course have permitted to understand how laser-induced reduction processes of graphene oxide and the consequent capacity of tuning its degree of reduction implies the synthesis of nanomaterials that are characterized by a surprising antimicrobial property (tested on *Escherichia Coli* bacteria through a series of reliable bacterial survival tests). Moreover, several methylene blue tests have showed how rGOs/TiO_2(P25)

nanosystems, obtained by a brief irradiation process towards a mix of laser-reduced GO and P25 solutions, exhibit a notable photocatalytic activity, which is closely related to the degree of reduction of the graphene component. Then, such a set of characteristics makes rGO a promising material for water treatment and purification, avoiding, in this way, the formation of harmful disinfection byproducts (DBPs), many of which are carcinogens.

Bibliography

1. **R.B. Heimann, S.E. Evsyukov, Y. Koga,** *Carbon*, Vol. 35, 10-11, pp. 1654-1658 (1997).
2. *The Allotropy of the* Elements, **W.E. Addison**, Oldbourne Press, London (1964).
3. *Polymorphism and Polytypism in Crystals*, **A.R. Verma and P. Krishna**, Wiley, New York (1966).
4. *Proc. 5th London Int. Carbon Graphite Conf.*, Sept. 18-22, 1978, Vol. 3, p. 103 (Publ. 1979).
5. **H.W. Kroto, J.R. Heath, S.C. O'Brien, R.F. Curl, R.E. Smalley,** *Nature*, Vol. 318, pp. 162-163 (1985).
6. *The Physics and Chemistry of Solids*, **S. Elliott**, Wiley, Chichester (1998).
7. **S. Iijima**, *Nature*, Vol. 354, pp. 56-58 (1991).
8. **A. Saito et al.**, *Appl. Phys. Lett.*, Vol. 60, 2204 (1992).
9. **H. Kuzmany, A. Kukovecz, F. Simona, M. Holzweber, C. Kramberger, T. Pichler**, *Synthetic Metals*, Vol. 141, pp. 113-122 (2004).
10. **N. Hamada, S. Sawada, A. Oshiyama**, *Phys. Rev. Lett.*, Vol. 68, n. 10, pp. 1579-1581 (1992).
11. **C.T. White, J. W. Mintmire**, *Nature*, Vol. 394, p. 29 (1998).

12. **S.K. Shin, J.K. Song, S.M. Park**, *Appl. Surf. Sc.*, Vol. 257, 12, pp. 5156-5158 (2011).
13. **P. Thaddeus, M.C. McCarthy**, *Spectrochim. Acta A*, Vol. 57, pp. 754-774 (2001).
14. **L. Ravagnan, F. Siviero, C. Lenardi, P. Piseri, E. Barborini, P. Milani**, *Phys. Rev. Lett.*, Vol. 89, 285506 (2002).
15. **S. Yang, M. Kertesz**, *J. Phys. Chem. A*, Vol. 110, pp. 9771-9774 (2006).
16. **R.B. Heiman, S.E. Evsyukov, L. Kavan,** *Carbyne and Carbynoid Structures*, Kluwer Academic Publishers, p. 444 (1999).
17. **A.K. Geim, K.S. Novoselov, S.V. Morozov, D. Jiang, Y. Zhang, S.V. Dubonos, I.V. Grigorieva, A.A. Firsov**, *Science*, Vol. 306, p. 666 (2004).
18. **E. McCann, M. Koshino,** *Rep. Prog. Phys.*, **76** (2013).
19. **A. Maffucci, G. Miano**, *Appl. Sci.*, Vol. 4(2), pp. 305-317 (2014).
20. **Castro Neto et al.**, *Rev. Mod. Phys.*, 81, No. 1 (2009).
21. **W. Chol, J-W. Lee**, *Graphene: Synthesis and applications*, CRC Press, Taylor & Francis Group (2012). ISBN: 978-1-4398-6187-5.
22. **X. Michalet, F.F. Pinaud, L.A. Bentolila, J.M. Tsay, S. Doose, J.J. Li, G. Sundaresan, A.M. Wu, S.S.**

Gambhir, S. Weiss, *Science*, Vol. 307, pp.538-544 (2005).

23. **S. Bae, H. Kim, Y. Lee, X. Xu, J.-S. Park, Y. Zheng, J. Balakrishnan, T. Lei, H.R. Kim, Y. Song, Y.-J. Kim, K.S. Kim, B. Ozyilmaz, J.-H. Ahn, B.H. Hong, S. Iijima**, *Nanotech.*, Vol. 5, pp. 574-578 (2010).
24. **X. Wang, L. Zhi, K. Müllen**, *Nano Lett.*, Vol. 8, pp. 323-327 (2008).
25. **M.S. Dresselhaus**, *G. Adv. Phys.*, Vol. 51, pp. 1-186 (2002).
26. **Y. Hernandez et al.**, *Nature Nanotech.*, Vol. 3, pp. 563-568 (2008).
27. **V.C. Tung et al.**, *Nature Technology*, Vol. 4, pp. 25-29 (2009).
28. **A.G. Cano-Màrquez et al.**, *Nano Lett.*, Vol. 4, p. 4 (2009).
29. **K.S. Subrahmanyam et al.**, *J. Phys. Chem. C*, Vol. 113, p. 11 (2009).
30. **H.O. Jeschke, M.E. Garcia, K.H. Bennemann**, *Phys. Rev. Lett.*, Vol. 87, pp. 15003-4 (2001).
31. **K. Hou, R.A. Outlaw, S. Wang, M. Zhu, R.A. Quinlan, D.M. Manos, M.E. Kordesch, U. Arp, B.C. Halloway**, *App. Phys. Lett.*, Vol. 92, p. 133112 (2008).
32. **S. Watcharotone, R.S. Ruoff, F.H. Read**, *Physics Procedia*, Vol. 1, pp. 71-75 (2008).

33. **S. P. Koenig, L. Wang, J. Pellegrino, J.S. Bunch**, *Nat. Nanotech.*, Vol. 7, pp. 728-732 (2012).
34. **D. Jiang, V.R. Cooper, and S. Dai**, *Nano Lett.*, Vol. 9, pp. 4019-4024 (2009).
35. **J. Zhu, D. Yang, X. Rui, D. Sim, H. Yu, H. E. Hoster, P.M. Ajayan, Q. Yan**, *Small,* http://dx.doi.org/10.1002/smll.201300755 (2013).
36. **S. Zhuo, M. Shao, and S.T. Lee**, *ACS Nano*, Vol. 6, pp. 1059-1064 (2012).
37. **B. Brodie**, *Phil. Trans.*, Vol. 149, p. 249 (1859).
38. **G. Eda, G. Fanchini, M. Chhowalla**, *Nat. Nanotechnology*, Vol. 3, p. 270 (2008).
39. **S. Park, R.S. Ruoff**, *Nat. Nanotechnol.*, Vol. 4, p. 217 (2009).
40. **M.J. Allen, V.O. Tung, R.B. Kaner**, *Chem. Rev.*, Vol. 110, p. 132 (2010).
41. **D.R. Dreyer, S. Park, C.W. Bielawski, R.S. Ruoff,** *Chem. Soc. Rev.*, Vol. 39, p. 228 (2010).
42. **A. Lerf, H. He, M. Forster, J. Klinowski**, *J. Phys. Chem. B*, Vol. 102, p. 4477 (1998).
43. **K. Erickson, R. Erni, Z. Lee, N. Alem, W. Gannett, A. Zettl**, *Adv. Mater.*, Vol. 22, p. 4467 (2010).
44. **C. Gòmez-Navarro, R. Weitz, A.M. Bittner, M. Scolari, A. Mews, M. Burghard, K. Kern**, *Nano Lett.*, Vol. 7, p. 3499 (2007).

45. **S. Saxena, T.A. Tyson, S. Shukla, E. Negusse, H. Chen, J. Bai**, *Appl. Phys. Lett.*, Vol. 99, p. 13104 (2011).
46. **C. E. Hamilton**, PhD Thesis, Rice University, Houston, Texas (2009).
47. **Y. Si, E.T. Samulski**, *Nano Lett.,* Vol. 8, p. 1679 (2008).
48. **J.R. Lomeda, C.D. Doyle, D.V. Kosynkin, W.-F. Hwang, J.M. Tour**, *J. Am. Chem. Soc.*, Vol. 130, p. 16201 (2008).
49. **F. Cataldo, G. Compagnini, G. Patanè, O. Ursini, G. Angelini, P.R. Ribic, G. Margaritondo, A. Cricenti, G. Palleschi, F. Valentini**, *Carbon*, Vol. 48, p. 2596 (2010).
50. **C. Gong, M. Acik, R.M. Abolfath, Y. Chabal, K. Cho**, *J. Phys. Chem. C*, Vol. 116, p. 9969 (2012).
51. **G. Williams, B. Seger, P.V. Kamat**, *ACS Nano*, Vol. 2, p. 1487 (2008).
52. **O. Akhavan, E. Ghaderi**, *J. Phys. Chem. C*, Vol. 113, p. 20214 (2009).
53. **L.J. Cote, R. Cruz-Silva, J. Huang**, *J. Am. Chem. Soc.*, Vol. 131, p. 11027 (2009).
54. **Y. Zhou, Q. Bao, B. Varghese, L. Ai Ling Tang, C.K. Tan, C.-H. Sow, K.P. Loh**, *Adv. Mater.*, Vol. 22, p. 67 (2009).
55. **L. Staudenmaier**, *Ibid.*, Vol. 32, 2824 (1899).

56. **A. Lachman**, *J. Am. Chem. Soc.*, Vol. 23 (12), pp. 902–923 (1901).
57. **W.S. Hummers, R.E. Offeman**, *J. Am. Chem. Soc.*, Vol. 80, p. 1339 (1958).
58. **L.J. Cote, F. Kim, and J. Huang**, *J. Am. Chem. Soc.*, Vol. 131, n. 3, p. 1045 (2009).
59. **U. Hofmann, R. Holst**, *Ber. Dtsch. Chem. Ges. B*, Vol. 72, pp. 754-771 (1939).
60. **G. Ruess**, *Monatsh. Chem.*, Vol. 76, pp. 381-417 (1946).
61. **M. Mermoux, Y. Chabre, A. Rousseau**, *Carbon*, Vol. 29, pp. 469-474 (1991).
62. **W. Scholz, H.P. Boehm**, *Z. Anorg. Allg. Chem.*, Vol. 369, pp. 327-340 (1969).
63. **T. Nakajima, A. Mabuchi, R. Hagiwara**, *Carbon*, Vol. 26, pp. 357-361 (1988).
64. **H. He, T. Riedl, A. Lerf, J. Klinowski**, *J. Phys. Chem.* , Vol. 100, pp. 19954-19958 (1996).
65. **A. Lerf, H. He, M. Forster, J. Klinowski**, *J. Phys. Chem. B*, Vol. 102, pp. 4477-4482 (1998).
66. **H. He, J. Klinowski, M. Forster, A. Lerf**, *Chem. Phys. Lett.*, Vol. 287, pp. 53-56 (1998).
67. **A. Buchsteiner, A. Lerf, J. Pieper**, *J. Phys. Chem. B*, Vol. 110, pp. 22328-22338 (2006).

68. **A. Lerf, A. Buchsteiner, J. Pieper, S. Schöttl, I. Dèkàny, T. Szabo, H.P. Boehm,** *J. Phys. Chem. Solids,* Vol. 67, pp. 1106-1110 (2006).
69. **T. Szabo, O. Berkesi and I. Dekany**, *Carbon*, Vol. 43, pp. 3186-3189 (2005).
70. **T. Szabo, O. Berkesi, P. Forgo, K. Josepovits, Y. Sanakis, D. Petridis, I. Dèkàny**, *Chem. Mater.*, Vol. 18, pp. 2740-2749 (2006).
71. **T. Szabo, E. Tombacz, E. Illes, I. Dèkàny**, *Carbon*, Vol. 44, pp. 537-545 (2006).
72. **V.C. Tung, et al.**, Nat. Nanotech., Vol. 4, pp. 25-29 (2009).
73. **S. Stankovich, D.A. Dikin, R.D. Piner, K.A. Kohlhaas, A. Kleinhammes, Y. Jia, Y. Wu, S.T. Nguyen and R.S. Ruoff**, *Carbon*, Vol. 45, pp. 1558–1565 (2007).
74. **R. Neidlein, T.V. Dao, A. Gieren, M. Kokkinidis, R. Wilckens, H.P. Geserich.**, *I. Chem Ber*, Vol. 115 (8), pp. 2898-2904 (1982).
75. **P.S. Wharton, D.H. Bohlen**, *J. Org. Chem.*, Vol. 26, p. 3615 (1961).
76. **Z. Zalan, L. Lazar, F. Fueloep**, *Curr. Org. Chem.*, Vol. 9(4), pp. 357–376 (2005).
77. **R.K. Mueller, D. Felix, J. Schreiber, A. Eschenmoser**, *HeIv Chim Acta,* Vol. 53(6), pp. 1479–1484 (1970).

78. **P.M. Lahti**, *Tetrahedron Lett.*, Vol. 24(23), pp. 2339–2342 (1983).
79. **Z.-S. Wu, W. Ren, L. Gao, B. Liu, C. Jiang and H.-M. Cheng**, *Carbon*, Vol. 47, pp. 493–499 (2009).
80. **G. Wang, J. Yang, J. Park, X. Gou, B. Wang, H. Liu, J. Yao**, *J. Phys. Chem. C*, Vol. 112, pp. 8192–8195 (2008).
81. **Z.-S. Wu, W. Ren, L. Gao, B. Liu, C. Jiang and H.-M. Cheng,** *Carbon*, Vol. 47, pp. 493–499 (2009).
82. **X. Fan, W. Peng, Y. Li, X. Li, S. Wang, G. Zhang, F. Zhang**, *Adv. Mater.*, Vol. 20, pp. 4490–4493 (2008).
83. **M.J. McAllister, J.-L. Li, D.H. Adamson, H.C. Schniepp, A.A. Abdala, J. Liu, M. Herrera-Alonso, D.L. Milius, R. Car, R.K. Prud'homme, I.A. Aksay**, Chem. *Mater.*, Vol. 19, pp. 4396-4404 (2007).
84. **H.C. Schniepp, J.-L. Li, M.J. McAllister, H. Sai, M. Herrera-Alonso, D.H. Adamson, R.K. Prud'homme, R. Car, D.A. Saville, I.A. Aksay**, *J. Phys. Chem. B*, Vol. 110, pp. 8535–8539 (2006).
85. **M. Zhou, Y. Wang, Y. Zhai, W. Ren, F. Wang, S. Dong**, *Chem.-Eur. J.*, Vol. 15, pp. 6116-6120 (2009).
86. **S.F. Spanò, G. Isgrò, P. Russo, M.E. Fragalà, G. Compagnini**, *Appl. Phys. A*, Vol. 117, pp. 19-23 (2014).
87. **J. Hecht,** *Optical Engineering*, Vol. 49(9), p. 091002-1 (2010).

88. **A. Einstein**, *Physika Zeitschrift.*, Vol. 18, pp. 121–128 (1917).
89. **R. Ladenburg**, *Z. Phys.*, Vol. 48, pp. 15–25 (1928).
90. **A.L. Schawlow, C.H. Townes**, *Physical Review*, Vol. 112, pp. 1940–1949 (1958).
91. **T.H. Maiman**, *Physical Review Letters.*, Vol. **4**, pp. 564–566 (1960).
92. **T. H. Maiman** , *Nature*, Vol. 187 , p. 493 (1960).
93. **H. Zeng, X.W. Du, S.C. Singh, S.A. Kulinich, S. Yang, J. He, W. Cai**, *Adv. Funct. Mater.*, Vol. 22, pp. 1333–1353 (2012).
94. **F. Breech, L. Cross**, *Applied Spectroscopy*, Vol. 16, p. 59 (1962).
95. **H.M. Smith, A.F. Turner**, *Applied Optics*, Vol. 4, pp. 147–148 (1965).
96. **G.W. Yang,** *Laser Ablation in Liquids*, Pan Stanford Publishing Pte. Ltd. (2012).
97. **K. Kempa, B. Kimball, J. Rybczynski, Z.P. Huang, P.F. Wu, D. Steeves, M. Sennett, M. Giersig, D.V. Rao, D.L. Carnahan, D.Z. Wang, J.Y. Lao, W.Z. Li, Z.F. Ren,** Nano Lett., Vol. 3, p. 13 (2003).
98. **X.F. Duan, C.M. Lieber,** Adv. Mater., Vol. 12, p. 12 (2000).
99. **H.G. Yang, H.C. Zeng**, *J. Phys. Chem. B*, Vol. 108, p. 3492 (2004).

100. **C.A. Mirkin, R.L. Letsinger, R.C. Mucic, J.J. Storhoff**, *Nature*, Vol. 382, p. 607 (1996).
101. **T. Tsuji, Y. Tsuboi, N. Kitamura, M. Tsuji**, *Appl. Surf. Sci.*, Vol. 229, p. 365 (2004).
102. **K. Sasaki, T. Nakano, W. Soliman, N. Takada**, *Appl. Phys. Express*, Vol. 2, p. 46501 (2009).
103. **F. Mafune, J.Y. Kohno, Y. Takeda, T. Kondow**, *J. Phys. Chem. B*, Vol. 31, p. 7577 (2002).
104. **F. Mafune, J.Y. Kohno, Y. Takeda, T. Kondow**, *J. Phys. Chem. B*, Vol. 107, p. 4218 (2003).
105. **Y. Takeuchi, T. Ida, K. Kimura**, *J. Phys. Chem. B*, Vol. 101, p. 1322 (1997).
106. **P.V. Kamat, M. Flumiani, G.V. Hartland**, *J. Phys. Chem. B*, Vol. 102, p. 3123 (1998).
107. **H. Fujiwara, S. Yanagida, P.V. Kamat**, *J. Phys. Chem. B*, Vol. 103, p. 2589 (1999).
108. **H. Muto, K. Miyajima, F. Mafune**, *J. Phys. Chem. C*, Vol. 112, p. 5810 (2008).
109. **J. Zhang, J. Worley, S. Denommee, C. Kingston, Z.J. Jakubek, Y. Deslandes, M. Post, B. Simard**, *J. Phys. Chem. B*, Vol. 107 , p. 6920 (2003).
110. **H. Hada, Y. Yonezawa, A. Yoshida, A. Kurakake**, *J. Phys. Chem.*, Vol. 80 , p. 2728 (1976).
111. **S. Eustis, H.Y. Hsu, M.A. El-Sayed**, *J. Phys. Chem. B*, Vol. 109, p. 4811 (2005).

112. **M. Sakamoto, M. Fujistuka, T. Majima**, *J. Photochem. Photobiol. C: Photochem. Rev.,* Vol. 10, p. 33 (2009).

113. **Y.H. Chen, C.S. Yeh**, *Chem. Commun.*, p. 371 (2001).

114. **G. Compagnini, E. Messina, O. Puglisi, V. Nicolosi**, *Applied Surface Science*, Vol. 254(4), pp. 1007-1011 (2007).

115. **C. Nethravathi, M. Rajamathi**, *Carbon*, Vol. 46, p. 1994 (2008).

116. **P. Russo**, PhD Thesis, pp. 65-99 (2014).

117. **H.O. Jeschke, M.E. Garcia, K.H. Bennemann**, *Phys. Rev. Lett.*, Vol. 87, pp. 15003-4 (2001).

118. **G. Compagnini, V. Mita, R.S. Cataliotti, L. D'Urso, O. Puglisi,** *Carbon*, Vol. 45, pp. 2456-2458 (2007).

119. **J. Zhou, C. Booker, R. Li, X. Zhou, T.K. Sham, X. Sun, Z. Ding**, J. Am. Chem. Soc., Vol. 129, pp.744-745 (2007).

120. **M. Feng, R. Sun, H. Zhan, Y. Chen**, Nanotechnol., Vol. 21, pp. 75601-7 (2010).

121. **M. Hiramatsu, H. Kondo, M. Hori**, *Nanotechnology and Nanomaterials » "New Progress on Graphene Research"*, Chapter 9, edited by Jian Ru Gong (2013).

122. **J. Zhou, C. Booker, R. Li, X. Zhou, T.K. Sham, X. Sun, Z. Ding.**, *J. Am. Chem. Soc.*, Vol. 129, pp. 744-745 (2007).

123. **J. Shang, L. Ma, J. Li, W. Ai, T. Yu, G.G. Gurzadyan**, *Scientific Reports*, Vol. 2, p. 792 (2012).

124. **F. Tuinstra, J.L. Koenig,** J. Chem. Phys., Vol. 53, p.1126 (1970).

125. **H. Wilhelm, M. Lelaurain, E. McRae, B. Humbert**, *J. Appl. Phys.*, Vol. 84, p. 6552 (1998).

126. **C.-T. Chien, S.-S. Li, W.-J. Lai, Y.-C. Yeh, H.-A. Chen, I.-S. Chen, L.-C. Chen, K.-H. Chen, T. Nemoto, S. Isoda, M. Chen, T. Fujita, G. Eda, H. Yamaguchi, M. Chhowalla, C.-W. Chen**, *Angew. Chem. Int. Ed.*, Vol. 51, p. 6662 (2012).

127. **K.P. Loh, Q. Bao, G. Eda, M. Chhowalla**, *Nat. Chem.*, Vol. 2, p. 1015 (2010).

128. **H. Bässler, M. Gailberger, R. F. Mahrt, J. M. Oberski, G.Weiser**, *Synth. Met.*, Vol. 49, p. 341 (1992).

129. **J. Tauc**, *Materials Research Bulletin*, Vol. 3, pp. 37–46 (1968).

130. **R.L.D. Whitby, A. Korobeinyk, V.M. Gunko, R. Busquets, A.B. Cundy, K. La´szlo´, J. Skubiszewska-Zie¸ba, R. Leboda, E. Tombacz, I.Y.**

Toth, K. Kovacs, S.V. Mikhalovsky, *Chem. Commun.*, Vol. 47, p. 9645 (2011).

131. **B. Konkena, S. Vasudevan**, *J. Phys. Chem. Lett.*, Vol. 3, p. 867 (2012).
132. **H.M. Kim, J.K. Lee, H.S. Lee**, *Thin Solid Films*, Vol. 519, pp. 7766–7771 (2011).
133. **I.H. Tseng, Y.F. Liao, J.C. Chiang, M.H. Tsai**, *Materials Chemistry and Physics*, Vol. 136, pp. 247-253 (2012).
134. **H.M. Kim, H.S. Lee,** *Carbon Lett.***,** Vol. 15 (1), pp. 50-56 (2014).
135. **H. Kim, Y. Miura, C.W. Macosko**, *Chem. Mater.*, Vol. 22, p. 3441 (2010).
136. **O.C. Compton, S. Kim, C. Pierre, J.M. Torkelson, S.T. Nguyen**, *Adv. Mater.*, Vol. 22, p.4759 (2010).
137. **J.S. Bunch, S.S. Verbridge, J.S. Alden, A.M. van der Zande, J.M. Parpia, H.G. Craighead, P.L. McEuen**, *Nano Lett.,* Vol. 8, p. 2458 (2008).
138. **J.-H. Yeun, G.-S. Bang, B.J. Park, S.K. Ham, J.-H. Chang**, *J. Appl. Polym. Sci.*, Vol. 101, p. 591 (2006).
139. **N.K. Lape, E.E. Nuxoll, E.L. Cussler**, *Journal of Membrane Science*, Vol. 236, pp. 29–37 (2004).

140. **E.L. Cussler, S.E. Hughes, W.J. Ward III, R. Aris**, *J. Membr. Sci.*, Vol. 38, p. 161 (1988).

141. **J.R. Welty, C.E. Wicks, R.E. Wilson**, *Fundamentals of Momentum, Heat, and Mass Transfer*, 3rd Ed. John Wiley & Sons, New York (1983).

142. **A. Polyakova, E.V. Stepanov, D. Sekelik, D.A. Schiraldi, A. Hiltner, E. Baer**, *J. Polym. Sci. B*, Vol. 39, p. 1911 (2001).

143. **R.R. Nair, H.A. Wu, P.N. Jayaram, I.V. Grigorieva, A.K. Geim**, *Science*, Vol. 335, p. 442 (2012).

144. **W. Hu, C. Peng, W. Luo, M. Lv, X. Li, D. Li, Q. Huang, C. Fan,** *ACS Nano*, Vol. 4(7), pp. 4317-4323 (2010).

145. **T.-F. Yeh, J. Cihlar, C.-Y- Chang, C. Chang and H. Teng**, *Mater. Today*, Vol, 16, pp. 78-84 (2013).

146. **S. Liu, T. H. Zeng, M. Hofmann, E. Burcombe, J. Wei, R. Jiang, J. Kong, Y. Chen**, *ACS Nano*, Vol. 5, p. 6971 (2011).

147. **R. Matthews**, *J. Chem. Soc.*, Vol. 1, p. 457 (1984).

148. **K. Okamoto, Y. Yamamoto, H. Tanaka, M. Tanaka, A. Itaya**, *Chem. Soc. Jpn*, Vol. 58, p. 2015 (1985).

149. **L. Westwood**, *Carbon*, Vol. 49, pp. 741-772 (2011).

150. **R.I. Bickley, T. Gonzalezcarreno, J.S. Lees, L. Palmisano, R.J.D. Tilley**, *J. Solid State Chem.*, Vol. 92, pp. 178–190 (1991).

151. **R. Leary, A. Westwood**, *Carbon*, Vol. 49, pp. 741-772 (2011).

152. **T.F. Yeh, J. Cihlàr, C.Y. Chang, C. Cheng, H. Teng**, *Materials Today*, Vol. 16(3), pp. 78-84 (2013).

153. **H. Zhang, et al**., *ACS Nano*, Vol. 4, p. 380 (2010).

154. **Y. Kim, et al**., *Small*, Vol. 8, p. 1038 (2012).

155. **J.S. Lee, et al.**, *Adv. Mater.*, Vol. 24, p. 1084 (2012).

156. **X.Y. Zhang, et al.**, *J. Mater. Chem.*, Vol. 20, p. 2801 (2010).

157. **X. Zhang, et al.**, *Int. J. Hydrogen Energy*, Vol. 37, p. 811 (2012).

158. **F. Zou, et al.**, *Scripta Mater.*, Vol. 64, p. 621 (2011).

159. **W. Wang, P. Serp, P. Kalck, J.L. Faria**, *J Mol Catal A: Chem*, Vol. 235(1–2), pp. 194–199 (2005).

160. **K. Woan, G. Pyrgiotakis, W. Sigmund**, *Adv. Mater.*, Vol. 21(21), pp. 2233–9 (2009).

161. **G. Pyrgiotakis, S.H. Lee, W.M. Sigmund**, Advanced Photocatalysis with anatase nano-coated multi-walled carbon nanotubes. In: Presented at MRS spring meeting. San Francisco, USA: *Materials Research Society*; p. 83–88 (2005).

List of works

Publications

S.F. Spanò, G. Isgrò, M.E. Fragalà, P. Russo, G. Compagnini, "Tunable properties of Graphene Oxide reduced by laser irradiation", *Appl. Phys. A*, Vol. 117, Issue 1, pp. 19-23 (2014).

Orals

- **P. Russo, S. F. Spanò, A. Hu, G. Compagnini,** "Laser Treated Graphene Oxide for Dye Removal" (Co-author). Presented at the conference: "ANGEL 2014" (*Advanced Nanoparticle Generation and Excitation by Laser in Liquids*) in Matsuyama (Japan).
- **M. G. Sinatra, S. F. Spanò, P. Russo, G. Compagnini**, "Spectroscopic characterization of ultrafine TiO_2 NPs produced via laser ablation of titanium in water" (Co-author). Presented at the conference: "GISR 2014" (*III Italian Meeting on Raman Spectroscopy and Non-Linear Optical Effects*) in Parma (Italy).
- **M. A. Buccheri, S. Scalese, S.F. Spanò, D. D'Angelo, G. Compagnini, G. Rappazzo and V. Privitera**,

"Antimicrobial properties of graphene oxide/TiO2hybrid composites". Presented at the conference: "IEEE-NMDC 2014" (*IEEE Nanotechnology Materials and Devices Conference*) in Aci Castello (Italy).

Posters

- **S. F. Spanò, G. Isgrò, M.E. Fragalà, P. Russo, G. Compagnini**, "Tunable photoluminescence of Graphene Oxide reduced by laser irradiation". Presented at the conference: "COLA 2013" (*12th Conference on Laser Ablation*) in Ischia (Italy).
- **G. Isgrò, S.F. Spanò, L. D'Urso, G. Compagnini, E. Fazio, F. Neri**, "Optical imiting effect in laser irradiated graphene oxide nanomaterials". Presented at the conference: "E-MRS 2014 Spring Meeting" (*European Materials Research Society*) in Lille (France).
- **P. Russo, S.F. Spanò, A. Hu, G. Compagnini,** "Nanosecond and femtosecond laser irradiation for graphene related nanomaterials production". Presented at the conference: "E-MRS 2014 Spring Meeting" (*European Materials Research Society*) in Lille (France).

Acknowledgements

I would like to thank my research supervisor, Professor Giuseppe Compagnini, for his guidance.
I would like also to express my sincere gratitude to my other research supervisor Dr. Silvia Scalese and Dr. Daniele D'Angelo, at CNR-IMM of Catania, for their support and advice.
I would like to offer my thanks to Dr. Maria Antonietta Buccheri at the Biological Sciences Departments for the biological experiments and measurements, and to Dr. Corrado Bongiorno at CNR-IMM of Catania for TEM images.
Moreover, I would like also to thank Dr. Riccardo De Bastiani for electric measurements, but also for his help for providing me comments and suggestions.
I want to show my gratitude to my LabFSN Research Group for the support and great friendship.
My warmest thanks go to my parents, family and friends, and to Roberto for their endless love, support and encouragement!
Thanks a lot!